Plasma Physics Reports, Vol. 28, No. 9, 2002, p. 711. Translated from Fizika Plazmy, Vol. 28, No. 9, 2002, p. 771.
Original Russian Text Copyright © 2002 by the Editorial Board.

In Memory of Dmitriĭ Aleksandrovich Panov

The papers published in this issue under the rubrics "Magnetic Confinement Systems" and "Tokamaks" are devoted to the memory of Dmitriĭ Aleksandrovich Panov, suddenly deceased November 4, 2001.

D.A. Panov, colleague and successor of I.N. Golovin, was one of the leaders of mirror-based magnetic plasma confinement research. However, the importance of his scientific activity goes far beyond the scope of this field. The achievements of the laboratory headed by Panov over many years at the Kurchatov Institute had a marked influence on the development of controlled fusion research as a whole. Being a bright, extraordinary person, he manifested himself in full measure as a talented scientist and experienced leader.

Among the achievements of Panov in the field of fusion research, one can note successful experiments on the feedback suppression of the flute and ion cyclotron plasma instabilities. He initiated the implementation of superconducting magnetic coils in fusion devices. In 1971, the first confinement system with superconducting windings (Ogra-III) was created under his leadership.

Being a heaven-born experimentalist, Panov also made a substantial contribution to the theory of magnetic confinement systems. In the beginning of the 1980s, he put forward the principle of "orthogonality" of the magnetic field geometry (the perpendicularity of the magnetic field lines to the contours of the absolute value of the magnetic field strength) to eliminate neoclassical transport. This idea was then developed in the modern theory of optimization of three-dimensional magnetic configurations with the purpose of improving plasma confinement.

Everyone who was lucky enough to work and communicate with D.A. Panov appreciates his high professionalism, good will, kindness, skill to listen, and reliability.

The Editorial Board is grateful to the authors who have responded to the proposal to present papers for this issue.

1063-780X/02/2809-0711$22.00 © 2002 MAIK "Nauka/Interperiodica"

Plasma Physics Reports, Vol. 28, No. 9, 2002, pp. 712–720. From Fizika Plazmy, Vol. 28, No. 9, 2002, pp. 772–782.
Original English Text Copyright © 2002 by Post.

MAGNETIC CONFINEMENT SYSTEMS

The Kinetic Stabilizer: Issues and Opportunities[1]

R. F. Post

Lawrence Livermore National Laboratory, Livermore, CA 94551, USA

Received January 24, 2002

Abstract—Five decades of fusion research have resulted in a solid base of understanding of the physics of plasma confinement by magnetic fields, including documentation of the role of the topology of the magnetic fields, i.e., "open" or "closed" field lines, in determining the confinement. Without known exception, closed systems, such as tokamaks, stellarators, or reversed-field pinches, have confinement times that are dominated by turbulence. As a result, to produce net fusion power, closed systems must be so large in size as to raise questions as to their practicality. By contrast, there are examples of open (mirror-based) systems where turbulence, if present at all, was at such low levels as to have a negligible influence on the confinement. Specifically, members of a subset of open systems, those with axisymmetric fields, have demonstrated cross-field transport rates that agree with classical predictions, opening up the possibility of fusion power systems that would be much smaller than their closed-field counterparts. Standing in the way of implementing axisymmetric mirror-based fusion systems is the MHD-unstable nature of their equilibria. The kinetic stabilizer represents a proposed way to overcome this difficulty, one based on theory that has been confirmed in the gas dynamic trap (GDT) axisymmetric mirror experiment in Novosibirsk, Russia. MHD-stabilization in the GDT arises from the presence of a sufficient density of effluent plasma on the outwardly expanding field lines outside the mirrors. However, in those mirror-based fusion systems, such as tandem-mirrors, that would operate at lower plasma collisionalities than the GDT, the effluent plasma density would be too low for this stabilization method to be effective. The kinetic stabilizer overcomes this difficulty by using ion beams injected from ion sources located far out on the expanding field lines beyond the outer mirror. These ion beams, aimed at small angles to the field lines, are compressed, stagnated, and reflected by the inwardly converging field, forming a localized plasma that accomplishes the stabilization. In previous papers, theory was developed and examples were given of mirror and tandem-mirror systems using kinetic stabilizers to achieve fusion-relevant plasma regimes. In this paper, some of the special issues that must be faced in pursuing the kinetic-stabilizer approach to fusion power will be discussed, together with some perceived opportunities for optimizing such systems. *© 2002 MAIK "Nauka/Interperiodica".*

1. INTRODUCTION

The magnetic-mirror approach to fusion has had a long history of development, being one of the first suggested means for solving the confinement problem of magnetic fusion. Dr. Dmitriĭ Panov, in whose honor this paper is being written, had a long and distinguished career in the experimental investigation of mirror-based fusion systems. This paper is concerned with a possible solution to a problem, the MHD instability of axisymmetric mirror systems, a problem that Dr. Panov also particularly addressed in his studies.

The 50-year history of research into the confinement of plasma in magnetic fields should have taught us one clear lesson. The lesson is that there is a fundamental difference in the character of plasma confinement between that in so-called "closed" systems, such as the tokamak, the stellarator, or the reversed-field pinch, and "open" systems, such as those based on the use of the magnetic mirror principle to provide axial confinement. Closed systems, with no known exceptions, show confinement that is dominated by turbulence-related processes, rather than by "classical," i.e., collision-related, processes. As a result, to achieve confinement adequate for fusion power purposes in, for example, the tokamak requires that it be scaled up in size and power level to the point that its ultimate practicality as an economically viable source of fusion power is open to question. By contrast, from earliest days, there have been examples of open systems where turbulence, if present at all, is at such a low level that only collision-related processes play a significant role in determining the confinement. Furthermore, within the class of mirror-based systems, those with axisymmetric magnetic fields (i.e., solenoidal fields produced by coaxial circular coils), have most clearly attained cross-field transport rates approaching the classical, "Spitzer" [1] rate predicted for such fields. Given this circumstance, in a search for simpler and smaller fusion power systems than those based on closed-field topology, axisymmetric mirror-based systems appear to offer much promise.

Standing in the way of implementing new forms of axisymmetric mirror-based fusion power systems is the long-understood tendency of such systems toward MHD instabilities of the "interchange" variety [2], a type of instability that leads to a coherent drift of the confined plasma column across the confining field. This

[1] This article was submitted by the authors in English.

type of transport of the plasma column across its confining field is to be contrasted with the enhanced-diffusion type of transport associated with the turbulent processes encountered in closed systems. As experiment has shown (for example, in the axisymmetric-field gas dynamic trap (GDT) at the Budker Institute in Novosibirsk [3]) when the MHD interchange instability is suppressed, the rate of transport of the plasma across the magnetic field can approach the slow diffusion rates expected from interparticle collisions, namely the Spitzer-predicted rate. The GDT experiment [3] and theory that preceded it [4] represent, in fact, the starting points for the kinetic stabilizer (KS) concept [5, 6], selected aspects of which will be discussed in this paper.

The stabilization method employed in the GDT is based on the following plasma physics considerations, reviewed briefly here.

In an axisymmetric mirror cell for which the ratio of the mean ion orbit radius to the radius of the plasma, r_i/a, is greater than the ratio of the plasma radius to the cell length, so-called "finite-orbit" effects [7] stabilize all but the lowest order MHD interchange mode. This $m = 1$ mode corresponds to a simple sideways drift of the plasma column as a whole.

For the $m = 1$ mode, as with all interchange modes, the source of free energy is the energy of expansion of the plasma that arises from the circumstance that, in an axially symmetric mirror cell, the volume of a given tube of flux increases if that tube is transported in the radial direction. The geometric origin of this effect lies in the competition between the regions of positive and negative field-line curvature that characterize the magnetic field between the mirrors. As shown by the theory [2], the region of negative field-line curvature (outwardly decreasing field strength) midway between the mirrors always wins (if only slightly) over the regions of positive curvature (outwardly increasing field strength) located near the mirrors.

To better define the plasma physics issues associated with the stabilization method employed in the GDT (and the one that is to be employed in the KS), it is helpful to consider the interchange instability from the standpoint of plasma currents and particle drifts. Looked at from that aspect, the interchange instability arises from the fact that, in regions of negative field-line curvature, the particle currents associated with the oppositely directed azimuthal drifts of the ions and electrons, if not canceled by current flow along the field lines from other regions of the plasma, would result in an azimuthally directed electric field in that region. In that azimuthal electric field, the ions and electrons would together perform an outwardly directed $\mathbf{E} \times \mathbf{B}$ motion. Stabilization occurs when three conditions are satisfied. The first condition is that there should exist a region (or regions) of positive field-line curvature down the field lines from the region of negative field-line curvature. The second condition is that these regions should be extensive enough so that the accumulative effect of the electron and ion drifts in them produces canceling currents that are sufficient to overcome the destabilizing charge separation that arises in the regions of negative field line curvature. The third, equally important, condition that must be satisfied is that there should exist a sufficient plasma density on the field lines between the regions of negative and positive curvature to allow the uninhibited flow of the neutralizing currents that suppress the instability.

Returning now to the situation in the GDT, since the field-line curvature of the field lines emerging outside each mirror is strongly positive, it follows that, if a sufficient amount of plasma were to be present outside the mirrors and if this plasma can electrically "communicate" adequately with the interior plasma, it can stabilize the interior, contained, plasma. As the theory shows [4], the plasma in the expander can be orders of magnitude lower in density and pressure and still be sufficiently dense to stabilize the interior plasma.

In the GDT, which operates in a dense and highly collisional plasma region where the mean-free-path for ion–ion collisions is shorter than the length of the plasma, the effluent plasma leaking through the mirrors, even though much lower in density than the interior, confined, plasma, is still sufficiently dense to satisfy the three conditions stated above. As a result, it MHD-stabilizes the confined plasma at a remarkably high plasma beta value of 30%. However, if we consider the situation that would be encountered in a conventional tandem-mirror fusion system, a different picture is obtained. Such systems would operate at plasma temperatures and densities where the mean-free-path for ion–ion collisions is long compared to the length of the plasma. In such a case, the effluent plasma density would be too low to stabilize the interior plasma and other means must be sought. The long-standing conventional approach to solving the MHD stability problem has been to abandon axisymmetry and to employ multipole magnetic-well fields, involving "baseball" or "yin-yang" [8] coils in the mirror cells, following the lead of the classic mirror experiment performed by Ioffe [9] in the 1960s.

Though highly effective in stabilizing MHD modes, the use of nonaxisymmetric fields not only introduces transport-producing "bounce-resonant" particle drifts [10], but also increases the complexity of the magnetic field coils of a tandem-mirror system. A consequence of this field-coil complexity is that it severely constrains the field strengths that can be attained in the mirrors and it inhibits the ability of the designer to reduce the volume of the plasma in the plug mirror cells in order to minimize the power required to maintain the plugging plasmas contained in these cells.

Table 1. Fusion Parameters of Example 1

Central cell magnetic field	0.5 T
Mirror ratio of central cell	2.0
Fusion plasma ion density (50–50 DT)	6.2×10^{20} m^{-3}
Ion and electron temperature of central-cell plasma	15 keV
Beta value of central-cell plasma	0.3
Length of fusion plasma	25.0 m
Diameter of fusion plasma	0.15 m

2. THE KINETIC STABILIZER CONCEPT

The KS concept as applied to axisymmetric mirror-based systems has been described in previous papers [5, 6]. Its starting point was an earlier concept, the "kinetic tandem" [11]. The idea is to create *in situ* a localized plasma on the expanding field lines lying outside the outermost mirror of an axisymmetric tandem-mirror system. This localized plasma is to be created by the "kinetic" technique of launching directed ion beams from ion sources lying still farther out on the expanding field lines. These ions, aimed at small angles to the local direction of the field lines, would be compressed, stagnated, and reflected at a predetermined position on the converging field lines, chosen so as to optimize the stabilizing effect of the beam-produced plasma. What was shown in the previous papers is that, when optimally produced, the density of this stabilizer plasma could be many orders of magnitude lower than that of the plug plasma in a tandem-mirror system and still be effective in MHD-stabilizing that plasma (provided that the three conditions stated above are all satisfied).

The field-line-curvature-related condition that must be satisfied by the KS plasma can be seen from an examination of the MHD stabilization criterion for an axisymmetric mirror system [4], stated in integral form in the expression

$$I_s = \int_{-L}^{L} a^3 \frac{d^2 a}{dz^2} [p_\perp + p_\parallel] dz > 0. \quad (1)$$

In this expression, the radius of the plasma is represented by the term a. The integral is to be carried out over the length of the plasma between the ends of the system, located at $-L$ and $+L$, respectively. The term in the brackets represents the total kinetic pressure of the plasma (a function of position). This pressure term is then multiplied by the plasma radius cubed and the second derivative of the plasma radius (the curvature term) and then integrated over the length of the system to determine the sign of I_s.

As can be seen from Eq. (1), regions of the plasma at large radius and where the field-line curvature is strongly positive will make the largest positive (stabilizing) contributions to the integral. The KS takes advantage of this scaling by creating its kinetically produced plasma at an optimally located position on the expanding field lines (the "expander") outside the mirrors. To achieve this optimization, the flux surfaces in the expander region can be tailored in specified ways (to be illustrated in a later section).

In order to study the KS in a quantitative manner, computer codes were written that perform the following functions:

(i) Generation of the flux surfaces for mirror cells and for the expander.

(ii) Calculation of the magnetic compression and localization of ion beams injected into the expander field, with angular distributions that simulate those from actual ion sources.

(iii) Evaluation of instability integral (1), both for mirror-contained plasmas and for the beam-produced stabilizer plasma.

In the next section, we will present an example (from a previous paper [5]) that illustrates the use of these codes, a route to a discussion of some new results.

3. AN EXAMPLE: STABILIZATION OF A SINGLE MIRROR CELL

As an example of a fusion-relevant system, for example, one that could be used to produce a high flux of 14 MeV D–T neutrons for material testing purposes, we consider a simple mirror cell with the following parameters (Table 1).

The first step in the code calculations was to evaluate the MHD stability integral, Eq. (1), for the mirror cell, assuming unity pressure in the cell (dropping to zero near the mirrors). The flux function that was assumed for this calculation is one that has been employed previously to model the fields in mirror cells [12]. It is of analytic form, involving trigonometric functions and Bessel functions of imaginary argument, representing the field lines in the vicinity of the end mirrors. This flux function matches smoothly onto a cylindrical flux tube (zero second derivative) in the central region of the mirror cell. The shape of the flux surfaces near the mirrors is shown in Fig. 1. In a later section, we will discuss more advantageous shapes for the flux surfaces, ones that can be employed to diminish the negative contributions to the instability integral from the regions of negative field-line curvature.

When evaluated between the midplane and the end of the mirror cell, the value of the integral, I_s, of Eq. (1) associated with the flux surface of Fig. 1 is -1.7×10^{-6}.

The next task of the code is to calculate the shape of the flux surface in the expander region. For this example, the expander flux surface was generated by a paraxial representation derived from a magnetic field, B_z, on the axis, the intensity of which was assumed to decrease in a Gaussian manner with distance from the mirror. This flux surface contour, as generated by the code, is shown in Fig. 2. As with the mirror cell flux

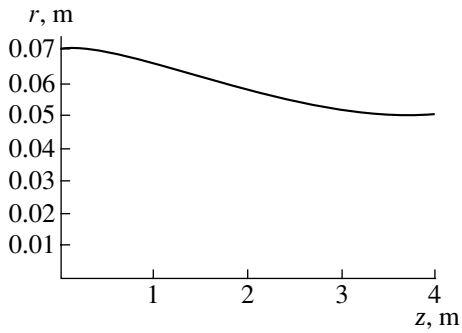

Fig. 1. Shape of a Bessel-function-type flux surface in a mirror cell used to calculate the stability integral.

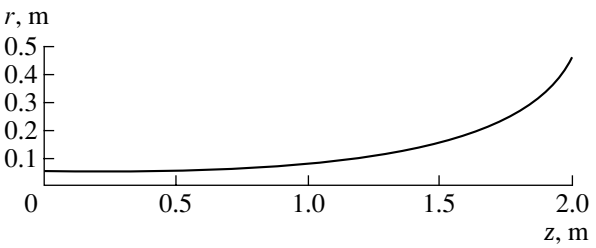

Fig. 2. Expander flux surface for a Gaussian variation of the field on the axis.

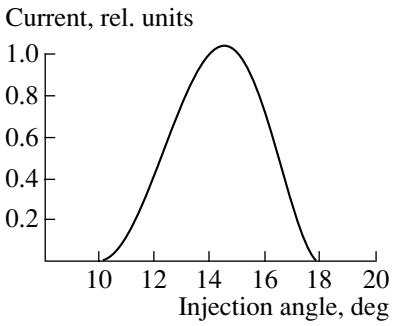

Fig. 3. Source angular distribution used in the example.

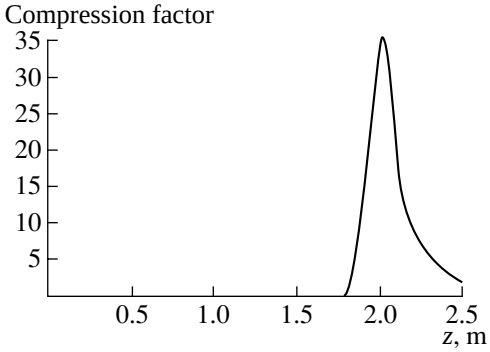

Fig. 4. Spatial location and density compression factor of KS plasma.

surface, we will later consider more advantageous ways to configure the expander flux surface.

The next task of the code is to calculate the value of the instability integral for a plasma that is assumed to be located favorably on the expander flux surface. The result found for a unit pressure KS plasma located between 1.9 and 2.1 m from the mirror was the value $I_s = +0.39$. Comparing this value to that found for the central cell, we find that the ratio between the two values is 4.5×10^{-6}. It follows that the pressure of the KS plasma can be more than five orders of magnitude smaller than that of the central plasma and still stabilize it against the MHD interchange instability, provided the "communication" requirement between the central plasma and the KS plasma, mentioned earlier, is also met.

To complete the analysis, the final task of the code was to calculate the location and pressure of a plasma generated by the compression, stagnation, and reflection of ions emerging from ion sources located farther out on the expander field lines. For this calculation, an analytical form was assumed for the angular distribution emitted by the ion sources, approximating ones characteristic of typical ion sources. By varying the width and mean angle of injection of these ions, a set of parameters could be determined that optimized the stabilization, i.e., which minimized the current and/or power requirements of the ion sources. Figure 3 shows the form of the angular distribution that was used to represent the ion sources.

Given the source angular distribution (which can be varied in width and mean angle of injection relative to the field lines) and the location of the sources (at 2.5-m distance from the mirrors), the code next used this distribution to calculate the location, the compressed particle density (relative to the density at the sources), and the spatial distribution of the KS plasma. This plasma was then used as input to another code, one that calculates the value of stability integral (1). Figure 4 shows the relative ion density, the location, and the spatial extent of the KS plasma. Note the density compression (in this case, by a factor of 35) caused by the convergence and stagnation of the injected ions.

When the density compression and the location in the expander of the KS plasma was used as input to the code for calculating the stability integral, a value of this integral of 11.6 was found. Therefore, the ratio of that determined for the central cell (1.7×10^{-6}) to this value is equal to 1.5×10^{-7}. We see therefore that the kinetic pressure of the injected KS ions, as averaged over the surface on which the ion sources are located, can be almost seven orders of magnitude smaller than the peak kinetic pressure in the central cell and still stabilize it against the MHD interchange mode, given a sufficient level of "communication" between the KS plasma an the plasma in the central cell.

Table 2

Mean diameter of KS stabilizer plasma	1.0 m
Area of KS ion sourse region	4.0 m^2
Energy of KS ions (Cs^+)	1.0 keV
KS ion-beam power (two ends)	200 kW
D–T fusion power released	45 MW

Table 3. Fusion Parameters of MINIMARS

Fusion Power	1200 MW
Electrical power output	600 MW
Neutron wall loading	2.7 MW/m^2
Central-cell magnetic field	3.0 T
Choke coil field	26.0 T
Length of central cell	95.0 m
Plasma radius	0.42 m
Ion temperature	30 keV
Plasma beta	0.6
Mirror ratio of central cell (beta-enhanced)	13.7

At the axial position of the sources, the magnetic field has dropped to about 0.02 T and the flux tube has expanded to a cross-sectional area of about 4 m^2. This area, taken together with an assumption about the energy and the type of ion emitted by the KS ion sources, will now permit us to estimate the beam power required to stabilize the plasma and then to compare this power to the fusion power released. The ions chosen for the KS ion sources were 1-keV Cs^+ ions (easy to generate and more effective because their low energy and large mass reduces the beam power requirements). Table 2 summarizes these parameters and gives the results for the required KS beam power and the calculated fusion power output from the central cell, using the parameters of Table 1 as input.

As can be seen, the fusion power released is much larger than the KS plasma beam power required to stabilize the plasma in the mirror cell. However, this example is not presented as a viable fusion power system, since no provision has been made for reducing the mirror end losses. Rather, the promise of the KS stabilizer comes from its application to tandem mirror systems. In the next sections, we will discuss this application and some of the special issues and opportunities that present themselves.

4. THE KINETIC STABILIZER TANDEM MIRROR: SPECIAL ISSUES

Of special interest for fusion purposes is the application of the KS concept to tandem-mirror fusion systems. This application has been discussed in a preliminary way in a previous paper [6]. In that paper, it was shown that the use of axisymmetric confining fields should permit the design of practical tandem mirror fusion power plants based on the original TM concept of Dimov, Fowler, and Logan, i.e., tandem mirror systems that would generate the required plugging potentials by the straightforward means of increasing the plasma density in the plugging cells by an order of magnitude relative to the central cell, while at the same time being able to operate with high central-cell mirror ratios. When one is employing only circular coils to produce the confining fields, not only is it possible to increase the fields in the plugging cells far above that possible with yin-yang or baseball coils, but at the same time the plasma volume in these cells can be made much smaller than would be possible with the nonaxisymmetric fields. Higher mirror ratios, higher end-cell fields, and small plugging plasma volumes translate to a major simplification (e.g., "thermal barriers" would not be required) and improvement in performance and should therefore result in major economic advantages.

To briefly summarize the results of the previous TM calculations, they addressed a "redesign" of an earlier-studied TM system, called "MINIMARS." [13]. In the calculations, the same fusion power parameters were retained as those of the earlier study, but the end plugging region (which had used multipole fields and thermal barriers) was replaced by small-volume axisymmetric mirror cells. What was calculated was the estimated power required to maintain the plugs at a high plasma density and the estimated KS beam power that would be required to stabilize the plug cells. What was found was that the end cells make the largest negative contribution to the stability integral. It follows that, if these are well stabilized, it will assure that the central-cell plasma will also be stable (assuming that the "communication" between the various plasmas is adequately robust). Note in this connection that the elimination of thermal barriers will improve the communication between the central-cell plasma and the end-cells, thereby reducing some of the concerns that arise when thermal barriers are employed. Table 3 summarizes the fusion parameters of MINIMARS that were assumed in the KS example [6].

In order to calculate the power required by the end cells, i.e., the sum of the beam power required to maintain the plugging plasmas plus that required to power the KSs, compromises between competing requirements had to be made. While the power required to maintain the plug plasmas is reduced if their length is made shorter (smaller volume of plasma), the negative contribution to the stability integral increases as the length is shortened. Also, the use of higher ion energies in the plugs reduces their mirror losses, but increases the pressure that must be stabilized by the KS. In the compromises made, 100 keV deuterons were chosen for the plug ions and the cell length was set at 3.0 m. With these parameters, the plug beam power and the KS beam power were approximately equal, being

8.2 MW for the former (each end) and 5.0 MW for the latter. The total power required to maintain and stabilize the plug cells was still small compared to the 600 MW fusion power output, the Q value of which was thus primarily determined by the confinement $n\tau$ value of the central cell.

One important change that was made in the updated MINIMARS example as compared to the previous study was an optimization of the expander. This optimization was accomplished in the following way: Consider a case in which, in the expander, the flux surface emerging from the mirror resembles a stylized trumpet horn. That is, it is of conical shape (zero second derivative), changing farther out to a sharply outwardly curving flux surface that shortly changes again to a conical surface for further expansion until the location of the ion sources is reached. The shape of the flux surfaces in such an expander is shown in Fig. 5.

With this shape of expander, the ion sources are to be aimed to converge at the high-curvature region between the two conical surfaces. In this way, their stabilizing effect can be optimized. Further optimization (to be discussed in a later section) arises from moving the location of high positive curvature in or out in the axial direction. Moving the location inward, although it reduces the radius-cubed term in the stability integral, is compensated for by greater magnetic compression of the beams and by an increase in the second-derivative term in the integral, with possible ancillary advantages having to do with "communication" and other issues.

5. TANDEM-MIRROR PLUG CELLS: ISSUES AND OPTIMIZATION

With the previous discussions as background, we will now address some new issues and some further avenues for optimization of tandem-mirror systems employing KSs.

Since the plug cells represent the largest negative contribution to the stability integral and thus require the lion's share of the KS beam power, it is worthwhile to examine ways to reduce the magnitude of this negative contribution, to be accomplished through shaping the flux surfaces in the plug cells. At the same time this type of optimization is going on, one must keep one's eye on a particular long-standing issue associated with mirror confinement, namely the Alfvén ion cyclotron (AIC) instability. This instability is driven by the inherent anisotropy of the mirror-confined plug ions. While "warm-plasma" stabilization, normally present in a tandem-mirror system without thermal barriers, is effective on other loss-cone-type instabilities, it is necessary to use special means to avoid the AIC mode. The technique that was developed to suppress this mode is that of "sloshing ions." That is, ions are injected into the mirror cell at an intermediate angle (relative to the field lines) so that they reduce the anisotropy of the trapped plasma. The ability to use sloshing ions to suppress the AIC has been predicted theoretically [14] and demonstrated in tandem-mirror experiments such as TMX-U [15] and Gamma 10 [16]. The fact that the presence of a sloshing-ion population does not have a deleterious effect on the confinement of an otherwise isotropic plasma has also been demonstrated in the GDT [3].

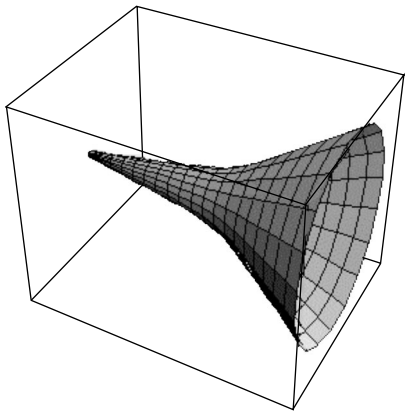

Fig. 5. Schematic representation of the flux surface in an optimized expander.

In the search for an improved flux surface configuration for the plug cells, it was found possible to achieve two objectives at once. The field configuration was calculated from a paraxial expansion (to fifth order in the plasma radius) of the field on the axis arising from the superposition of currents in circular loop coils. The field was shaped in such a way that the presence of the sloshing-ion population reduces the negative contribution of the plug cell to the stability integral. This long-understood concept takes advantage of the fact that, if the sloshing ions are preferentially reflected in regions of the field with positive field-line curvature, the negative contribution of the plasma to the instability integral will be reduced. The presence of collisional randomization in steady-state will prevent the achievement of complete stabilization, but that is not required if the system is to employ KSs. However, these stabilizers would now require much less beam power than if the sloshing ions were not present.

To perform the needed evaluations, the stability code was adapted to calculate flux surfaces generated by coaxial, coplanar, circular-hoop coils, the currents in which increase linearly (from a base value) in moving toward the mirrors, starting from the midplane between the mirrors. As was shown in an early report [17], this type of coil assembly produces a mirror-cell field the flux surfaces of which are everywhere convex (have positive curvature) with respect to the axis, except for a short region whose length is on the order of the coil radius. Figure 6 shows an example of such a flux-surface contour, as generated by the code.

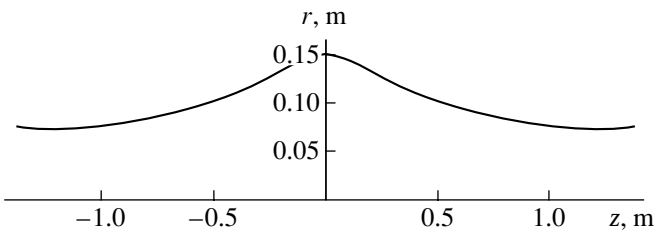

Fig. 6. Flux surface contour associated with an assembly of circular current loops (radius 0.25 m) the currents in which increase linearly (from a base value) with distance from the midplane (note the change of scale between the r and z axes).

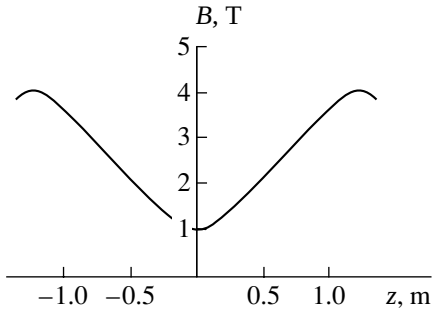

Fig. 7. Variation (with distance from the midplane) of the magnetic field strength on the axis of the coil system producing the flux surface shown in Fig. 6.

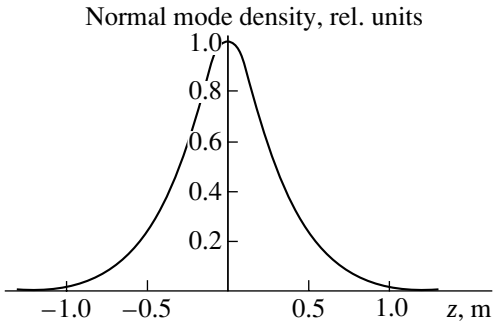

Fig. 8. Normal-mode density distribution for a Bessel-function mirror cell.

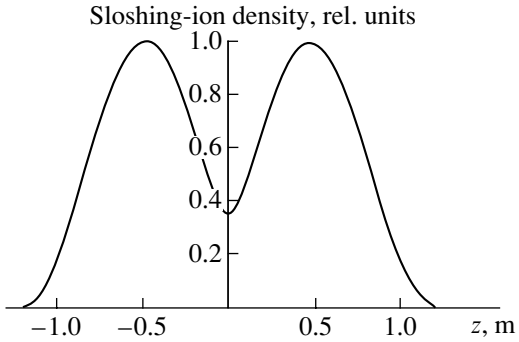

Fig. 9. Sloshing-ion axial density distribution.

The strength of the magnetic field on the axis of the coil system is shown in Fig. 7. Note that the mirror ratio is 4 : 1 for this choice of values.

The shape of the flux surface shown in Fig. 6 can be seen to be such that it is well-suited for the containment of a sloshing-ion type of distribution in that the sloshing ions will be preferentially reflected in regions of positive field-line curvature. On the other hand, this flux surface would not be expected to be advantageous for the centrally peaked "normal-mode" distributions that would be characteristic of mirror-confined plasmas under usual circumstances.

To illustrate the gain (reductions in the negative contribution to the stability integral) that could be expected by employing sloshing-ion distributions in mirror cells with flux surfaces of the type shown in Fig. 6, comparison calculations of the stability integral were made. First, a normal-mode distribution was used together with a Bessel-function type of flux surface (an example of which is shown in Fig. 1). The cell length was 2.5 m, the mirror ratio was 4 : 1, and the radius of the flux surface at the midplane was 0.15 m. The normal-mode density distribution used is shown in Fig. 8.

Next, a sloshing-ion distribution normalized to the same unit peak pressure was employed in the same cell. Finally, the normalized sloshing-ion distribution was employed in the cell the flux surface of which is shown in Fig. 6. The length of the cell, the flux surface radius at the mirror, and the mirror ratio were kept the same as for the Bessel-function cell. To represent a sloshing-ion distribution, a normal-mode distribution was multiplied by a weighting function that approximates the effect of off-angle injection of ions. The resultant normalized axial distribution of the plasma as it was used in the two mirror cells is depicted in Fig. 9.

As was noted, the value of the instability integral was calculated for three cases: (i) for the normal-mode distribution (Fig. 8) in the Bessel-function cell, (ii) for a sloshing-ion distribution (Fig. 9) in the same cell, and (iii) for a sloshing-ion distribution in the linear-taper cell of Fig. 6. To illustrate the gains achievable by the optimization of the flux surfaces and by the use of sloshing ions, Table 4 gives the value I_s of the stability integral for the three cases. The first entry is for the normal-mode case in the Bessel-function cell. The second entry is for the sloshing-ion distribution in the same cell. The third entry is for the sloshing-ion distribution in the linear-taper-coil cell of Fig. 6. For all cases, the mirror ratio was 4 : 1 and the plasma radius at the mirrors had the same value (0.075 m). All distributions were normalized to unity at their peak pressures so that

all would generate the same peak plugging potential in a tandem-mirror system.

It can be seen from Table 4 that a substantial reduction in the negative contribution to the stability integral can be achieved by using sloshing ions in a taper-coil cell as compared to either normal-mode or sloshing-ion distributions contained in a Bessel-function cell. This reduction comes about as a result of the combined effect of sloshing ions and the favorable shaping of the field lines that occurs when the cell employs the linear-taper configuration for the current in its field coils.

The example given above illustrates the kinds of reductions in destabilizing effect (reflected in reductions in the KS beam-power requirements) that are possible by shaping the flux surfaces in the end-cells of a tandem mirror employing KSs. In a 1988 paper concerning the GDT, Mirnov and Ryutov [18] employed variational analysis to determine the optimal shape of the flux surfaces in the mirror cell of the GDT, i.e., the shape that minimizes the negative contribution of this cell to the instability integral. Although, in the case that they treated, the plasma pressure was isotropic (owing to the high collisionality of the GDT operating regime), their analytical approach could also be applied to a sloshing-ion pressure distribution. In that way, even further gains than those presented here could no doubt be realized, within the limits imposed by engineering requirements in the construction of the field coils.

Although the discussion here has been centered on the optimization of the flux surfaces in the plug cells of a tandem mirror, the analysis by Mirnov and Ryutov [18] shows that the central cell can also be optimized with respect to minimizing its destabilizing contribution to the stability integral. There is however, perhaps another reason for specially shaping the flux surfaces of the central cell. The flux surfaces that were described above and illustrated in Fig. 6 are created by circular coils with a linearly increasing current as a function of distance from the midplane. The field lines, as noted, possess "good" curvature everywhere except near the midplane. Although, as far as is known, the stability analysis has not been performed for this type of mirror field configuration, it seems reasonable that such a shape of flux surface could help in suppressing a class of weakly driven modes of the "trapped-ion" [19] variety. These instabilities have their origin in inadequate electrical communication between the central cell, plug, and expander regions in the tandem mirror. Parenthetically, the elimination of thermal barriers, as proposed here, and the alternative expander designs (discussed in the next section) should go a long way toward eliminating this particular concern.

6. THE EXPANDER: ISSUES AND OPTIMIZATION

The design of the expander presents another opportunity for optimization, previously discussed in Section 4. It also involves some special issues relative to the "communication" requirement mentioned in Section 1. As was discussed, the generic requirements for optimization of the expander are to create an expanding flux surface that consists of a combination of conical (zero second derivative) and strong-positive-curvature flux surfaces, chosen to optimally accomplish the magnetic compression, stagnation, and reflection of ion beams injected (at optimally chosen angles of injection) into the expander. In the choice for the location of the positive-curvature region of the expander, there are two different approaches that can be taken. The first approach, the one that is illustrated in Fig. 5, involves the location of this region at a position that is intermediate between that of the ion sources (located close to the outer end of the expander) and the outer mirror of the plug cell. In this way, the stabilizing (positive) contribution to the instability integral arises from a combination of magnetic compression and exploitation of the radius-cubed term in the integrand of the integral. The potential disadvantage of using this means for optimization arises from the "communication" issue as it applies to the region of the expander between the location of the stabilizer plasma and the mirror. Since the distance between these two locations in the expander might be fairly large and since the density of the stabilizer plasma would be quite low, it would be necessary to insure that a sufficient density of high-conductivity plasma existed between the two to insure the easy flow of the stabilizing currents. This potential problem suggests the examination of an alternative way to optimize the effectiveness of the beam-produced stabilizer plasma as follows.

First, the expander is to be configured so that its outer conical region extends almost into the mirror region itself, changing abruptly there to a region of high positive curvature. Second, the ion beams are to be directed at smaller angles and with a smaller angular spread, so that they are strongly converged and compressed, being stagnated and reflected in the high-curvature region close to the mirror. In this way, although the radius-cubed enhancement effect is largely lost, sta-

Table 4

Cell type and density distribution	I_s	Ratio
Normal-mode distribution in the Bessel cell	-3.6×10^{-4}	1.0
Sloshing-ion distribution in the Bessel cell	-3.7×10^{-4}	1.03
Sloshing-ion distribution in the taper-coil cell	-1.4×10^{-4}	0.39

bilization strength is recovered through the greatly increased magnetic compression of the stabilizer beam ions. In an example where the magnetic compression factor was approximately 800 : 1, the value of the stability integral, I_s, was found to be +22.0. This value is nearly as large as the value that was obtained by injecting the same current of ions at larger angles into an expander of the shape shown in Fig. 5.

Some of the advantages of taking this alternate approach to the expander design are the following. First, the communication distance between the plug-cell plasma and the stabilizer plasma is much smaller than that for the alternative design. Second, the density of the stabilizer plasma, since it is much higher than that for the other case, will itself create a significant local potential peak. The formation of this potential peak will then be expected to result in the trapping of a low-density plasma between this peak and the mirror, still further enhancing the electrical communication between the stabilizer and the plug plasma. A third perceived advantage is that the electrons trapped by the potential peak could be heated by directed microwave beams, thus further enhancing the MHD stabilizing effect of the stabilizer plasmas.

7. CONCLUSION

Following a discussion of some prior examples, the discussions in Sections 5 and 6 illustrate some of the considerations that need to be taken into account in the design of the plug cells and the expanders for tandem-mirror systems with KSs. In the design of the plug cells, it was shown that significant gains in performance could be obtained by a combination of flux-surface shaping and the use of sloshing-ion distributions. The use of sloshing ions is further indicated for the suppression of the AIC mode in the plug cells. In the design of the expanders, which one of the two generic design philosophies (stabilizer plasma distant-from or close-to the mirrors) should be employed would depend on plasma physics and engineering/economic issues that can only be settled by more detailed analyses and computer simulations. Already, however, the approaches discussed above can be expected to result in a significant improvement in the performance of the "MINIMARS with KSs" that was reported in [6]. The next steps, now underway, will be to update "legacy" mirror MHD stability codes developed in the 1980s at Livermore, and apply them to the analysis of an axisymmetric tandem mirror with KSs, thereby extending the zeroth-order analyses given here to realistic, finite-beta examples. If these new studies validate the KS concept, they will provide additional motivation for a resurgence of work on mirror-based fusion systems as important contenders in the search for practical and economic approaches to fusion power.

ACKNOWLEDGMENTS

I wish to acknowledge with gratitude the help of D.D. Ryutov in discussions of plasma physics issues associated with the KS concept. This work was performed under the auspices of the U. S. Department of Energy by the University of California, Lawrence Livermore National Laboratory, under contract no. W-7405-Eng-48.

REFERENCES

1. L. Spitzer, *Physics of Fully Ionized Gases* (Interscience, New York, 1962).
2. M. N. Rosenbluth and C. L. Longmire, Ann. Phys. **1**, 120 (1957).
3. A. V. Anikeev, P. A. Bagrjanskj, B. N. Bocharov, *et al.*, in *Open Plasma Confinement Systems for Fusion*, Ed. by E. A. Kabantsev (World Scientific, Singapore, 1994), p. 283.
4. D. D. Ryutov, in *Proceedings of Workshop on Physics of Alternative Magnetic Confinement Schemes, Villa Monastero, Italy, 1987*, Ed. by S. Ortolani and E. Sindoni (Società Italiana di Fisica, Bologna, 1987), Vol. II, p. 791.
5. R. F. Post, Fusion Technol. **39**, 25 (2001).
6. R. F. Post, in *Current Trends in International Fusion Research: Proceedings of the Fourth Symposium, Washington, DC, 2001* (in press).
7. M. N. Rosenbluth, N. A. Krall, and N. Rostoker, Nucl. Fusion Suppl., Part 1 143 (1962).
8. R. W. Moir and R. F. Post, Nucl. Fusion **9**, 253 (1969).
9. Yu. V. Gott, M. S. Ioffe, and V. G. Tel'kovskii, Nucl. Fusion Suppl., Part 3 1045 (1962).
10. D. D. Ryutov and G. V. Stupakov, Pis'ma Zh. Éksp. Teor. Fiz. **26**, 186 (1977) [JETP Lett. **26**, 174 (1977)].
11. R. F. Post, Trans. Fusion Technol. **35**, 40 (1999).
12. R. F. Post, Nucl. Fusion **27**, 1579 (1987).
13. L. J. Perkins, B. G. Logan, R. B. Campbell, *et al.*, Fusion Technol. **8**, 685 (1985).
14. G. R. Smith, Phys. Fluids **27**, 1499 (1984).
15. T. I. Orzechowski, S. L. Allen, J. H. Foote, *et al.*, Phys. Fluids **26**, 2335 (1983).
16. T. Cho, M. Ichimura, M. Inutake, *et al.*, in *Proceedings of the 10th International Conference on Plasma Physics and Controlled Nuclear Fusion Research, London, 1984* (IAEA, Vienna, 1985); Nucl. Fusion Suppl. **2**, 275 (1985).
17. R. F. Post, Sixteen Lectures on Controlled Thermonuclear Reactions, Report UCRL-4231 (February 2, 1954) (unpublished).
18. V. V. Mirnov and D. D. Ryutov, in *Advances in Science and Technology, Series: Plasma Physics*, Ed. by V. D. Shafranov (VINITI, Moscow, 1988), Vol. 8, p. 77.
19. H. L. Berk and B. G. Lane, Phys. Fluids **29**, 3749 (1986).

Plasma Physics Reports, Vol. 28, No. 9, 2002, pp. 721–726. From Fizika Plazmy, Vol. 28, No. 9, 2002, pp. 783–789.
Original English Text Copyright © 2002 by Yatsu, Cho, Higaki, Hirata, Hojo, Ichimura, Ishii, Ishimoto, Itakura, Katanuma, Kohagura, Minami, Nakashima, Numakura, Saito, Saosaki, Takemura, Tatematsu, Yoshida, Yoshikawa.

MAGNETIC CONFINEMENT SYSTEMS

Recent Development in GAMMA 10 Experiment[1]

K. Yatsu, T. Cho, H. Higaki, M. Hirata, H. Hojo, M. Ichimura, K. Ishii, Y. Ishimoto, A. Itakura, I. Katanuma, J. Kohagura, R. Minami, Y. Nakashima, T. Numakura, T. Saito, S. Saosaki, Y. Takemura, Y. Tatematsu, M. Yoshida, and M. Yoshikawa

Plasma Research Center, University of Tsukuba, Tsukuba, Ibaraki 305-8577, Japan

Received March 4, 2002

Abstract—After the attainment of the density doubling due to the potential confinement, GAMMA 10 experiments have been directed to obtain a high-density plasma with potential confinement and also to study the dependence of the confining potential and confinement time on the plasma density. These problems are important to understand the physics of potential formation in tandem mirrors and also for the development of a tandem mirror reactor. GAMMA 10 experiments have advanced greatly after the Sorrento IAEA Conference, where high-density plasma production by using an ICRF heating at a higher harmonic frequency was reported. Recently, a high-density plasma was attained and the reproducibility of high-density plasma production was much improved by adjusting the spacing of the conducting plates installed in the anchor transition regions. In this paper, we report the production of a high-density plasma and the dependence of the confining potential and confinement time on the density up to a density of 4×10^{12} cm^{-3}. © *2002 MAIK "Nauka/Interperiodica".*

1. INTRODUCTION

The mirror concept was suggested in the early 1950s independently by G.I. Budker in the USSR and R.F. Post in the USA [1]. Ever since, many efforts have been continued toward the goal of fusion power by using the mirror concept. In the history of mirror research, many Russian works are admired for the great pioneering achievement. M.S. Ioffe *et al.* demonstrated the effectiveness of the minimum-*B* field for suppressing MHD instability [2, 3]. After that, the concept of the minimum-*B* field became one of the guiding principles in fusion researches. The idea of the tandem mirror was proposed first in the world in Russia [4, 5]. D.A. Panov is another great pioneer in mirror research. He constructed first in the world the superconducting thermonuclear installations OGRA-3 [6] and OGRA-3B [7]. He pioneered the works on magnetic field confining properties—the orthogonal magnetic field, "Panov's" coordinates, and other ideas. He contributed to successful experiments on feedback stabilization of instabilities [8]. This paper is dedicated to the achievement of D.A. Panov.

In the GAMMA 10 tandem mirror, plug and thermal barrier potentials of 1.7 and 1.1 kV have been attained with a plasma confinement time of 0.6 s for a plasma with an ion temperature of 0.5 keV [9]. In this experiment, plasma heating was mainly electron cyclotron resonance heating (ECRH) and an ion temperature was about 0.5 keV. Then, ion heating power in the ion cyclotron range of frequency (ICRF) was increased and an ion temperature of 10 keV was attained [10]. We mentioned this heating scenario as a hot-ion mode. However, a density increase due to the potential confinement was less than 10%. This situation was much improved by axisymmetrization of the heating patterns of ECRH for potential formation [11] and of ICRF heating [12]. A further improvement of confinement was made by installing conducting plates in anchor transition regions. The central-cell density and the diamagnetism were doubled due to those improvements [13]. After this attainment, GAMMA 10 experiments have been directed to obtain a high-density plasma with potential confinement and also to study the dependence of the confining potential and confinement time on the plasma density. These problems are important for understanding the physics of potential formation in tandem mirrors and also for the development of a tandem mirror reactor. We reported a high-density plasma production by using higher harmonic ICRF heating in the last ICPP Conference [14] and IAEA Conference [15]. Recently, a higher density plasma was attained and the reproducibility of the high-density plasma production was much improved than the plasma reported before. This improvement was attained by adjusting the spacing of the conducting plates installed in the anchor transition regions [13]. In this paper, we report on the recently obtained high-density plasma and the dependence of the confining potential and the confinement time on the density up to a density of 4×10^{12} cm^{-3}.

2. GAMMA 10 TANDEM MIRROR

The GAMMA 10 tandem mirror consists of a central cell, two anchor cells, and two end mirror cells. The anchor cells with a minimum-*B* configuration are located at both ends of the axisymmetric central cell

[1] This article was submitted by the authors in English.

1063-780X/02/2809-0721$22.00 © 2002 MAIK "Nauka/Interperiodica"

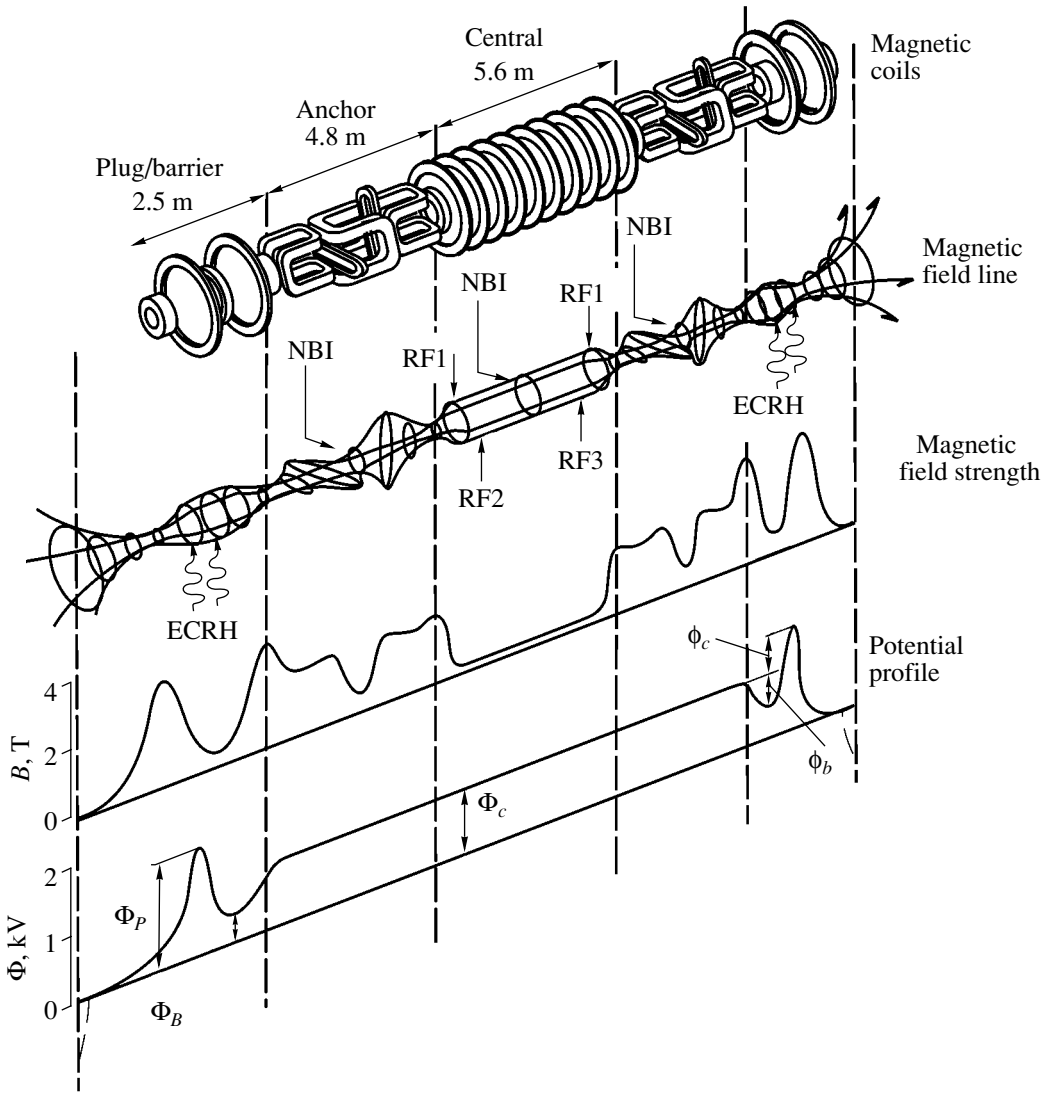

Fig. 1. GAMMA 10 coil system, shape of magnetic flux tube with heating systems, axial magnetic-field strength, and axial distribution of the plasma potential.

and are connected to the axisymmetric end mirror cells. The central cell has a length of 5.6 m, and the magnetic-field intensity at the midplane is 0.4 T with a mirror ratio of 5.2. The plug/barrier cell has a length of 2.5 m, and the magnetic-field intensity at the midplane is 0.5 T with a mirror ratio of 6.2. Regions between the axisymmetric field and the minimum-B field are mentioned as transition regions. The initial plasma is produced by magneto-plasma-dynamic plasma guns located at both ends. A slow ion cyclotron wave (RF1: 9.9 MHz) excited by Nagoya type III antennas installed near both ends of the central cell is used for plasma production with hydrogen gas puffing in the central cell. Ions in the central cell are heated by ICRF (RF2: 6.3 MHz) power applied to a double half-turn (DHT) antenna. A higher harmonic ICRF (RF3: 36–76 MHz) power applied another DHT antenna is used to obtain a higher density plasma. A neutral beam injection (NBI: 25 kV, 30 A) started last year for plasma heating and production in the central cell. A plasma confining potential is produced by electron cyclotron resonance heating (ECRH) in the plug/barrier region. Figure 1 shows the magnetic-field coils, the shape of the magnetic flux tube with heating systems, the axial magnetic-field strength, and the axial distribution of the plasma potential.

For plasma diagnostics, plasma densities in the central cell, anchor cells, and plug/barrier cells are measured by using microwave interferometers. The end-loss ion current and the ion energy spectrum at the end are measured by using an end-loss ion-energy analyzer (ELA) [16]. Plasma potentials in the central cell and in the barrier region of the plug/barrier cell are measured

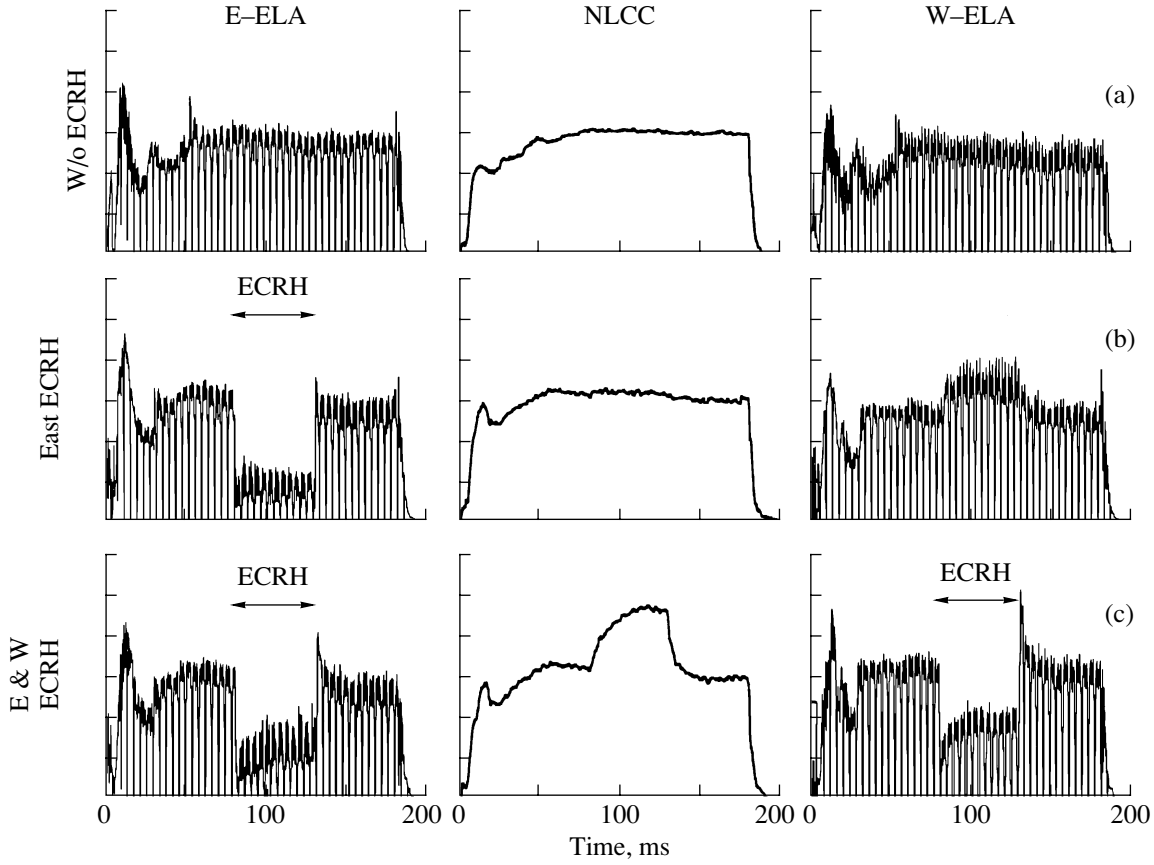

Fig. 2. Central-cell line density (NLCC) and end-loss ion current to the east (E–ELA) and the west (W–ELA) ends for (a) the case without ECRH, (b) only east ECRH, and (c) both east and west ECRH.

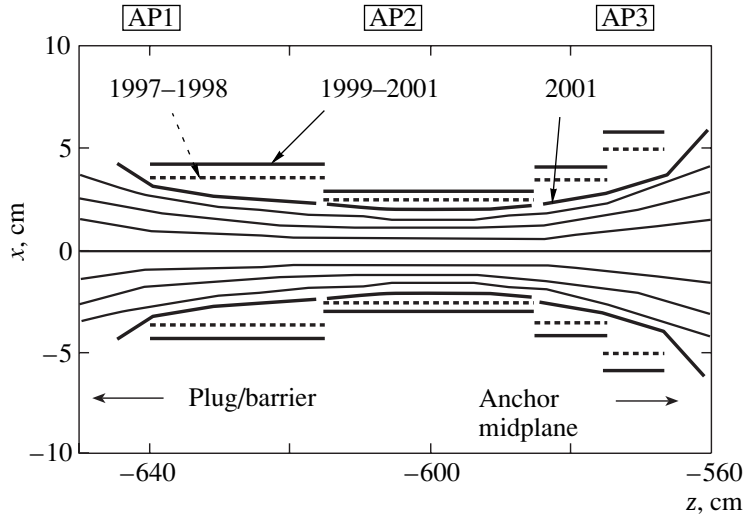

Fig. 3. Cross-sectional view of anchor conducting plates. In the case of AP1 (used in 1997–1998) and AP2 (used in 1999–2001), flat plates are arranged at a different axial location from the axis. New anchor plates AP3 are curved along magnetic field lines and are located close to the plasma. The thickness of the fanning magnetic flux corresponding to the 30-cm-diameter flux tube in the central cell is 2.7 cm at $z = -600$ cm (from central cell midplane to the west direction).

by using beam probes [17]. The plasma potential in the plug region is determined by analyzing the energy of the end-loss ions measured with the ELA. The plasma confinement potential is determined as the potential difference between the potentials in the plug region and central cell.

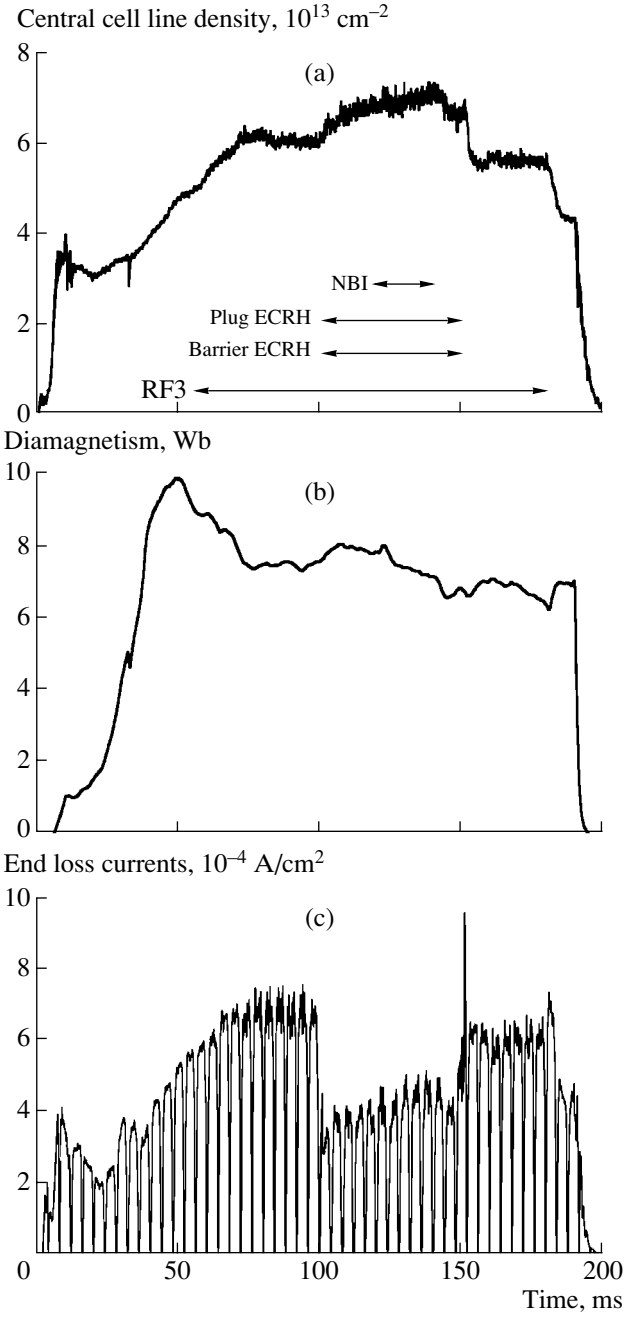

Fig.4. Waveforms of (a) central-cell line density, (b) diamagnetic signal, and (c) end-loss ion current.

3. HIGH-DENSITY PLASMA PRODUCTION AND CONFINEMENT IN GAMMA 10

Potential confinement was studied under various heating scenarios, such as without ECRH, with ECRH at one end, and with ECRH at both ends. Figure 2 shows the waveforms of the central cell line densities and end-loss ion currents, where NLCC denotes the central cell line density and E-ELA and W-ELA indicate end-loss currents to the east and west ends. When ECRH is not applied, NLCC and E- and W-ELA have similar waveforms indicating that the plasma is mainly lost to the ends. Actually, we measured that about 85% of the produced plasma was lost in the axial direction globally and the ratio was higher in the core region defined as inside the FWHM of the density profile. When ECRH is applied only to the east plug, the ion current to E-ELA decreases owing to the potential reflection of low energy ions, while the ion current to W-ELA increases owing to the ions reflected due to the east plug potential; NLCC does not increase. When ECRH is applied to both plugs, NLCC increases as a result of potential confinement. This experiment clearly indicates the potential confinement in the tandem mirror. With the potential confinement, we attained doubling of the density indicating about a fourfold increase in the axial particle confinement time near the axis [13].

After the attainment of the density doubling, it was observed that a density higher than 2.5×10^{12} cm^{-3} was difficult to be achieved with and without potential confinement due to a density clamping mechanism. Although this mechanism has not been made clear yet, a higher density plasma was obtained by higher harmonic ICRF heating (RF3) [14]. In addition to the RF3 power, the central cell NBI made the plasma density higher. An important contribution in the high density plasma production was the adjustment of the spacing of the conducting plates installed in the anchor transition regions. Figure 3 shows the cross sectional view of the conducting plates arrangement. In the figure, the former conducting plates (AP1 and AP2) are also indicated. The new conducting plates (AP3) are curved along magnetic field lines and located close to the plasma. Figure 4 shows the waveforms of (a) the central cell line density, (b) diamagnetic signal, and (c) end-loss ion current measured by ELA. The ELA is used in a bias-scanning operational mode and the envelope of the signal traces the end-loss ion current. In Fig. 4a, the line density increases by 30% by applying RF3 power at 100 kW. In the experiment without RF3, the line density was saturated at about 4.5×10^{13} cm^{-3} even if the RF1 power was increased to higher than 100 kW. So, the higher harmonic ICRF heating is efficient for higher density plasma production. The line density increases further due to the potential confinement by applying ECRH. The FWHM of the line density profile was 19 cm and the plasma density on the axis was $n(0) = 3.5 \times 10^{12}$ cm^{-3} when the line density was 7×10^{13} cm^{-2}. The decrease in the diamagnetic signal with applying RF3 is not well explained yet. The increase in the diamagnetic signal with ECRH and NBI is not large, but the increase becomes larger as the wall conditioning progresses more with plasma shots. The ion temperature was determined from the diamagnetic signal and also by energy analysis of charge-exchange neutrals. The ion distribution was anisotropic with a perpendicular (with respect to the magnetic field) temperature of 3 keV and parallel temperature of 0.3 keV. The electron temperature was 0.08 keV. The particle confinement

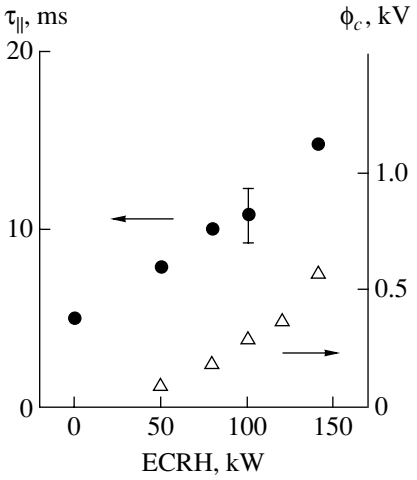

Fig. 5. Particle confinement time $\tau_\parallel$ (closed circles) and confining potential ϕ_c (triangles) vs. plug ECRH power (at one end).

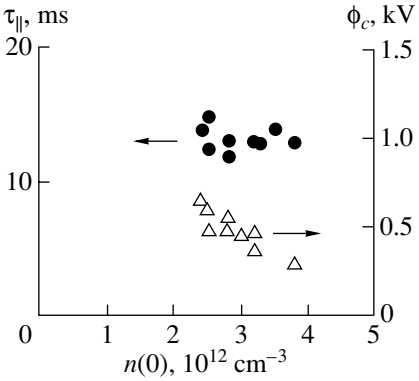

Fig. 6. Axial confinement time $\tau_\parallel$ (closed circles) and plasma confining potential ϕ_c (triangles) vs. plasma density for a plug ECRH power of 140–150 kW.

time parallel to the magnetic field $\tau_\parallel$ is determined as $\tau_\parallel = eN/I_{\text{loss}}$, where e is the unit charge, N is the total number of ions in a flux tube, and I_{loss} is the end loss current from the flux tube measured by ELA. Figure 4c shows the current density at the measurement position. For the end loss current corresponding to the flux tube in the central cell, the ELA current is multiplied by a factor of 40 corresponding to the ratio of magnetic field strength between the central cell and ELA position. Just before applying ECRH, i.e., without confining potential, a particle confinement time parallel to the magnetic field was 5 ms and the radial confinement time was estimated to be longer than 30 ms. Those confinement times of the ICRF-sustained plasma correspond to the mirror confinement time in the GAMMA 10 magnetic field. The parallel confinement time was increased about three times due to the potential confinement, but the radial confinement time decreased by about 30%, with the result that the density increase on the axis was about 30% in this shot.

Figure 5 shows an increase in the plasma confining potential ϕ_c and axial particle confinement time $\tau_\parallel$ with ECRH power for a plasma with a relatively low density of about 1.5×10^{12} cm^{-3}. At a plug ECRH power of 140 kW, a confining potential of 550 V was produced and the plasma density increased from 1.3×10^{12} to 2.5×10^{12} cm^{-3} due to the potential confinement. Figure 6 shows the axial confinement time and confining potential versus plasma density. In contrast to the confinement time, the confining potential tends to decrease with the density. Such behavior requires a more detailed study. The potential formation mechanism is theoretically studied by means of Monte Carlo simulation [18]. In this model, however, the potential depends only on the profile but not on the absolute value of the density. Therefore, we are to study the dependence of the potential on density experimentally. The magnitude of the confining potential depends strongly on the anisotropy of the plug electron distribution function. The electron velocity anisotropy is considered to be relaxed as the plasma density increases. Then, the decrease in the confining potential with the plasma density is as expected. The density range in Fig. 6 is not wide, and we need more experiments in order to obtain a functional relation between them.

4. SUMMARY

A high-density plasma has been obtained with good reproducibility, and we expect an increase in the ion temperature with progress of wall conditioning. The dependence of the confining potential and confinement time on the density was studied in the high-density plasma, but we need more experiments in order to obtain a functional relation between them. A further increase in the density and longer sustainment of a high-density plasma are the next problems to be studied.

REFERENCES

1. D. D. Ryutov, Nucl. Fusion **20**, 1068 (1980).
2. M. S. Ioffe, R. I. Sobolev, V. G. Tel'kovskii, and E. E. Yushmanov, Zh. Éksp. Teor. Fiz. **39**, 1602 (1960) [Sov. Phys. JETP **12**, 1117 (1961)].
3. Yu. V. Gott, M. S. Ioffe, and V. G. Tel'kovskii, Nucl. Fusion Suppl. **3**, 1045 (1962).
4. G. I. Dimov, V. V. Zakaidakov, and M. E. Kishinevskii, Fiz. Plazmy **2**, 597 (1976) [Sov. J. Plasma Phys. **2**, 326 (1976)].
5. T. K. Fowler and B. G. Logan, Comments Plasma Phys. Control. Fusion **2**, 167 (1977).
6. V. A. Zhil'tsov, V. Kh. Likhtenshtejn, D. A. Panov, *et al.*, in *Proceedings of the 5th International Conference on Plasma Physics and Controlled Nuclear Fusion Research, Tokyo, 1974* (IAEA, Vienna, 1975), Vol. 1, p. 355.

7. V. A. Zhil'tsov, P. M. Kosarev, V. Kh. Likhtenshtejn, *et al.*, in *Proceedings of the 7th International Conference on Plasma Physics and Controlled Nuclear Fusion Research, Innsbruck, 1978* (IAEA, Vienna, 1979); Nucl. Fusion Suppl. **2**, 469 (1979).
8. D. A. Panov, Pis'ma Zh. Éksp. Teor. Fiz. **35**, 70 (1982) [JETP Lett. **35**, 82 (1982)].
9. S. Miyoshi, T. Cho, H. Hojo, *et al.*, in *Proceedings of the 13th International Conference on Plasma Physics and Controlled Nuclear Fusion Research, Washington, DC, 1990* (IAEA, Vienna, 1991); Nucl. Fusion Suppl. **2**, 539 (1991).
10. T. Tamano, T. Cho, M. Hirata, *et al.*, in *Proceedings of the 15th International Conference on Plasma Physics and Controlled Nuclear Fusion Research, Seville, 1994* (IAEA, Vienna, 1995), Vol. 2, p. 399.
11. T. Saito, Y. Tatematsu, Y. Kiwamoto, *et al.*, Fusion Eng. Des. **53**, 267 (2001).
12. M. Ichimura, H. Hojo, K. Ishii, *et al.*, Nucl. Fusion **39**, 1995 (1999).
13. K. Yatsu, L. G. Bruskin, T. Cho, *et al.*, Nucl. Fusion **39**, 1707 (1999).
14. M. Ichimura, T. Cho, M. Hirata, *et al.*, Phys. Plasmas **8**, 2066 (2001).
15. K. Yatsu, T. Cho, M. Hirata, *et al.*, Nucl. Fusion **41**, 613 (2001).
16. Y. Sakamoto, T. Cho, M. Hirata, *et al.*, Rev. Sci. Instrum. **66**, 4928 (1995).
17. K. Ishii, M. Kotoku, T. Segawa, *et al.*, Nucl. Fusion **30**, 1051 (1990).
18. I. Katanuma, Y. Tatematsu, K. Ishii, *et al.*, J. Plasma Fusion Res. **77**, 1085 (2001).

Plasma Physics Reports, Vol. 28, No. 9, 2002, pp. 727–733. From Fizika Plazmy, Vol. 28, No. 9, 2002, pp. 790–797.
Original English Text Copyright © 2002 by Ichimura, Higaki, Saosaki, Kano, Kakimoto, Tokumoto, Yamaguchi, Hojo, Inutake, Yatsu.

MAGNETIC CONFINEMENT SYSTEMS

ICRF Heating in Magnetic Mirror Plasmas[1]

M. Ichimura*, H. Higaki*, S. Saosaki*, H. Kano*, S. Kakimoto*, K. Tokumoto*, Y. Yamaguchi*, H. Hojo*, M. Inutake, and K. Yatsu***

**Plasma Research Center, University of Tsukuba, Tsukuba, Ibaraki 305-8577, Japan*

***Graduate School of Engineering, Tohoku University, Sendai 980-8579, Japan*

e-mail: ichimura@prc.tsukuba.ac.jp

Received March 4, 2002

Abstract—Waves in the ion cyclotron range of frequency are efficiently used to produce and heat magnetic mirror plasmas. In relatively low-density (lower than 10^{18} m^{-3}) plasmas, the fast Alfvén eigenmodes are formed in radial and axial directions and the excitation of these modes is strongly affected by the density. The slow Alfvén waves are also effectively used for plasma heating. The ion temperature above 10 keV is achieved, which is confirmed by the detection of fusion neutrons. The excitation of Alfvén eigenmodes is studied in the GAMMA 10 tandem mirror. © *2002 MAIK "Nauka/Interperiodica".*

This manuscript is dedicated to Dr. D.A. Panov and his pioneer works on magnetic mirror research.

1. INTRODUCTION

Plasma heating with waves in the ion cyclotron range of frequency (ICRF) is widely used in fusion devices. In tokamaks, fast Alfvén waves are mainly used to heat large-size and high-density plasmas. In fusion-oriented mirror devices [1–3], slow Alfvén waves with a fundamental ion cyclotron resonance frequency are effectively used for the heating of low-density plasmas in magnetic field configurations with axial profiles. ICRF waves are also used for the initial plasma production in the mirror and stellarator devices [4]. GAMMA 10 is an axisymmetrized tandem mirror with a thermal barrier [5–8]; it consists of five mirror cells, which are a central cell, minimum-*B* anchor cells, and plug/barrier cells at both ends. The length of the central cell between mirror throats is 5.8 m, and the diameter of the stainless-steel vacuum vessel is 1 m. Magnetic field strength at the midplane of the central cell is 0.41 T, and the mirror ratio is 5 in a standard mode of operation. A limiter 0.36 m in diameter is set near the midplane. The anchor cells have a minimum-*B* mirror field configuration and are located at both sides of the central cell. The anchor cells play a role of MHD-stabilizers. The magnetic field strength is 0.61 T at the midplane, and the mirror ratio is 3. The plug/barrier cells are located at both ends of GAMMA 10, where a thermal barrier and plug potentials are produced. In the central cell of GAMMA 10, ICRF waves are used successfully for plasma production and heating. The high ion temperature plasma above 10 keV was achieved and sustained stably with ICRF heating. Typical plasma parameters on the axis are the following: the density is 2×10^{18} m^{-3}, the ion temperature is 5 keV, and the electron temperature is 100 eV.

The plasma production with ICRF waves is used not only in fusion experiments but also in plasma applications. In this paper, experiments on the plasma production and heating, as well as the characteristics of the waves excited in the mirror field configuration, are reported.

2. SETUP OF ICRF EXPERIMENTS ON GAMMA 10

Figure 1 shows the axial profile of the magnetic field line and strength and a schematic of ICRF antennas installed in the central cell. The axial coordinate is counted from the midplane of the central cell, where $z = 0$. The negative values of z correspond to the east side of the device. Two kinds of ICRF antennas are installed near the mirror throats of the central cell. The first kind is the so-called Nagoya type III antennas (Type III) [9], which are installed at $z = \pm 2.2$ m, where the mirror ratio R is 1.6. The four plate elements of Type III consist of two pairs, one with vertical plates and the other with horizontal plates, in order to generate a rotating electromagnetic field. Another is conventional double half-turn antennas (DHTs) installed at $z = \pm 1.7$ m, where $R = 1.1$. Three ICRF systems (RF1, RF2, and RF3) are now in operation. Principally, Type III are driven by the RF1 system and are used for plasma production in the central cell and ion heating in the anchor cell [2]. The frequency is adjusted to the ion cyclotron frequency near the midplane of the anchor cell. Fast Alfvén waves which are launched by Type III propagate through a flux tube with an elliptical cross section between the central and anchor cells and are converted to slow Alfvén waves [10, 11]. DHTs are

[1] This article was submitted by the authors in English.

1063-780X/02/2809-0727$22.00 © 2002 MAIK "Nauka/Interperiodica"

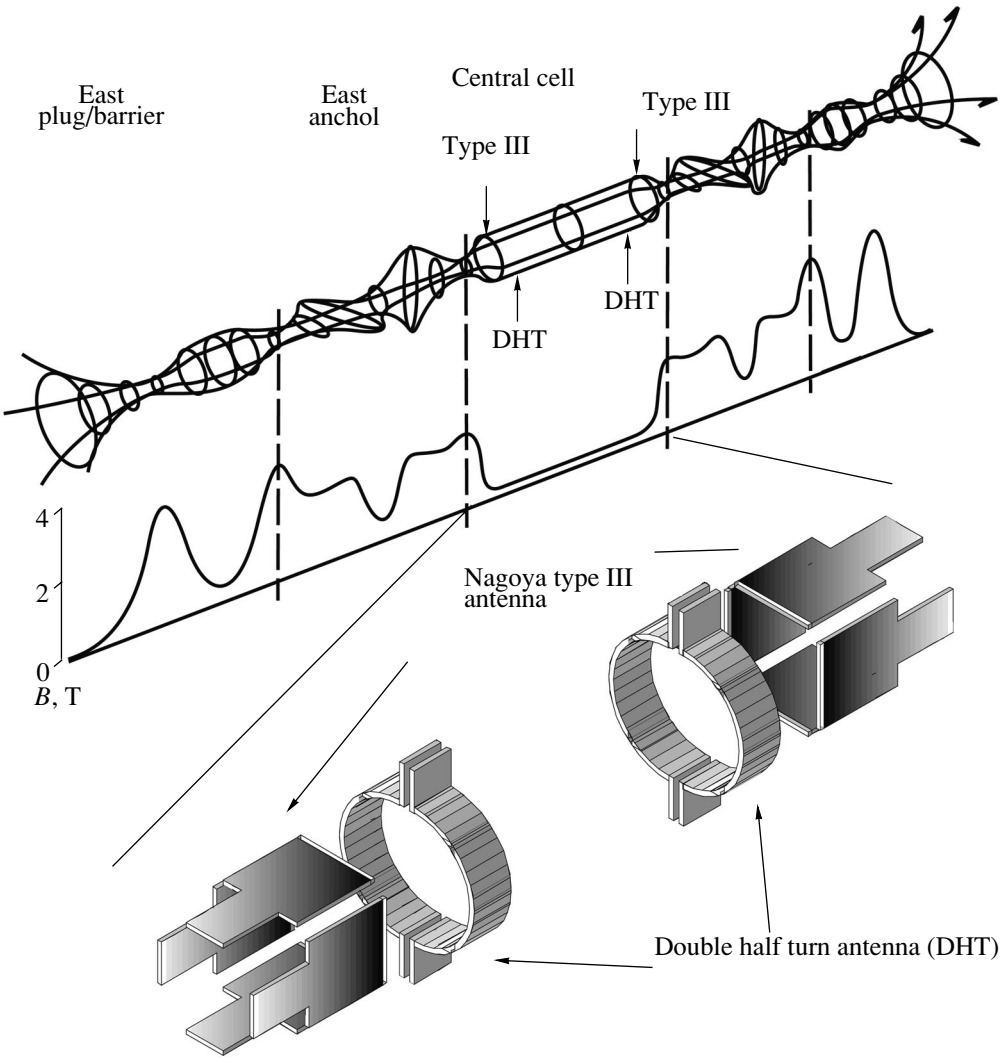

Fig. 1. Axial profiles of the magnetic field line and strength in GAMMA 10 and a schematic of the ICRF antennas.

driven by RF2 and are used for the main plasma heating in the central cell. The frequency is adjusted to the ion cyclotron frequency near the midplane of the central cell. The plasma is started up by injecting pulsed (1 ms) gun-produced plasmas from both ends and is sustained by applying RF1 and RF2 in combination with hydrogen gas puffing in the central cell. To avoid energy loss due to charge exchange, the gas is puffed near the mirror throats, where less hot ions exist. In mirror plasmas, ions which are heated in the perpendicular direction are deeply trapped near the midplane. RF1 and RF2 have two final outputs for both sides of antennas. The total radiated powers from Type III and DHTs are typically 100 kW with a duration of 200 ms, respectively. RF3 is a newly constructed system, which is used for the production of high-density plasma [12]. The RF3 system uses Type III or DHTs according to the experimental purpose. The maximum power and duration, as well as the frequency range of each ICRF system, are listed in the table.

Parameters of ICRF systems in GAMMA 10

	max power, kW	max duration, ms	Frequency range, MHz
RF1	300×2	500	7.5–15
RF2	300×2	500	4.4–9.6
RF3	200	500	36–76

In GAMMA 10, a plasma with a temperature anisotropy between perpendicular and parallel directions to the magnetic field is produced during strong ICRF heating. Temperature anisotropy is measured by using a diamagnetic loop array installed at $z = -0.33, \pm 1.5$, and 1.95 m. Mirror ratios at the location of each diamagnetic loop are 1.01, 1.08, and 1.26, respectively. From diamagnetic loops installed at $z = \pm 1.5$ m, it is determined that the axial pressure profile of the central cell is symmetric with respect to the midplane. Diamagnetic

loops are also installed in the midplane of both anchor cells.

3. EIGENMODES IN THE AXIAL AND AZIMUTHAL DIRECTIONS

Figure 2 shows the axial profiles of the magnetic field strength and the ω/Ω_{ci} values, which are determined from the magnetic field strength and applied frequencies of RF1 and RF2, where ω is the angular frequency of RF1 and RF2 and Ω_{ci} is the local ion cyclotron angular frequency. The locations of both antennas are also indicated. As is shown in Fig. 2, Type III are driven at a frequency close to the fundamental cyclotron frequency at the antenna location. Under the present experimental conditions, i.e., the relatively low density and the small radius, a fast wave eigenmode with an azimuthal mode number $m = +1$ is only excited. This mode satisfies the boundary conditions in the radial direction. The dispersion relation of the $m = +1$ fast wave that is excited in cylindrical and uniform plasmas with a vacuum layer between plasma and conducting wall is indicated in Fig. 3. It is calculated for a frequency of 9.9 MHz; a magnetic field strength of 0.41 T; and plasma and wall radii of 0.18 and 0.5 m, respectively. Because the $m = +1$ fast wave experiences no cut-off [13] in this region, it can propagate all over the GAMMA 10 device. When RF1 antennas installed at both ends of the central cell are driven at the same frequency, excited fast waves interact with each other. The interaction between the excited waves depends strongly on the plasma density because the wavelength changes under the fixed frequency condition. As was previously explained, these fast waves excited in the central cell can also propagate in the end direction and are converted into slow waves in the region between the central and anchor cells. The converted slow waves propagate to the anchor cell and heat ions in the fundamental cyclotron resonance layer. Then, the effect of the fast wave excitation in the central cell appears in the diamagnetic signals in both the east and west anchor cells. Figure 4 shows the temporal evolution of both diamagnetic signals in the east and west anchor cells. The temporal behavior of both signals shows the out-of-phase dependence of the density because the density is changing during the discharge. This interference indicates that the anchor cell beta, which is defined as the ratio of the plasma pressure to the magnetic field pressure, can be controlled by changing the phase difference between both antennas in the central cell. Figure 5 shows the phase dependence of both the east and west anchor diamagnetic signals under a fixed central cell line density of 2.5×10^{17} m^{-2}. The powers that are carried to the anchor cells are written as described in [9]:

$$\frac{P_E}{P_0} = 1 + \cos(k_z d - \delta), \quad (1)$$

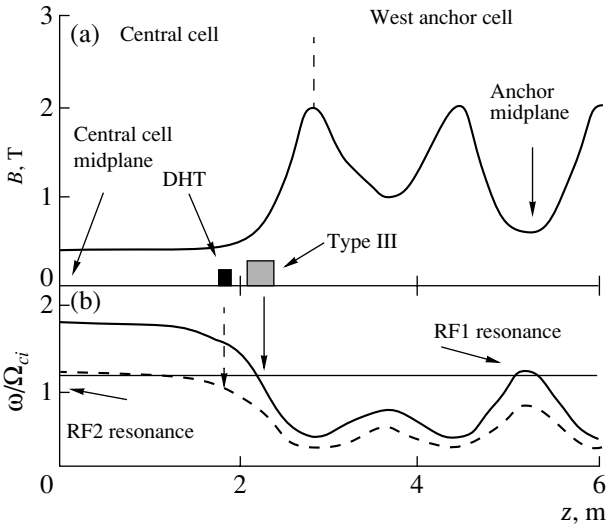

Fig. 2. (a) Axial profile of the magnetic field strength in the central and anchor cells and the location of ICRF antennas; (b) ω/Ω_{ci} values determined from the magnetic field strength and the applied frequency.

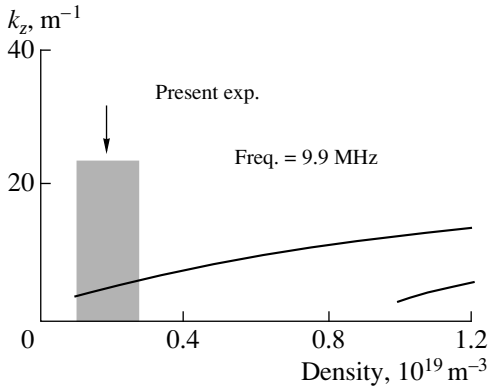

Fig. 3. Dispersion relation of an $m = +1$ fast wave in a uniform cylindrical plasma surrounded by vacuum. Parameters of RF1 are used, and the present experimental region is indicated.

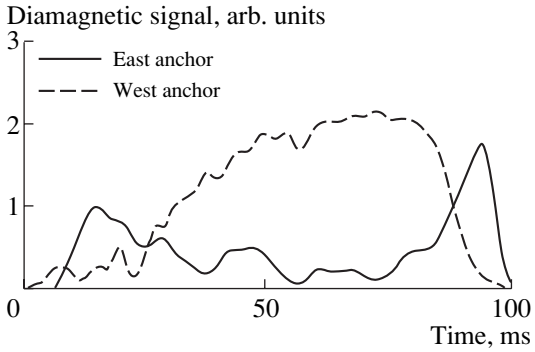

Fig. 4. Time evolution of the diamagnetic signals in both the east and west anchor cells when both the east and west RF1 antennas are driven at the same frequency.

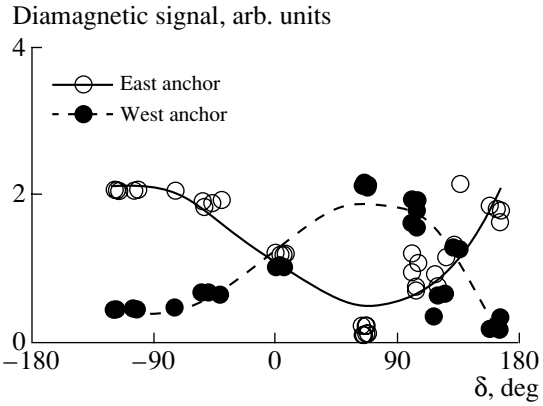

Fig. 5. Anchor diamagnetic signals when the phase difference between RF1 antennas is changed at a fixed line density of 2.5×10^{17} m^{-2}. Open and solid circles indicate the signals in the east and west anchor cells, respectively.

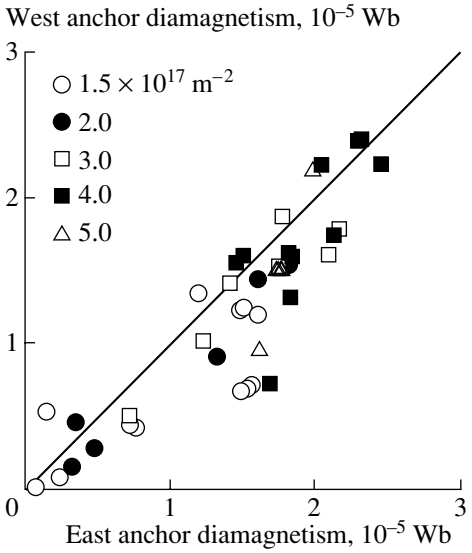

Fig. 6. Diamagnetic signals in the east and west anchor cells for different line densities in the central cell.

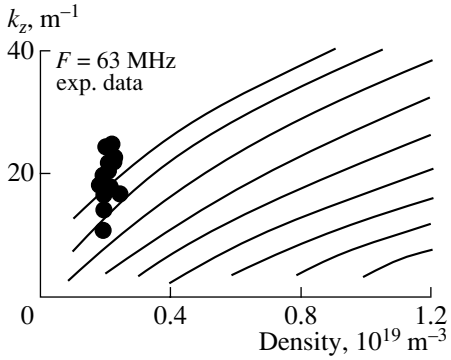

Fig. 7. Dispersion relation of $m = +1$ fast waves calculated for a frequency of 63 MHz. Solid circles represent the experimental data from magnetic probes.

$$\frac{P_W}{P_0} = 1 + \cos(k_z d + \delta), \quad (2)$$

where P_E and P_W are the powers to the east and west anchors, respectively; P_0 is the power to both anchors when there are no interactions; and k_z, d, and δ are the axial wavenumber, the distance between both antennas, and the phase difference, respectively. As is clearly seen from Eqs. (1) and (2), we can choose optimum conditions for the MHD stability, in which case the total power becomes $2P_0$ by controlling the phase difference. However, it is difficult to control the anchor beta when the density is automatically changed by improving the particle confinement due to the potential formation. There will be a possibility to use the feedback control of the phase difference from the viewpoint of optimization of the anchor beta. In recent experiments in GAMMA 10, RF1 with different frequencies in the east and west Type III is used in order to avoid the interference. Figure 6 shows the east and west anchor diamagnetic signals as functions of the line density when frequencies of 9.9 and 10.3 MHz are used for the east and west antennas, respectively. The amplitude of both diamagnetic signals becomes almost the same when the line density changes from 1.5×10^{17} to 5×10^{17} m^{-2}. The controllability of the plasma has been improved.

In mirror plasmas, the magnetic field strength and the plasma parameters are nonuniform in the axial direction. The excited waves will be affected by this nonuniformity and will form eigenmodes also in the axial direction even though RF1 with different frequencies in the east and west sides is used. These eigenmodes also depend strongly on the density. The existence of such axial eigenmodes means that the amplitude of the wave field becomes strong discretely as the density changes. As is indicated in Fig. 3, only one radial eigenmode is excited in the given parameter region. Then, it will be difficult to keep the excitation of the wave continuously with increasing density. If there is a large gap between the densities at which axial eigenmodes are excited, the density will be clamped. Recently, an ICRF system with a frequency in the high-harmonic fast wave (HHFW) region is introduced to improve such a discrete excitation of eigenmodes. Figure 7 shows the calculated dispersion curves of $m = +1$ fast waves which are excited in the cylindrical plasma under a fixed frequency close to ten ion cyclotron frequencies. It is seen that several modes can be excited under the given experimental conditions. It is expected that the density clamping due to the axial eigenmode formation by RF1 is improved and the density increases more smoothly because eigenmodes will be excited at various densities by RF3. Figure 8 shows a typical time evolution of the line density and diamagnetism with RF3. The RF1 power is fixed at 180 kW and a line density of 4×10^{17} m^{-2} is sustained. The ion temperature of several keV is achieved with RF2. RF3, which has a fre-

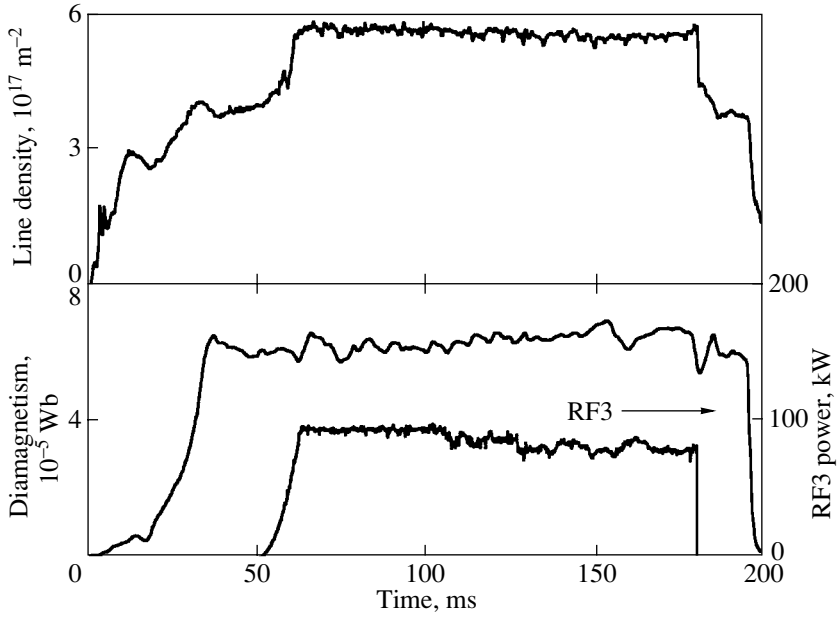

Fig. 8. Typical temporal evolution of the line density and diamagnetic signals when RF3 is applied. The RF1 power is fixed at 180 kW.

quency of 63 MHz, is superposed from 50 ms as indicated in Fig. 8. A clear increase above 40% in the line density is observed. When the RF1 power was further increased under the fixed conditions, i.e., the same amount of gas puffing, the same RF2 power, and so on, we observed little increase in the line density above 4×10^{17} m^{-2}. In the previous experiments, in which a large amount of gas puffing was used, we have observed the line density increase up to 2×10^{18} m^{-2} accompanied with a significant reduction of diamagnetism [14]. In the RF3 case, no reduction in diamagnetism is observed with increasing line density and the ion temperature is kept at several keV. The density profile measurements indicate that the density increases mainly in the core region. The wavenumber of the excited waves is measured with a magnetic probe array installed at the peripheral region of the central cell. Obtained wavenumbers are plotted in Fig. 7, and the waves with the fundamental radial mode are detected.

4. HOT ION MODE WITH ICRF HEATING

As was explained previously, DHTs located near both ends of the central cell are driven by RF2 with a frequency of 6.36 MHz and launch slow Alfvén waves for the ion heating in the central cell. Although both DHTs are driven at the same frequency, no interferences are observed because the fundamental cyclotron resonance layers exist between both antennas and slow waves cannot propagate through the central cell midplane. When we arrange experimental conditions carefully, the diamagnetic signal, which is the information of mainly the ion pressure, increases with the radiated power from RF2 antennas. Figure 9 shows the radiated-power dependence of the diamagnetic signals at different magnetic field strengths. The plasma pressure increases almost linearly with the RF2 power. Since the dependence is almost the same for each magnetic field, the ion pressure is nearly proportional to the magnetic field strength. The highest ion temperature above 10 keV was achieved at the highest field of 0.57 T. When the output power of RF2 is further increased, the radiated power from the antenna tends to saturate. It means that the loading resistance decreases in the high-power region. As was noted above, the mirror ratio at the DHT location is 1.1. The central cell beta increases

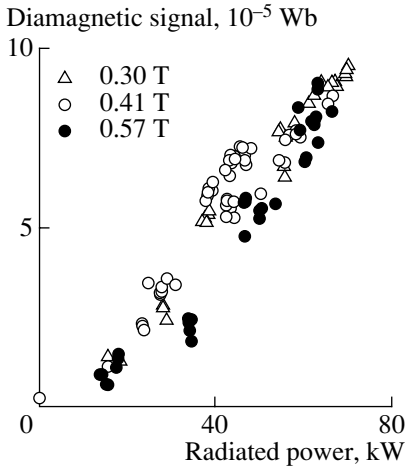

Fig. 9. Diamagnetic signals in the central cell vs. RF2 radiated power for different magnetic field strengths.

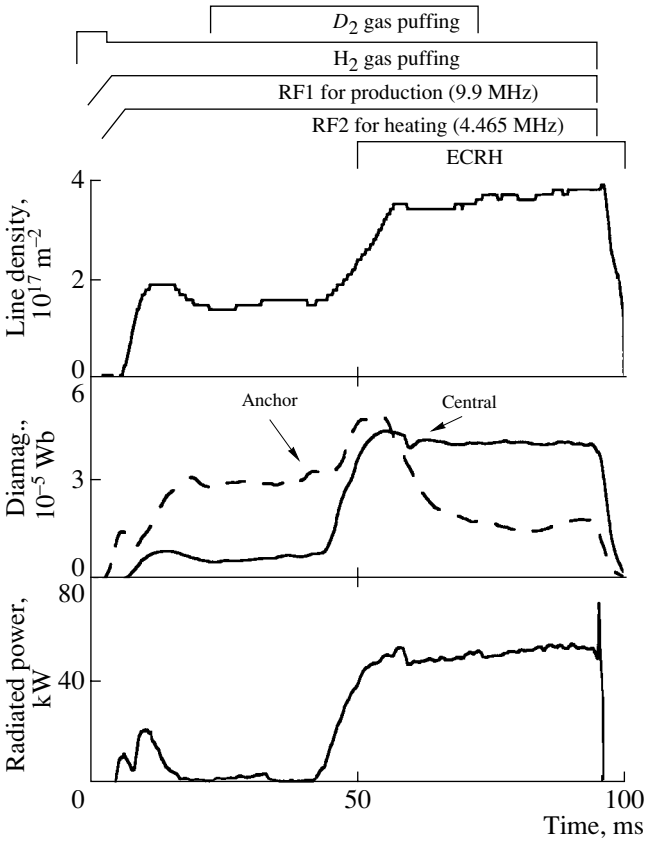

Fig. 10. Typical temporal evolution of the plasma parameters in experiments with a hydrogen–deuterium mixture.

with increasing RF2 power; when it becomes several percent, the magnetic field profile changes, which strongly affects the propagation of the excited slow waves. The other possible reasons for the reduction of the loading resistance is the MHD instability of the plasma. The loading resistance is affected by the MHD activity near the antenna region. It will be required to increase the anchor beta. These MHD-related issues will be discussed in other manuscripts.

The achievement of the ion temperature above 10 keV is confirmed by the emission of fusion neutrons in the deuterium plasma [15]. To keep the axisymmetrized configuration, the magnetic field strength of the anchor cell and the RF1 frequency are chosen to satisfy the fundamental cyclotron resonance condition for proton plasma. A target proton plasma is sustained by RF1 with a frequency of 9.9 MHz. The magnetic field strength in the central cell and the RF2 frequency (4.465 MHz) are chosen to satisfy the fundamental cyclotron resonance condition for deuterium plasma. Figure 10 shows the typical temporal evolution of plasma parameters in the deuterium experiment and a time sequence of the heating system. The time evolution of the radiated power of RF2 is also indicated. Initially, the proton plasma is sustained by applying RF1 and RF2 with hydrogen puffing and the diamagnetic signal in the anchor cell increases. Since the RF2 frequency is adjusted to deuterium plasma, the slow waves are not excited and the ion temperature is kept low in the central cell as is seen in Fig. 10. The additional deuterium puffing is done from 40 ms. Then, the radiated power of RF2 increases abruptly and the diamagnetic signal in the central cell also increased. The density fractions of protons and deuterium ions are evaluated from the spectroscopic measurements of the Balmer lines of these two species and are found to be approximately 50 : 50. From neutron measurements, in which the yield reaches 7×10^8 neutron/s, it was estimated that the deuterium ion temperature grows to above 10 keV. This heating scheme with two ion species is just the slow wave heating. The slow wave heating will become ineffective in high-density plasmas. Advanced experiments with two ion species in mirror devices were reported in [16, 17]. Two ion hybrid heating schemes as in tokamaks or other heating scenarios must be tested in the mirror devices for higher density plasma heating in the nearest future.

5. SUMMARY

Fast Alfvén waves are efficiently used for plasma production in the GAMMA 10 tandem mirror. In the central cell, the radial and axial eigenmodes are formed and the plasma performance is affected by the strong density dependence of the excitation of these eigenmodes. The density clamping is observed when the power for the plasma production is increased. High-harmonic fast waves are introduced for the higher density plasma production. The increase above 40% in the line density is observed with no reduction of the diamagnetic signal.

The slow Alfvén waves are also efficiently used for plasma heating in the magnetic mirror configuration. An ion temperature above 10 keV is achieved, which is confirmed by the detection of fusion neutrons in experiments with a hydrogen–deuterium mixture.

ACKNOWLEDGMENTS

The authors acknowledge the GAMMA 10 group of the University of Tsukuba for their collaboration.

REFERENCES

1. G. Dimonte, A. W. Molvik, J. Barter, *et al.*, Nucl. Fusion **27**, 1959 (1987).
2. M. Ichimura, M. Inutake, S. Adachi, *et al.*, Nucl. Fusion **28**, 799 (1988).
3. S. N. Golovato, K. Brau, J. Casey, *et al.*, Phys. Fluids B **1**, 851 (1989).
4. A. I. Lysojvan, V. E. Moiseenko, O. M. Shvets, *et al.*, Nucl. Fusion **32**, 1361 (1992).
5. M. Inutake, T. Cho, M. Ichimura, *et al.*, Phys. Rev. Lett. **53**, 783 (1984).

6. S. Miyoshi, T. Cho, H. Hojo, *et al.*, Plasma Phys. Controlled Nucl. Fusion Res. **2**, 539 (1991).
7. T. Tamano, T. Cho, M. Hirata, *et al.*, Plasma Phys. Controlled Nucl. Fusion Res. **2**, 399 (1995).
8. K. Yatsu, L. G. Bruskin, T. Cho, *et al.*, Nucl. Fusion **39**, 1707 (1999).
9. T. Watari, K. Adati, T. Aoki, *et al.*, Nucl. Fusion **22**, 1359 (1982).
10. M. Inutake, M. Ichimura, Y. Kimura, *et al.*, Phys. Rev. Lett. **65**, 3397 (1990).
11. H. Hojo, M. Inutake, M. Ichimura, *et al.*, Phys. Rev. Lett. **66**, 1866 (1991).
12. M. Ichimura, T. Cho, M. Hirata, *et al.*, Phys. Plasmas **8**, 2066 (2001).
13. F. J. Paoloni, Phys. Fluids **18**, 640 (1975).
14. M. Ichimura, S. Adachi, T. Cho, *et al.*, in *Proceedings of the 16th EPS Conference on Controlled Fusion and Plasma Physics, 1987*, Vol. 1, p. 554.
15. Y. Kiwamoto, Y. Tatematsu, T. Saito, *et al.*, Phys. Plasmas **3**, 578 (1996).
16. D. R. Roberts and N. Hershkowitz, Phys. Fluids B **4**, 1475 (1992).
17. O. Sakai and Y. Yasaka, Phys. Plasmas **1**, 3896 (1994).

Plasma Physics Reports, Vol. 28, No. 9, 2002, pp. 734–749. From Fizika Plazmy, Vol. 28, No. 9, 2002, pp. 798–815.
Original English Text Copyright © 2002 by Katanuma, Tatematsu, Ishii, Saito, Ichimura, Nakashima, Yatsu.

MAGNETIC CONFINEMENT SYSTEMS

Single Minimum-*B* Ambipolar Trap[1]

I. Katanuma, Y. Tatematsu, K. Ishii, T. Saito, M. Ichimura, Y. Nakashima, and K. Yatsu

Plasma Research Center, University of Tsukuba, Tsukuba 305-8577, Japan

e-mail: katanuma@prc.tsukuba.ac.jp

Received: March 4, 2002

Abstract—A new type of ambipolar trap is proposed, where a minimum-*B* magnetic field is used to confine the particles radially and to provide plasma macroscopic stability. The particles are confined axially by creating the plug potentials at both end-mirror cells of the ambipolar trap. The plug potential is produced by only electron cyclotron resonance heating, the mechanism of which is proposed. *© 2002 MAIK "Nauka/Interperiodica".*

1. INTRODUCTION

Magnetic mirror confinement studies, in which Russian scientists have been playing an important role in improving the idea of the mirror concept, have a long history. An experiment on a minimum-*B* single mirror was firstly carried out by Ioffe [1] to prove the magnetohydrodynamic (MHD) stability.

D.A. Panov, who was a pioneer of the mirror program in Kurchatov Institute, carried out the pioneer experiments on feedback stabilization (Ogra-2 and Ogra-3 installations [2]), the first superconducting plasma installations (Ogra-3 simple mirror [3] and Ogra-4 baseball mirror [4]). Panov is well known for starting theoretical study of orthogonal magnetic configurations.

The idea of an ambipolar trap was first proposed by Dimov [5]. The ion axial confinement in the electrostatic potential hill at both ends of the ambipolar trap was theoretically studied by Pastukhov [6]. The original ambipolar trap was improved by Baldwin and Logan [7] by introducing the thermal barrier potential between the central cell and the plug region. The conventional ambipolar trap with a thermal barrier contains minimum-*B* mirror cells at both ends for MHD stability. However, such a minimum-*B* magnetic field leads to neoclassical radial transport [8, 9]. So, ambipolar traps involve many physical issues, e.g., electrostatic potential formation, plasma axial and radial transport, etc.

Ambipolar traps with a thermal barrier potential make use of the magnetically trapped high-energy ion population (sloshing ions) in the end mirror cells to create an electrostatic potential hill for ion confinement [7, 10, 11], which is called the ion confining potential or the plug potential. Subsequent experimental works, however, indicate that the plug potential can be formed without high-energy sloshing ions [12, 13]. That is, only electron cyclotron resonance heating (ECRH) applied in the plug region is responsible for the plug potential formation. The efforts aimed at understanding the mechanism for the plug potential formation without sloshing ions were first made theoretically in [14].

The ambipolar trap has greatly improved the ion axial confinement by the plug potential formation, although the formation mechanism is still unknown. So, the next issue is plasma radial transport. The GAMMA 10 ambipolar trap was designed as an axisymmetrized ambipolar trap; i.e., neoclassical radial transport is suppressed by the magnetic field configuration. However, recent experiments in GAMMA 10 revealed the existence of appreciable plasma radial transport [15, 16].

Therefore, a design of a new type of ambipolar trap is expected on the basis of the experimental results. In Section 2, we propose a new type of ambipolar trap. Section 3 presents a simple analysis of the plug potential formation. Mechanisms for the plug and thermal barrier potential formation are described in Section 4. A possible mechanism for plasma radial transport in the present ambipolar traps is presented in Section 5. A summary is given in Section 6.

2. SINGLE MINIMUM-*B* AMBIPOLAR TRAP

It is known that a magnetic surface does not exist in an open-ended magnetically confinement system such as an ambipolar trap. Instead, a magnetic flux tube, which is chosen to be circular at the central cell midplane of the ambipolar trap, has been considered as a magnetic surface without any question. The equipotential surfaces are assumed to lie just on the magnetic flux tube in the central cell. An analysis of neoclassical transport has been done of such idealized electric and magnetic configurations.

[1] This article was submitted by the authors in English.

1063-780X/02/2809-0734$22.00 © 2002 MAIK "Nauka/Interperiodica"

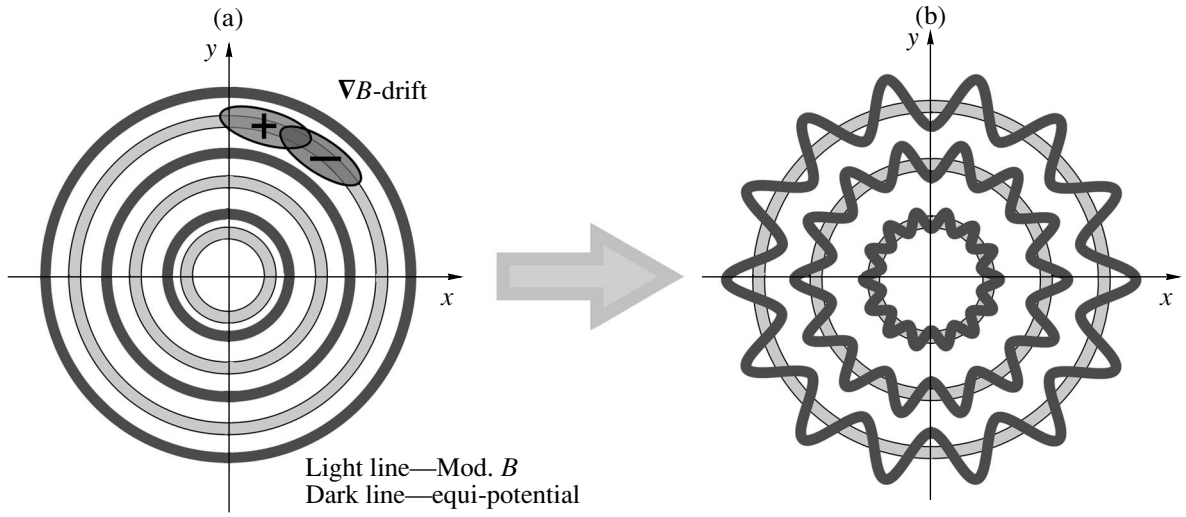

Fig. 1. Schematic diagram of $|B|$ and equipotential surfaces: (a) the circular case and (b) the case with perturbations added to the equipotential surfaces.

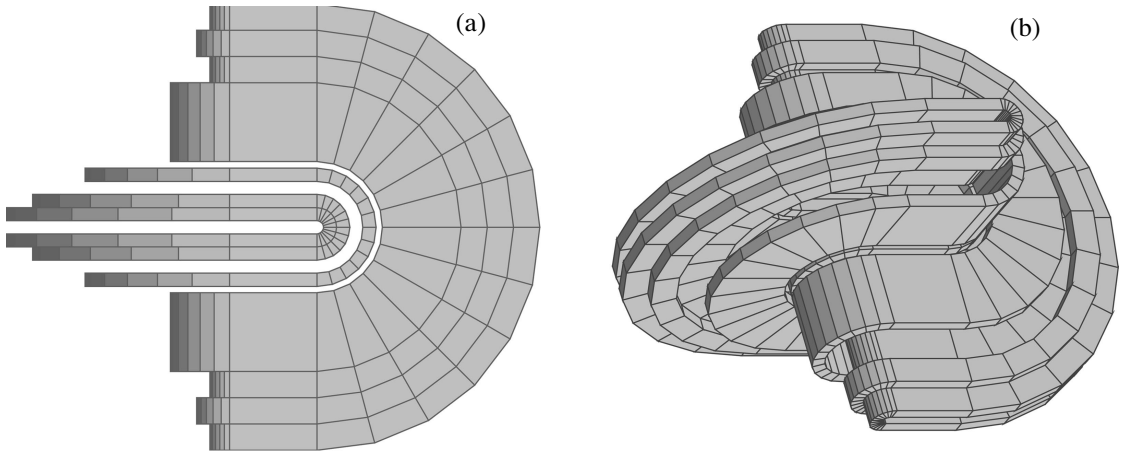

Fig. 2. Coil system of a single minimum-*B* ambipolar trap: (a) a top view and (b) a bird's eye view.

Defining the bounce frequencies ω_E and ω_B of a particle in the azimuthal direction as

$$\omega_E \equiv \frac{c|-\nabla\varphi\times\mathbf{B}|}{2\pi RB^2}, \quad \omega_B \equiv \frac{c|-\mu\nabla B\times\mathbf{B}|}{2\pi ReB^2}, \qquad (1)$$

where R is the plasma radius, e is the unit charge, c is the speed of light, B is the magnetic field, φ is the electrostatic potential, and μ is the magnetic moment, one can see that the relation $\omega_E \gg \omega_B$ is satisfied in a standard ambipolar trap such as GAMMA 10 [15, 16]. Henceforth, we use the standard notations. The plasma is produced by gas puffing and ionization and is heated by externally injected waves, so that the density and temperature fluctuations always occur in the experimental device.

Figure 1 illustrates the variations of an equipotential surface in the cross section of a single mirror cell. The unperturbed equipotential surfaces are assumed to be circular (Fig. 1a). Ions and electrons produced by ionization drift in the opposite directions through the ∇B drift. The system is usually designed to be stable against MHD modes, so that the resultant charge separation does lead to the growth of the density perturbations. However, the resultant density fluctuations will lead to the fluctuations of the equipotential surface shown in Fig. 1b.

As will be shown below, such perturbed equipotential surfaces enhance the radial drift of particles. The energy ε and the magnetic moment μ of a particle are conserved during drift motion if the Coulomb collision frequency is lower than the drift frequency. Especially for the particles with $\varepsilon \gg e\varphi$, the magnitude of the mag-

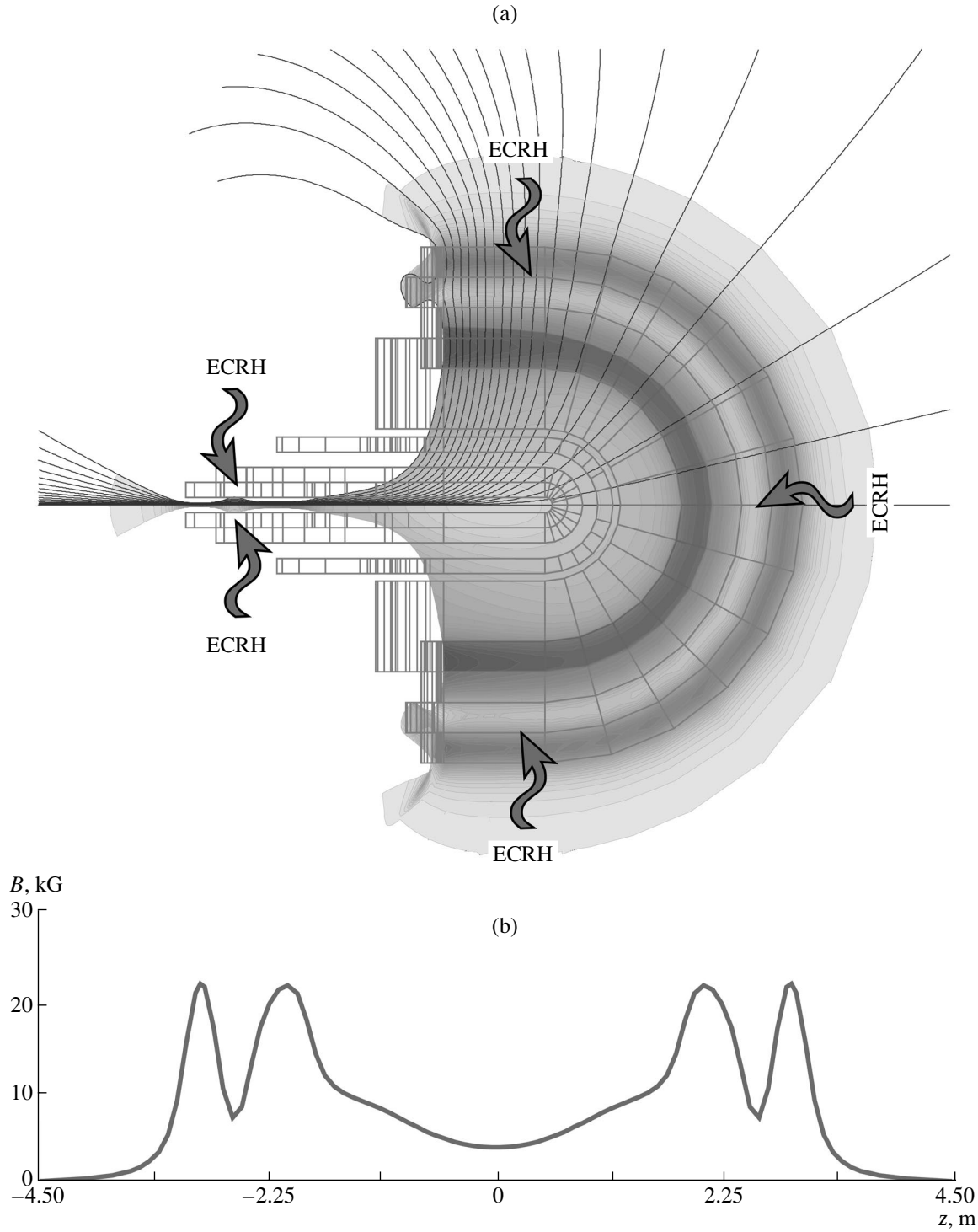

Fig. 3. (a) |B| surfaces and magnetic field lines in a single minimum-*B* ambipolar trap and (b) the axial profile of the magnetic field.

netic field B_t satisfying the relation $\varepsilon = \mu B_t$ is conserved during drift motion. Here, B_t is the magnitude of the magnetic field at the particle turning position of the axial bounce motion. That is, the particle drift motion is limited by the region $B(x, y, z) \leq B_t$. Therefore, the experimental device having closed mod-*B* surfaces can confine the particles within the magnetic well even if the electrostatic potential perturbations appear.

The single minimum-*B* ambipolar trap has a coil system shown in Fig. 2. The mod-*B* surfaces and the

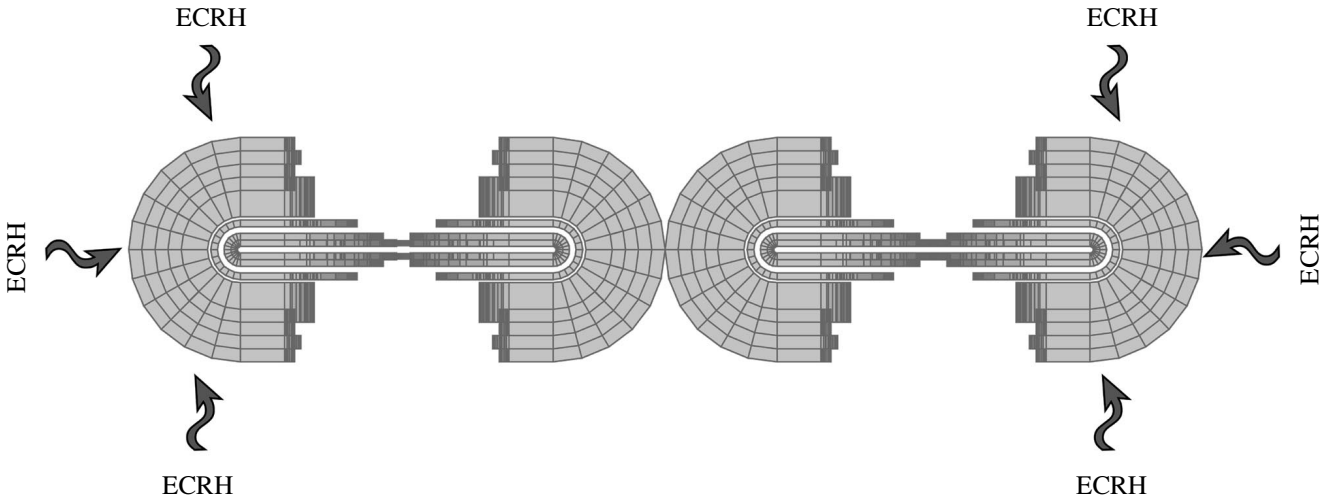

Fig. 4. Coil system of a linked minimum-*B* ambipolar trap.

axial profile of magnetic field are plotted in Fig. 3. The mirror ratio is about six, and the central cell is surrounded by baseball coils, as is seen in Figs. 2 and 3. ECRH is performed in the outermost mirror cells, which are highly elongated from the circular cross section of the magnetic flux tube, and the mod-*B* surfaces are open. Therefore, the ions and electrons trapped in the outermost mirror cells escape rapidly from there due to drift motion in the perturbed electrostatic potential, which plays the role of a thermal barrier. The plug potential is created by ECRH shown schematically in Fig. 3. The natural drift pumping of ions is expected around the thermal barrier region at the midplane in the outermost mirror cells. The linked minimum-*B* ambipolar trap is designed to increase the efficiency the power input, as is shown in Fig. 4, where ECRH is applied only in outermost single minimum-*B* mirrors. The design of the magnetic field in the transition region between single minimum-*B* mirrors is under consideration.

The mechanism for the plug potential formation is described in next section [14, 17].

3. SIMPLE ANALYSIS OF THE PLUG POTENTIAL FORMATION

The electrons coming from the central cell are reflected by the thermal barrier potential and only a small amount of the electrons reaches the plug region. On the other hand, the electrons magnetically trapped in the plug/barrier region are heated by ECRH.

The profiles of electrostatic potential and magnetic field profiles are schematically shown in Fig. 5a, and the velocity spaces of electrons and ions are shown in Figs. 5b and 5c, respectively. The electrons coming from the central cell are assumed to be Maxwellian at $z = z_i$; on the other hand, the electrons trapped in the plug/barrier region are assumed to be non-Maxwellian

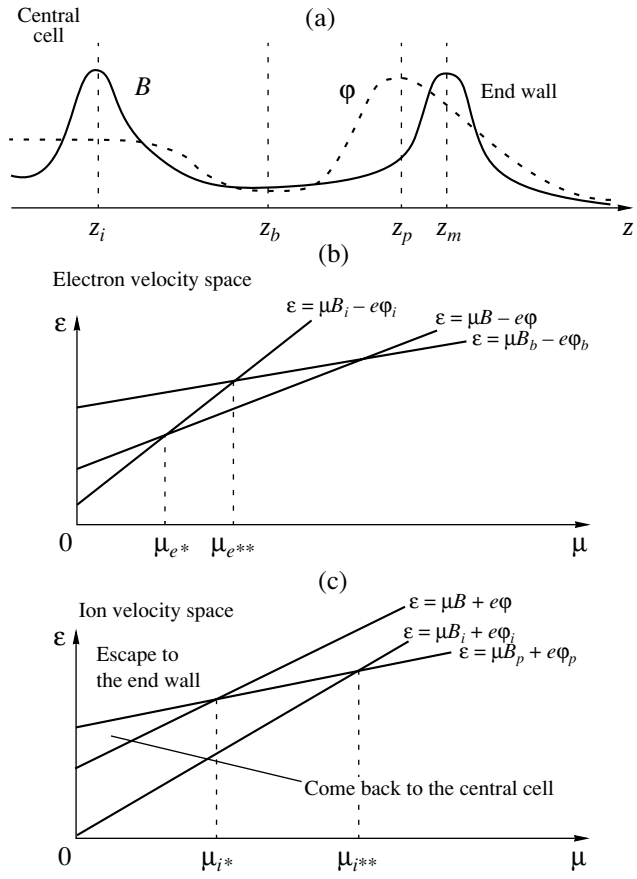

Fig. 5. (a) Axial magnetic field and electrostatic potential profiles in the plug/thermal barrier cell, (b) electron velocity space, and (c) ion velocity space.

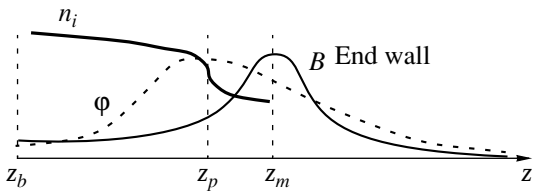

Fig. 6. Schematic diagram of the axial ion density profile around the plug.

due to radial drift (or radial loss). So, the electron distribution function is written as

$$f_e = \begin{cases} n_{ec}\left(\dfrac{m_e}{2\pi T_{ec}}\right)^{3/2}\exp\left\{-\dfrac{\varepsilon + e\varphi_i}{T_{ec}}\right\} \\ \text{for} \quad \varepsilon \geq \mu B_i - e\varphi_i \\ n_{ec}\left(\dfrac{m_e}{2\pi T_{ec}}\right)^{3/2}\exp\left\{-\dfrac{\varepsilon + e\varphi_i - \alpha_e \mu B_i}{(1-\alpha_e)T_{ec}}\right\} \\ \text{for} \quad \varepsilon < \mu B_i - e\varphi_i. \end{cases} \tag{2}$$

Here, α_e is a constant, T_{ec} and n_{ec} are the electron temperature and density at $z = z_i$, and m_e is the electron mass. Subscript i denotes the values of the quantities at $z = z_i$. The quantities ε and μ are the electron total energy ($\varepsilon \equiv \frac{1}{2} m_e v^2 - e\varphi$) and magnetic moment ($\mu \equiv \frac{1}{2} m_e v_\perp^2 / B$), where v is the velocity and $v_\perp$ is the velocity component perpendicular to the magnetic field. Distribution function (2) is the simplest one that includes the effect of non-Maxwellian electrons trapped magnetically, but it can be integrated analytically in velocity space, which is the reason why we adopt expression (2) as the electron distribution function in the end-mirror cell.

The electron density $n_e(z)$ ($z_b \leq z \leq z_m$) is given by integrating the distribution in the appropriate velocity space as

$$\begin{aligned} n_e(z) = \frac{B n_{ec}}{\sqrt{\pi} T_{ec}^{3/2}} \Bigg(& \Bigg[\int_{\mu B_b - e\varphi_b}^{\infty} d\varepsilon \int_0^{\mu_{e**}} d\mu + \int_{\mu B_i - e\varphi_i}^{\infty} d\varepsilon \int_{\mu_{e**}}^{\infty} d\mu \Bigg] \\ & \times \frac{1}{(\varepsilon - \mu B + e\varphi)^{1/2}} \exp\left\{-\frac{\varepsilon + e\varphi_i}{T_{ec}}\right\} \\ & + \int_{\mu B - e\varphi}^{\mu B_i - e\varphi_i} d\varepsilon \int_{\mu_{e*}}^{\infty} d\mu \frac{1}{(\varepsilon - \mu B + e\varphi)^{1/2}} \\ & \times \exp\left\{-\frac{\varepsilon + e\varphi_i - \alpha_e \mu B_i}{(1-\alpha_e)T_{ec}}\right\} \Bigg), \end{aligned} \tag{3}$$

where $\mu_{e*} \equiv e(\varphi - \varphi_i)/(B - B_i)$ and $\mu_{e**} \equiv e(\varphi_b - \varphi_i)/(B_b - B_i)$.

With the assumption $e(\varphi - \varphi_b)/T_{ec} \gg 1$ and $\mu_{e**} B_i / T_{ec} \gg 1$, the integrations in Eq. (3) result in [17]

$$e(\varphi - \varphi_i) \simeq (1-\alpha_e) T_{ec} \ln\left\{\frac{B - \alpha_e B_i}{B(1-\alpha_e)^{3/2}} \frac{n_e(z)}{n_{ec}}\right\}. \tag{4}$$

Here, the constant α_e should satisfy the relation $\alpha_e \leq B_b/B_i$ in order that electron distribution function (2) remain finite in the range of $B_b \leq B \leq B_i$, when $\mu \longrightarrow \infty$ with $\varepsilon = \mu B$. On the basis of thermal barrier potential φ_b, Eq. (4) reduces to

$$\begin{aligned} e(\varphi - \varphi_b) &= (1-\alpha_e) T_{ec} \ln\left\{\frac{B - \alpha_e B_i}{B(1-\alpha_e)^{3/2}} \frac{n_e(z)}{n_{ec}}\right\} \\ &\quad - (1-\alpha_e) T_{ec} \ln\left\{\frac{B_b - \alpha_e B_i}{B_b(1-\alpha_e)^{3/2}} \frac{n_{eb}}{n_{ec}}\right\} \\ &= (1-\alpha_e) T_{ec} \ln\left\{\frac{B_b[B - \alpha_e B_i]}{B(z)[B_b - \alpha_b B_i]} \frac{n_e(z)}{n_{eb}}\right\}, \end{aligned} \tag{5}$$

where $n_{eb} \equiv n_e(z_b)$.

At $z = z_b$, the distribution function of the electrons trapped in the plug/barrier mirror cell in Eq. (2) is written as

$$\begin{aligned} f_e = n_{ec}\left(\frac{m_e}{2\pi T_{ec}}\right)^{3/2} \exp\Bigg\{ & -\frac{\frac{1}{2} m_e v_\parallel^2}{(1-\alpha_e) T_{ec}} \\ & - \frac{\frac{1}{2} m_e v_\perp^2}{\frac{(1-\alpha_e)}{(1-\alpha_e B_i / B_b)} T_{ec}} + \frac{e(\varphi_b - \varphi_i)}{(1-\alpha_e) T_{ec}} \Bigg\}, \end{aligned} \tag{6}$$

which is a bi-Maxwellian distribution function with two component temperatures $T_{e\parallel}$ and $T_{e\perp}$, parallel and perpendicular to the magnetic field, respectively,

$$T_{e\parallel} = (1-\alpha_e) T_{ec}, \quad T_{e\perp} = \frac{(1-\alpha_e)}{(1-\alpha_e B_i/B_b)} T_{ec}. \tag{7}$$

Modified Boltzmann relation (5) can be derived under the assumption that the electron distribution is bi-Maxwellian distribution (6) at $z = z_b$ in the entire velocity space, including the region passing to the inner mirror throat $z = z_i$. The electrons coming from the inner mirror throat are fewer at $z = z_b$ than those magnetically trapped in the thermal barrier region if $B_i/B_b \gg 1$ and $T_e/T_{e\parallel} \gg 1$, so that the assumption that the electrons are bi-Maxwellian in the passing region at $z = z_b$ is a good

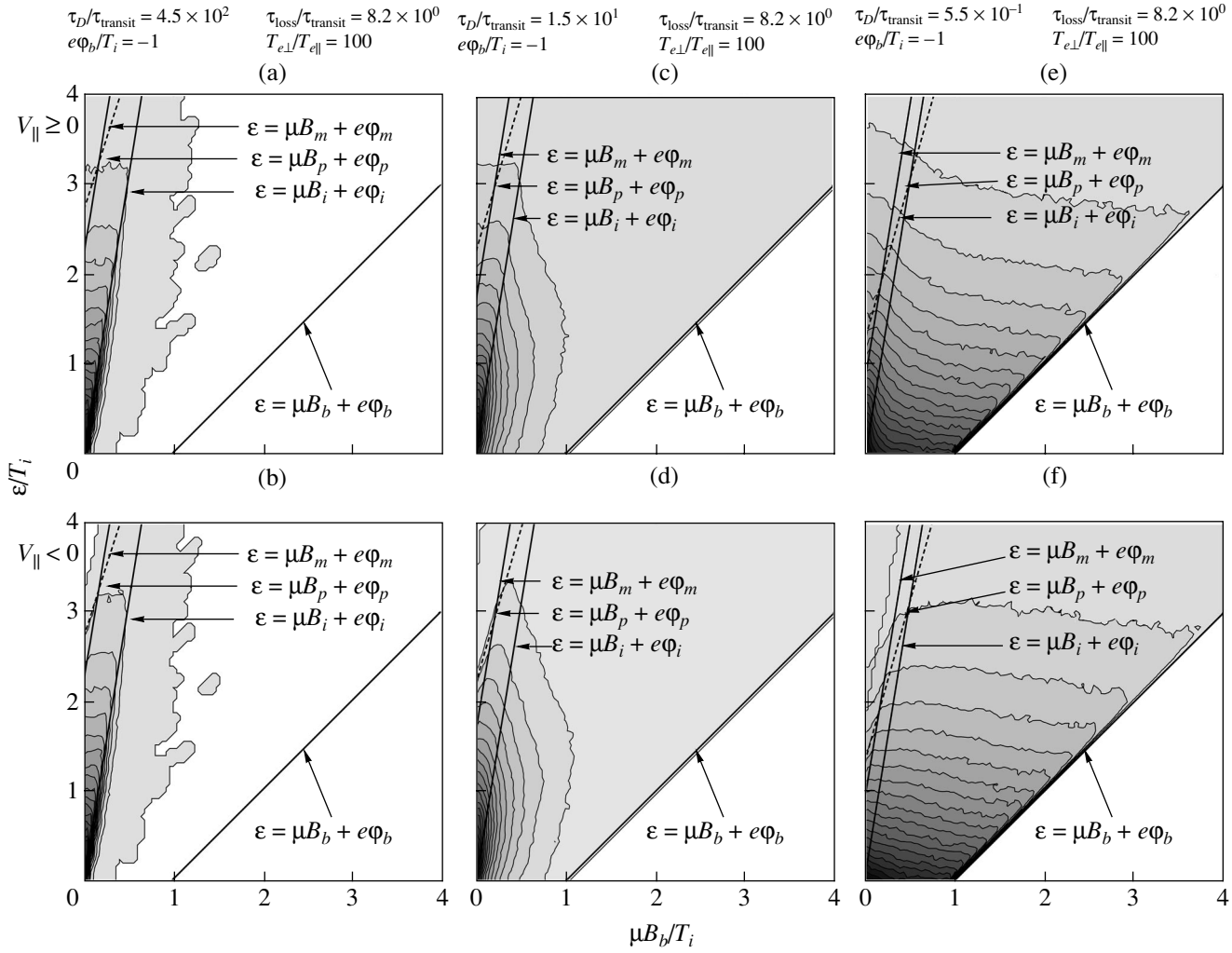

Fig. 7. Ion distribution functions: (a, c, e) the distribution functions for $v_{\parallel} \geq 0$ and (b, d, f) for $v_{\parallel} < 0$. Plots (a) and (b) are the same simulation results, plots (c) and (d) are the same parameter runs, and (e) and (f) are also the results of the same simulation runs.

approximation of the Maxwellian electrons in the passing region.

Now, we consider the mechanism for the plug potential formation briefly. As was mentioned previously in this section, modified Boltzmann law (5) has a form of $e(\varphi(z) - \varphi_b) = T_{e\parallel}\ln\{G(B)n_i(z)/n_{ec}\}$. Here, we assume the charge neutrality condition, so that the electron density n_e is equal to the ion density n_i. Since the original scenario of the plug potential formation includes the high-energy sloshing ion population, the plug potential is formed at the point where $dn_i/dz = 0$ if $G(B)$ is independent of B. In the case of a non-Maxwellian electron distribution in the plug/thermal barrier region (i.e., when $G(B)$ is a function of B), the plug potential can be formed in the region satisfying the condition $d[G(B)n_i]/dz = 0$ (if exists) in the midway from $z = z_b$ to $z = z_m$ even if there is no high-energy sloshing ion population.

In order to clear whether there exists a region where the condition $d[G(B)n_i]/dz = 0$ is satisfied, the following ion distribution function is introduced:

$$f_i = \begin{cases} n_{ic}\left(\dfrac{m_i}{2\pi T_{ic}}\right)^{3/2} \exp\left\{-\dfrac{\varepsilon - e\varphi_i}{T_{ic}}\right\} \\ \text{for} \quad \varepsilon \geq \mu B_i + e\varphi_i \\ n_{ic}\left(\dfrac{m_i}{2\pi T_{ic}}\right)^{3/2} \exp\left\{-\dfrac{\varepsilon - e\varphi_i - \alpha_i \mu B_i}{(1-\alpha_i)T_{ic}}\right\} \\ \text{for} \quad \varepsilon < \mu B_i + e\varphi_i \\ 0 \quad \text{for} \quad \begin{cases} v_{\parallel} \leq 0 \\ \text{and} \quad \varepsilon \geq \mu B_p + e\varphi_p \\ \text{and} \quad \varepsilon \geq \mu B_i + e\varphi_i. \end{cases} \end{cases} \tag{8}$$

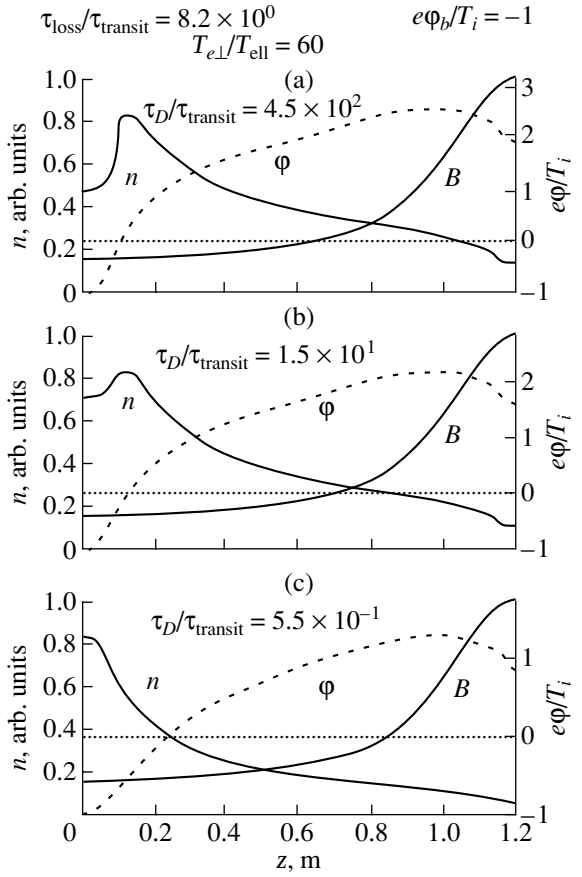

Fig. 8. Axial profiles of the electrostatic potential and ion density obtained by Monte Carlo simulations.

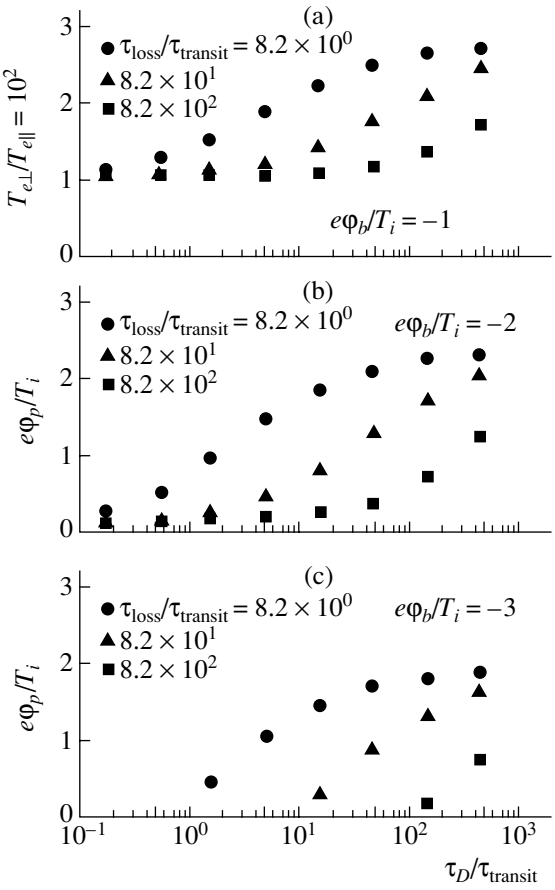

Fig. 9. Height of the plug potential as a function of τ_D.

The corresponding ion velocity space is illustrated in Fig. 5c. Here, the ion distribution function is of the same type as the electron distribution function and α_i is a constant. The ion distribution function in the loss cone in the region $v_\parallel \le 0$ is assumed to be zero; i.e., ions escaping through the outer mirror throat $z = z_m$ never come back (here, we assume $B_m = B_i$ and $\varphi_m = \varphi_i$ for simplicity). An explicit expression for the velocity $v_\parallel$ is defined in Section 4 [see Eq. (9)].

The resultant ion density profile, however, has an infinite slope at the plug as shown in Fig. 6; i.e., $dn_i/dz = -\infty$ at $z = z_p$ [17]. The infinite ion density gradient, $|dn_i/dz| = \infty$, at $z = z_p$ follows from that $|\partial f_i/\partial\varepsilon| = \infty$ on the line $\varepsilon = \mu B_p + e\varphi_p$ in Eq. (8). A type of a modified Boltzmann law $e(\varphi(z) - \varphi_b) = T_{e\parallel}\ln\{G(B)n_i(z)/n_{ec}\}$ in Eq. (4) requires $d[G(B)n_i]/dz = 0$ at the plug. However, $dn_i/dz = -\infty$ at $z = z_p$ leads to $d[G(B)n_i]/dz = -\infty$ at $\varphi = \varphi_p$ (i.e., $B = B_p$); i.e., the plug potential does not form. This contradiction is avoided by introducing the effect of Coulomb collisions, which make $|\partial f_i/\partial\varepsilon| < \infty$ on the line $\varepsilon = \mu B_p + e\varphi_p$. Coulomb collisions, therefore, are expected to form the plug potential between $z = z_b$ and $z = z_m$ because these avoid making $|dn_i/dz| < \infty$ at $z = z_p$.

4. MONTE CARLO CALCULATION OF THE PLUG POTENTIAL FORMATION

As was shown in the previous section, ion Coulomb collisions, as well as the modified Boltzmann law, are necessary to form a plug potential. In order to include Coulomb collisions in the calculations of the ion distribution function, we carry out Monte Carlo simulations.

Since the plug potential formation is a one-dimensional problem along z, we calculate the ion orbits along a magnetic field line to regard the plug potential formation as a one-dimensional problem along a magnetic field line,

$$\frac{dz}{dt} = v_\parallel, \quad v_\parallel = \sqrt{\frac{m_i}{2}(\varepsilon - \mu B - e\varphi)}. \qquad (9)$$

Ion scattering by Coulomb collisions is included by the Monte Carlo method [18–20]. The ions are input in the thermal barrier region, and, finally, the ion distribution function becomes Maxwellian due to Coulomb collisions. To describe non-Maxwellian ions in the steady state, it is necessary to introduce radial ion losses with the mean ion loss time τ_L. A uniform random number ξ_k (which is from 0 to 1) is given at each

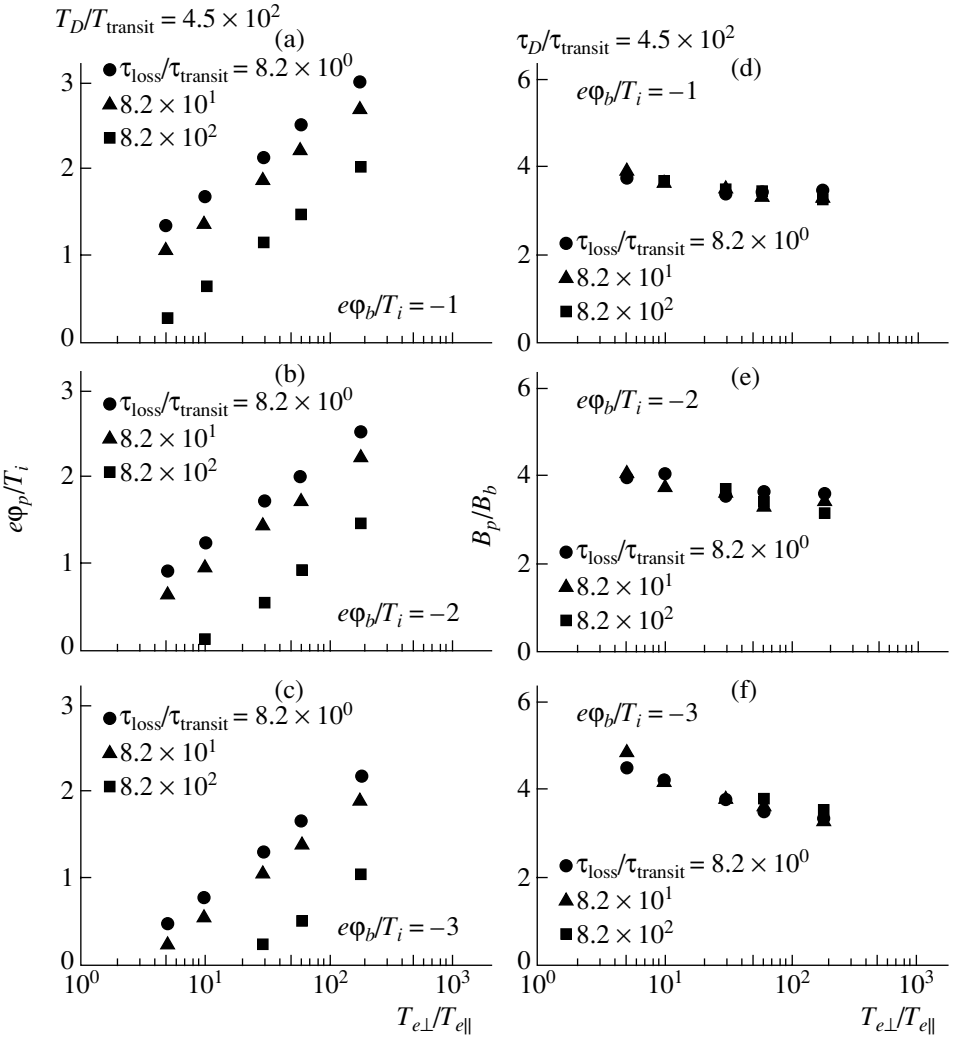

Fig. 10. Height of the plug potential and the location of the plug.

calculation step for the kth ion. The number ξ_k is compared with the magnitude of $\exp\{-t_k/\tau_L\}$, where the time t_k is measured from the time when the kth ion was input at the inner mirror throat $z = z_i$ in Fig. 5a. If $\xi_k > \exp\{-t_k/\tau_L\}$, the kth ion is lost from the plug/barrier mirror cell. Since we are looking for the steady-state plug potential, the ions that are lost are immediately input at the inner mirror throat $z = z_i$. Here, the velocity components $v_\parallel$ and $v_\perp$ of an ion at $z = z_i$ are given randomly according to a Maxwellian distribution with temperature T_{ic} in the passing region in velocity space.

The assumption of charge neutrality allows us to determine the electron density from $n_e(z) = n_i(z)$. The electrostatic potential $\varphi(z)$ is calculated by modified Boltzmann law (5). In simulations, the electrostatic potential is given in advance; i.e., $\varphi(z) = 0$. The motion of ions is followed in the given electrostatic potential, and the density is calculated from the ion positions. Ion motion is calculated until the steady-state ion density profile is established.

The new electrostatic potential is calculated by modified Boltzmann law (5) with the steady-state ion density for the old electrostatic potential profile. Then, the ion motion is traced again in the new electrostatic potential and the ion density is accumulated until a new steady-state ion density profile is established. The above procedure is repeated until the steady-state profiles of both the ion density and the electrostatic potential are established.

The parameters used in simulations are as follows. The magnetic field profile from $z = z_b$ to $z = z_m$ is adopted to be that in the end mirror cell of GAMMA 10 [12], where the axial length L_z from the thermal barrier $z = z_b$ to the outer mirror throat $z = z_m$ is $L_z = 120$ cm. The temperatures T_{field} of the field ions and electrons, with which the test ions receive Coulomb collisions, are 100 eV. The number density n_{field} of the field ions (the same as that of the field electrons) is uniform along z

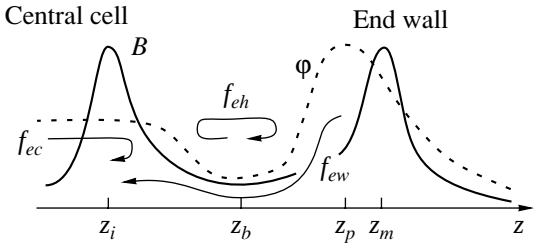

Fig. 11. Schematic diagram of electron orbits representing the electrostatically trapped warm component f_{ew}, magnetically trapped hot component f_{eh}, and low-energy components f_{ec} in the central cell.

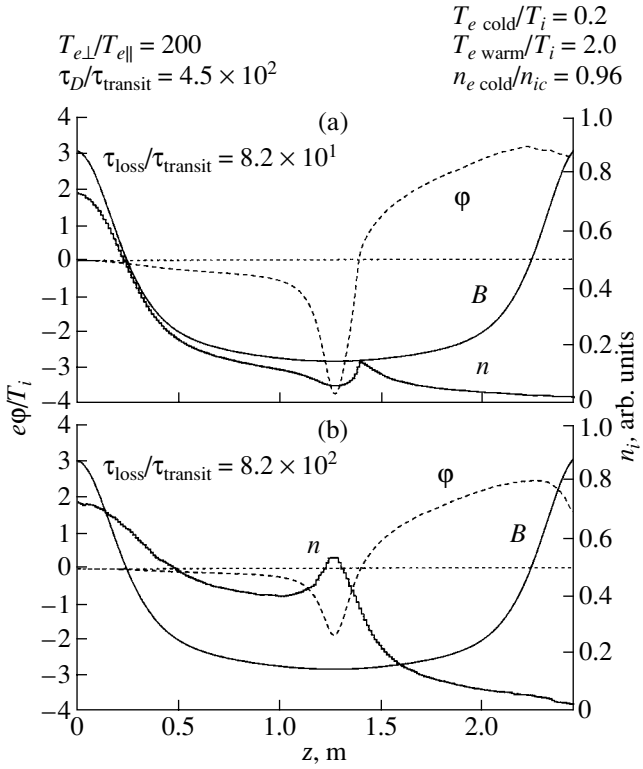

Fig. 12. Axial profiles of the electrostatic potential and ion density.

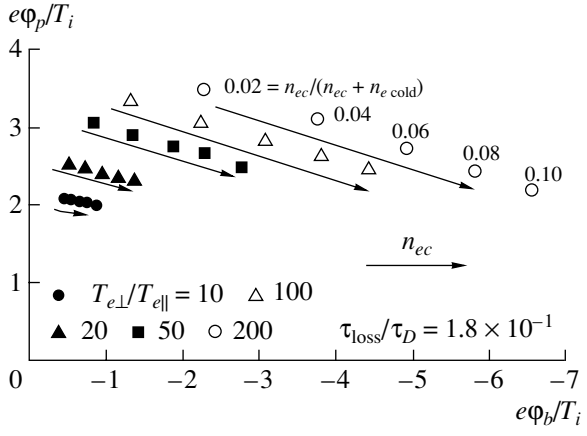

Fig. 13. Plug potential height vs. thermal barrier potential depth.

and is equal to $n_{field} = 10^{11}$ cm^{-3}. In this field plasma, the deflection time τ_D is given by

$$\tau_D = \sqrt{\frac{m_i}{2}}\frac{T_{field}^{3/2}}{\pi n_{field} e^4 \ln\Lambda_{ii}}, \quad (10)$$

where $\ln\Lambda_{ii}$ is the Coulomb logarithm. The time τ_0, defined as $\tau_0 \equiv (T_i/m_i)^{-1/2}$, is the time required for a thermal test hydrogen ion to move by 1 cm.

The temperature of test ions is set to be $T_i = 100$ eV at $z = z_i$. The deflection time is $\tau_D \simeq 5.6 \times 10^{-3}$ s, and the flight time of 1 cm is $\tau_0 \simeq 1.0 \times 10^{-7}$ s for the above parameters. The transit time $\tau_{transit}$ of an ion with $T_i = 100$ eV moving from $z = z_b$ to $z = z_m$ is defined as $\tau_{transit} = L_z \times \tau_0 = 1.2 \times 10^{-5}$ s.

In simulations, the test ions escaping from the outer mirror throat $z = z_m$ or lost (radially) are input again at the inner mirror throat $z = z_i$. The justification of the boundary condition on test ions will be given below. The ion axial density profile $n_i(z)$ is given by the test ion axial positions as

$$n_i(z) = \sum_k B(z_k)\delta(z - z_k). \quad (11)$$

Here, z_k is the axial position of the kth test ion and $\delta()$ is the Dirac delta function. The weight $B(z_k)$ in Eq. (11) comes from that the cross section of the magnetic flux tube is in inverse proportion to the magnitude of the magnetic field $B(z)$. The total number of ions N_i in the mirror cell from $z = z_b$ to $z = z_m$ in Fig. 5a is given as

$$N_i \equiv \int_{z_b}^{z_m} n_i(z)\frac{dz}{B(z)} = \int_{z_b}^{z_m}\sum_k B(z_k)\delta(z - z_k)\frac{dz}{B(z)} = \sum_k 1, \quad (12)$$

where Eq. (11) is used. Therefore, the test ions escaping from the outer mirror throat or radially are to be input immediately at the inner mirror throat in order that the total number of the ions N_i in the steady state remain unchanged. The above boundary condition on test ions means that the ions in the plug/barrier region are supplied by the ion flux from the inner mirror throat.

In order to save computer time, only the region from $z = z_b$ to $z = z_m$ is calculated. The test ions input at $z = z_i$ are mapped at $z = z_b$ with a positive velocity $v_\parallel$ on the assumption of the conservation of ε and μ during its flight from $z = z_i$ to $z = z_b$. The test ions arriving at $z = z_b$ with $v_\parallel \le 0$ are reflected perfectly at $z = z_b$ if $\varepsilon \le \mu B_i + e\varphi_i$, and are input again at $z = z_i$ with a Maxwellian velocity of T_i if $\varepsilon > \mu B_i + e\varphi_i$. The algorithm of ion supply to the end mirror cell adopted in Monte Carlo simulations is consistent with the present tandem mirror

experiment, where the ions in the end mirror cell are supplied from the central cell and escape through the outer mirror throat or escape radially.

The electrostatic potential is set to be $\varphi_i = 0$ at $z = z_i$. The potential φ_b at $z = z_b$ is given in advance and does not change throughout the simulation run. Therefore, the potential profile $\varphi(z)$ is determined from its magnitude at $z = z_b$.

Figure 7 shows the steady state ion distribution functions in the entire axial region represented by ε and μ in the case of $e\varphi_b/T_i = -1$ and $T_{e\perp}/T_{e\parallel} = 100$ for different values of $\tau_D/\tau_{transit}$, where the field ion density is changed to obtain different values of τ_D. The separatrices denoted by the lines $\varepsilon = \mu B_p + e\varphi_p$ and $\varepsilon = \mu B_m + e\varphi_m$ are determined in the simulation run, while the separatrices denoted by $\varepsilon = \mu B_i + e\varphi_i$ and $\varepsilon = \mu B_b + e\varphi_b$ are given in advance as boundary conditions for the electrostatic potential. Figures 7a and 7b, 7c and 7d, and 7e and 7f are the results of the same simulation runs, respectively. The region $\varepsilon > \mu B_p + e\varphi_p$ and $\varepsilon > \mu B_m + e\varphi_m$ is the passing region for $v_\parallel \geq 0$ in Figs. 7a, 7c, and 7e and the loss cone region for ions $v_\parallel < 0$ in Figs. 7b, 7e, and 7f. The loss time $\tau_{loss}/\tau_{transit}$ is fixed at 8.2, so that Figs. 7a and 7b are the loss dominant case and Figs. 7e and 7f are the Coulomb collision dominant case. It is seen that the loss cone region is filled with ions by Coulomb collisions in Fig. 7f, but it is almost empty in Fig. 7b. The velocity space only in the region $\varepsilon \geq 0$ is plotted in Fig. 7; i.e., the ions responsible for the plug potential formation (the energy of these ions is larger than the potential energy $e\varphi_i$ at $z = z_i$) are seen in these figures. Since the ion loss time satisfies the inequality $\tau_D/\tau_{loss} \gg 1$ in Figs. 7a and 7b, the number of test ions in the region $\varepsilon \leq \mu B_i + e\varphi_i$ is very small. However, the ion distribution function in the passing region from the inner mirror throat $\varepsilon > \mu B_i + e\varphi_i$ is almost independent of μ; i.e., it is a part of the Maxwellian distribution function, because the transit time $\tau_{transit}$ is shorter than τ_D and τ_{loss}. On the other hand, Figs. 7e and 7f correspond to the case of $\tau_D/\tau_{loss} \ll 1$, so that a significant increase in ion collisional filling is observed in the region $\varepsilon < \mu B_i + e\varphi_i$.

Figure 8 presents the axial profiles of the steady state electrostatic potential and ion density for different values of $\tau_D/\tau_{transit}$. The plug potential (note that the plug is a maximum point of the electrostatic potential) is clearly created in every case in Fig. 8. The maximum point of the ion density profile does not coincide with the position of the plug potential but rather exists in front of the plug potential, which means that almost all ions are reflected in front of the plug potential and only a small part of ions reaches the plug point. In the case of few trapped ions in the thermal barrier potential in Fig. 8a, the peak point of the ion density exists around the region where the electrostatic potential is greater than zero, i.e., the region just beyond the height of φ_i.

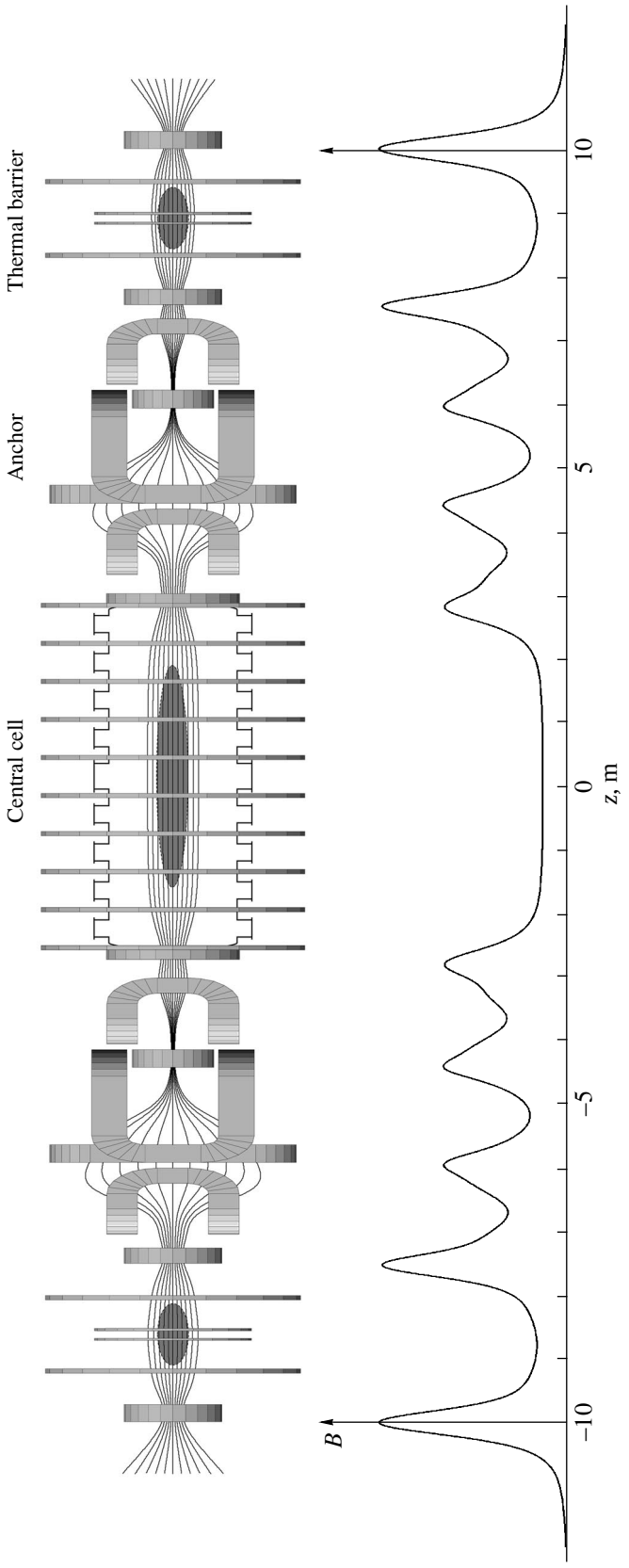

Fig. 14. GAMMA10 ambipolar trap coil system with a magnetic field line (at the top) and the axial profile of magnetic field (at the bottom).

Since the ions have the potential energy $z = z_i$ when they are input at $e\varphi_i$, the ions are reflected by the electrostatic potential predominantly when the potential is beyond φ_i. The ion density, therefore, decreases with the growth of the electrostatic potential beyond φ_i. If there exists a large amount of ions trapped in the thermal barrier potential in Fig. 8c, the peak point of the ion density profile is around $z = z_b$. The magnitude of the plug potential is plotted as a function of $\tau_D/\tau_{\text{transit}}$ in Fig. 9. In the limit of small $\tau_D/\tau_{\text{transit}}$, i.e., even in the collision dominant limit, the plug potential is found to be formed in Figs. 9a and 9b. The larger the ratio $T_{e\perp}/T_{e\parallel}$, the larger the plug potential in Figs. 10a–10c.

Figure 10 plots the height of a plug potential as a function of $T_{e\perp}/T_{e\parallel}$. Here, Fig. 10a is for $e\varphi_b/T_i = -1$, Fig. 10b is for $e\varphi_b/T_i = -2$, and Fig. 10c is for $e\varphi_b/T_i = -3$. The field ion and electron densities and temperatures determining Coulomb collisions with the test ions are the same as those mentioned previously in this section. By using relations (7), modified Boltzmann law (5) can be rewritten as

$$e(\varphi - \varphi_b) = T_{e\parallel}\ln\left\{\left[\frac{T_{e\perp}}{T_{e\parallel}} + \left(1 - \frac{T_{e\perp}}{T_{e\parallel}}\right)\frac{B_b}{B(z)}\right]\frac{n_e(z)}{n_{eb}}\right\}. \quad (13)$$

Note that the charge neutrality condition $n_i(z) = n_e(z)$ is assumed throughout this paper. The plug potential is a function of $n_e(z_p)/n_{eb}$ and B_p/B_b, as well as $T_{e\perp}/T_{e\parallel}$ in Eq. (13). Figure 10, however, indicates that the height of the plug potential is a function of only $T_{e\perp}/T_{e\parallel}$ as long as τ_D/τ_L is fixed. Figures 10d–10f show the magnetic field at the axial position of the plug potential. The position of the plug depends weakly on the ratio $T_{e\perp}/T_{e\parallel}$ and the thermal barrier depth $\varphi_b - \varphi_i$, and the position is almost independent of τ_L/τ_0, i.e., τ_L/τ_D.

Until now, the thermal barrier depth is given in advance as a boundary condition. The calculation of the entire region of the plug/thermal barrier cell including the thermal barrier region will be described below. In order to calculate the electrostatic potential from $z = z_i$ to $z = z_m$, we take into account the population of the cold component of electrons coming from the central cell, but reflected from the thermal barrier potential,

$$f_{e\,\text{cold}} = n_{e\,\text{cold}}\left(\frac{m_e}{2\pi T_{e\,\text{cold}}}\right)^{3/2}\exp\left\{-\frac{\varepsilon + e\varphi_i}{T_{e\,\text{cold}}}\right\}. \quad (14)$$

Electron distribution function (14) is the cold component denoted by the index "cold." The total electron distribution function $f_e + f_{e\,\text{cold}}$ consists of the distributions described by Eqs. (2) and (14). The two-component electron distribution function is observed in the central cell experimentally [21].

By integrating the electron distribution function $f_e + f_{e\,\text{cold}}$ over velocity space, we arrive at the modified Boltzmann law

$$\frac{e(\varphi - \varphi_i)}{T_{ec}} \simeq \frac{\left[\left(\frac{n_{e\,\text{cold}}}{n_{ec}}\right) + \left(\frac{B}{B - \alpha_e B_i}\right)\right]}{\left[\left(\frac{n_{e\,\text{cold}}}{n_{ec}}\frac{T_{ec}}{T_{e\,\text{cold}}}\right) + \left(\frac{B}{B - \alpha_e B_i}\right)\right]}\left\{1 - \frac{\left[\left(\frac{B}{B - \alpha_e B_i}\right) + \frac{3}{2}\left(\frac{n_{e\,\text{cold}}}{n_{ec}}\frac{T_{ec}}{T_{e\,\text{cold}}}\right) - \frac{1}{2}\left(\frac{n_{e\,\text{cold}}}{n_{ec}}\right)\right]\left[\frac{\alpha_e B}{B - \alpha_e B_i}\right]}{\left[\left(\frac{n_{e\,\text{cold}}}{n_{ec}}\right) + \left(\frac{B}{B - \alpha_e B_i}\right)\right]\left[\left(\frac{n_{e\,\text{cold}}}{n_{ec}}\frac{T_{ec}}{T_{e\,\text{cold}}}\right) + \left(\frac{B}{B - \alpha_e B_i}\right)\right]}\right\} \quad (15)$$

$$\times \ln\left\{\frac{n_e(z)}{n_{e\,\text{cold}} + n_{ec}\left[\frac{B}{(B - \alpha_e B_i)}(1 - \alpha_e)^{3/2}\right]}\right\}.$$

In the case of $n_{e\,\text{cold}} = 0$, Eq. (15) reduces to Eq. (4), and, in the case of $n_{ec} = 0$, Eq. (15) becomes the Boltzmann law for cold electrons, so that Eq. (15) can be regarded as an interpolation formula.

Figure 11 illustrates the typical electron orbits in the plug/thermal barrier cell. The electrons in the central cell of an ambipolar trap has a two-component distribution function in Fig. 11. Monte Carlo simulation results are plotted in Fig. 12. Here, the calculations include the region from the inner mirror throat $z = z_i$ to the outer mirror throat $z = z_m$ of the plug/thermal barrier cell. Figure 12a corresponds to the case of $\tau_{\text{loss}}/\tau_D \ll 1$, while Fig. 12b corresponds the case of $\tau_{\text{loss}}/\tau_D \gtrsim 1$. The thermal barrier potential is found to be created around $z = z_b$, and the plug potential is found at the point between $z = z_b$ and $z = z_m$ in both Figs. 12a and 12b.

Figure 13 shows the results of simulations for different parameter values. The deeper the thermal barrier potential, the higher the plug potential. The plug potential decreases with increasing ratio $n_{ec}/(n_{ec} + n_{e\,\text{cold}})$. Especially, in case of $n_{e\,\text{cold}} = 0$, the thermal barrier potential becomes too deep to form the plug potential.

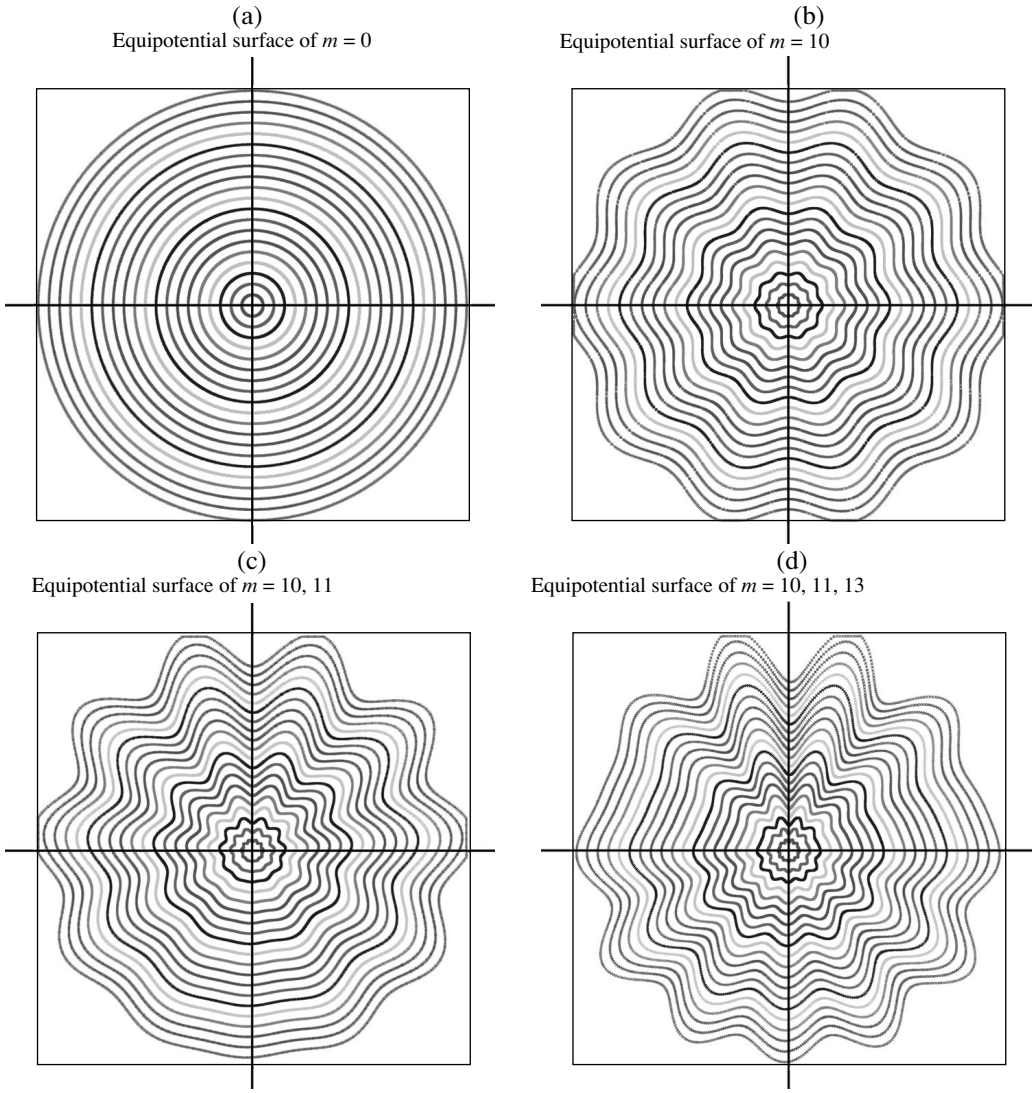

Fig. 15. Poincare map of the ions with the pitch angle $\Theta = \pi/3$ at $z = 0$.

5. RADIAL TRANSPORT DUE TO THE NONUNIFORMITY OF THE ELECTROSTATIC POTENTIAL

In calculating the plug potential formation in Section 4, the ion loss was taken into account. The larger the ion loss, the higher the plug potential. In Section 2, the natural ion radial loss was expected to create the thermal barrier potential for the plug potential formation in the outermost end mirror cells in Figs. 2 and 3.

As seen in Section 4, variations in the electrostatic potential along the magnetic field line can easily occur when the electron distribution deviates from Maxwellian. Electrons are heated by ECRH so that the temperature T_e of electrons is a function of ψ and θ, which are the coordinates across the magnetic axis. Here, we adopt the flux coordinates (ψ, θ, ζ), where the ζ coordinate is taken along the magnetic field line, $\mathbf{B} = \nabla\psi \times \nabla\theta$, and $\nabla\psi \cdot \nabla\zeta = \nabla\theta \cdot \nabla\zeta = 0$. The θ coordinate corresponds to the azimuthal coordinate and the ψ coordinate is proportional to the magnetic flux, i.e., the radial coordinate. Therefore, it is natural to assume that the electron distribution function is $f_e = f_e(\varepsilon, \mu, \psi, \theta)$.

The drift motion of ions is described by

$$\begin{aligned} \frac{d\psi}{dt} &= -c\frac{\partial\varphi}{\partial\theta} - \frac{c}{e}\kappa_\theta(2\varepsilon - \mu B - 2e\varphi), \\ \frac{d\theta}{dt} &= c\frac{\partial\varphi}{\partial\psi} + \frac{c}{e}\kappa_\psi(2\varepsilon - \mu B - 2e\varphi), \end{aligned} \tag{16}$$

where κ_ψ and κ_θ are the covariant components of the magnetic field line curvature $\boldsymbol{\kappa}$ defined by

$$\boldsymbol{\kappa} = \kappa_\psi \nabla\psi + \kappa_\theta \nabla\theta. \tag{17}$$

Here, $\boldsymbol{\kappa} \equiv \hat{e}_\parallel \cdot \nabla\hat{e}_\parallel$ and $\hat{e}_\parallel \equiv \mathbf{B}/B$.

If the electrostatic potential is a function of only ψ (i.e., $\varphi = \varphi(\psi)$), then the ions move along the surface

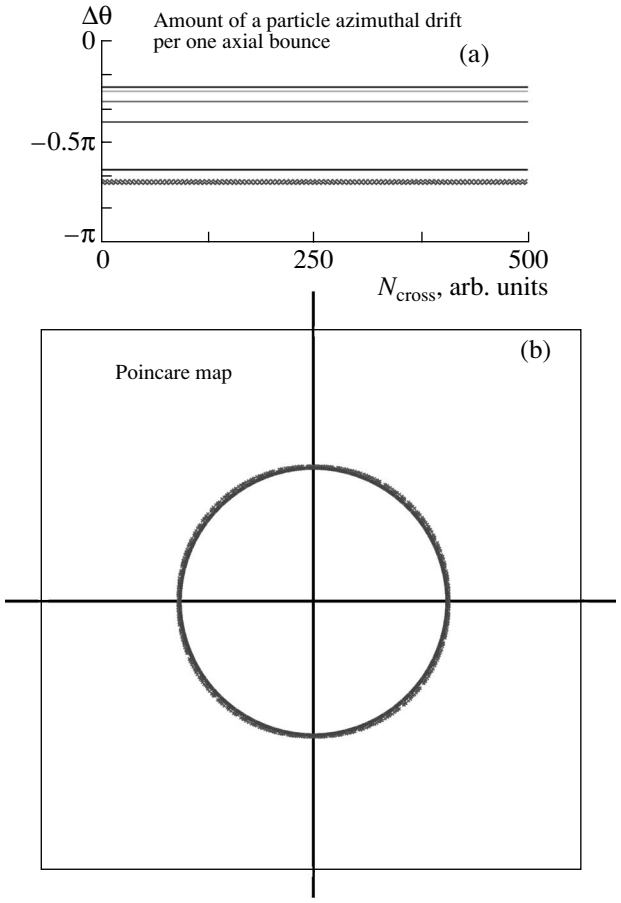

Fig. 16. Ion drift orbits with different pitch angles: (a) the amount of azimuthal drift per half axial bounce motion and (b) the Poincare map at $z = 0$. Here, N_{cross} in plot (a) is a count of particle's transits at $z = 0$.

ψ = const in the zeroth order motion and the ions drift in the first order motion across the magnetic flux tube through the ∇B drifts, which causes neoclassical radial transport. However, if $\varphi = \varphi(\psi, \theta, \zeta)$, then the ions do not move along the equipotential surfaces in the zeroth order motion in the magnetic mirrors because $\omega_E \gg \omega_B$ in Eq. (1) is satisfied in the standard cases of an ambipolar trap.

In the thermal barrier region, the electrostatic potential has a complicated axial structure, so that we consider the ions in the central region. Figure 14 shows the GAMMA 10 experimental device.

In the following calculations of ion orbits, we use the following model of the electric field:

$$\frac{e\partial\varphi}{\partial\psi} = -\frac{T_i}{\psi_0}(1 - \xi(z)\cos\{10\theta\} - \eta(z)\cos\{11\theta + 0.1\} - \zeta(z)\cos\{13\theta + 0.2\})),$$
$$\frac{e\partial\varphi}{\partial\theta} = T_i\frac{\psi}{\psi_0}(10\xi(z)10\sin\{10\theta\} + 11\eta(z)\sin\{11\theta + 0.1\} + 13\zeta(z)\sin\{13\theta + 0.2\})), \quad (18)$$

where $\psi_0 \equiv (1/2)(20\text{ cm})^2 B(z = 0)$. Ions feel the $\mathbf{E} \times \mathbf{B}$ drifts given by Eqs. (18). The ion drift surfaces are illustrated in Fig. 15, where a Poincare map is plotted at $z = 0$ by tracing the ion drift orbits in GAMMA 10. Here, an ion orbit with the pitch angle $\Theta = \pi/3$ is followed. In Eq. (18), the electric field causing $\mathbf{E} \times \mathbf{B}$ drifts is assumed to be $\xi(z) = \eta(z) = \zeta(z) = 0$ to obtain the results in Fig. 15.

The perturbations of the electric field are added to Fig. 15a in order to obtain the results in Figs. 15b–15d; i.e., the electric field with $\xi(z) = 0.1$ and $\eta(z) = \zeta(z) = 0$ is assumed in Eq. (18) to obtain the results in Fig. 15b; $\xi(z) = \eta(z) = 0.1$ and $\zeta(z) = 0$ in Fig. 15c; and $\xi(z) = \eta(z) = \zeta(z) = 0.1$ in Fig. 15d. Namely, small perturbations are added to the zeroth order $\mathbf{E} \times \mathbf{B}$ drift in Figs. 15b–15d. Therefore, Fig. 15 illustrates the equipotential surfaces at $z = 0$. The ions with the pitch angle $\Theta = n\pi/180$, where $n = 10$, 20, 30, 40, 50, 60, and 70, starting at $z = 0$, $r = 10$ cm [$\psi = 50B(z = 0)$ cm^2 G] and $\theta = \pi/4$] are traced in the electrostatic potential in Fig. 15.

Figure 16 shows the Poincare map in the electrostatic potential in the case $\xi(z) = \eta(z) = \zeta(z) = 0$, the equipotential surface of which is shown in Fig. 15a. The drift orbits with different pitch angles are circular, which is the reason why GAMMA 10 is an effectively axisymmetrized ambipolar trap. The quantity $\Delta\theta$ in Fig. 16a represents the amount of azimuthal drift per half bounce motion along a magnetic field line.

The cases in which perturbations are added to the zeroth order electric field are displayed in Fig. 17. Here, drift orbits plotted in Figs. 17a and 17b were calculated in the case of $\xi(z) = 0.1$ and $\eta(z) = \zeta(z) = 0$ as is shown in Fig. 15b; the orbits in Figs. 17c and 17d are the case of $\xi(z) = \eta(z) = 0.1$ and $\zeta(z) = 0$, the equipotential surface of which is shown in Fig. 15c; and the orbits in Figs. 17e and 17f are the case of $\xi(z) = \eta(z) = \zeta(z) = 0.1$, which is shown as the equipotential surface of Fig. 15d. It is seen in Fig. 17d that there exists a resonance particle whose orbit is shifting from the original equipotential surface and its radial position at $z = 0$ continues to approach zero in Fig. 17c. In the case of Figs. 17e and 17f, nonresonant particles are perturbed from their original equipotential surface and their orbits depend on the pitch angle.

Figures 18a and 18b correspond to the case $\xi(z) = 0.1$ (for $|z| < 200$ cm) and 0 (for $|z| \geq 200$ cm) and $\eta(z) = \zeta(z) = 0$, Figs. 18c and 18d to the case $\xi(z) = \eta(z) = 0.1$ (for $|z| < 200$ cm) and 0 (for $|z| \geq 200$ cm) and $\zeta(z) = 0$, and Figs. 18e and 18f to the case $\xi(z) = \eta(z) = \zeta(z) = 0.1$ (for $|z| < 200$ cm) and 0 (for $|z| \geq 200$ cm). Namely, Fig. 18 is the case that the electric field perturbation is localized within $|z| < 200$ cm. In these cases, the ion drift orbits are found to depend on its pitch angle greatly.

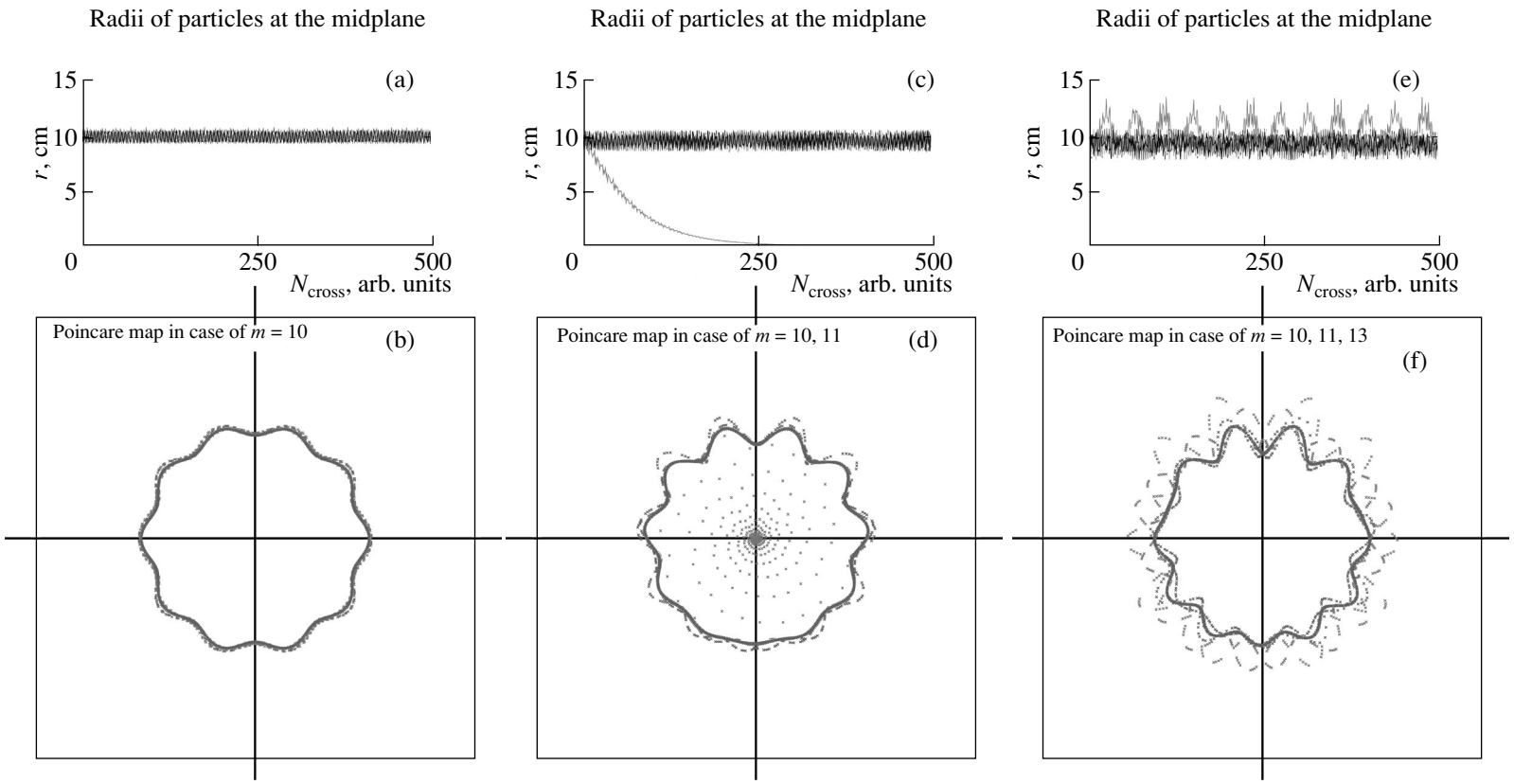

Fig. 17. Ion drift orbits: (a, c, e) the radial position of the test ions at $z = 0$ and (b, d, f) the Poincare maps of the ions at $z = 0$. Here, N_{cross} in plots (a, c, e) is a count of particle's transits at $z = 0$.

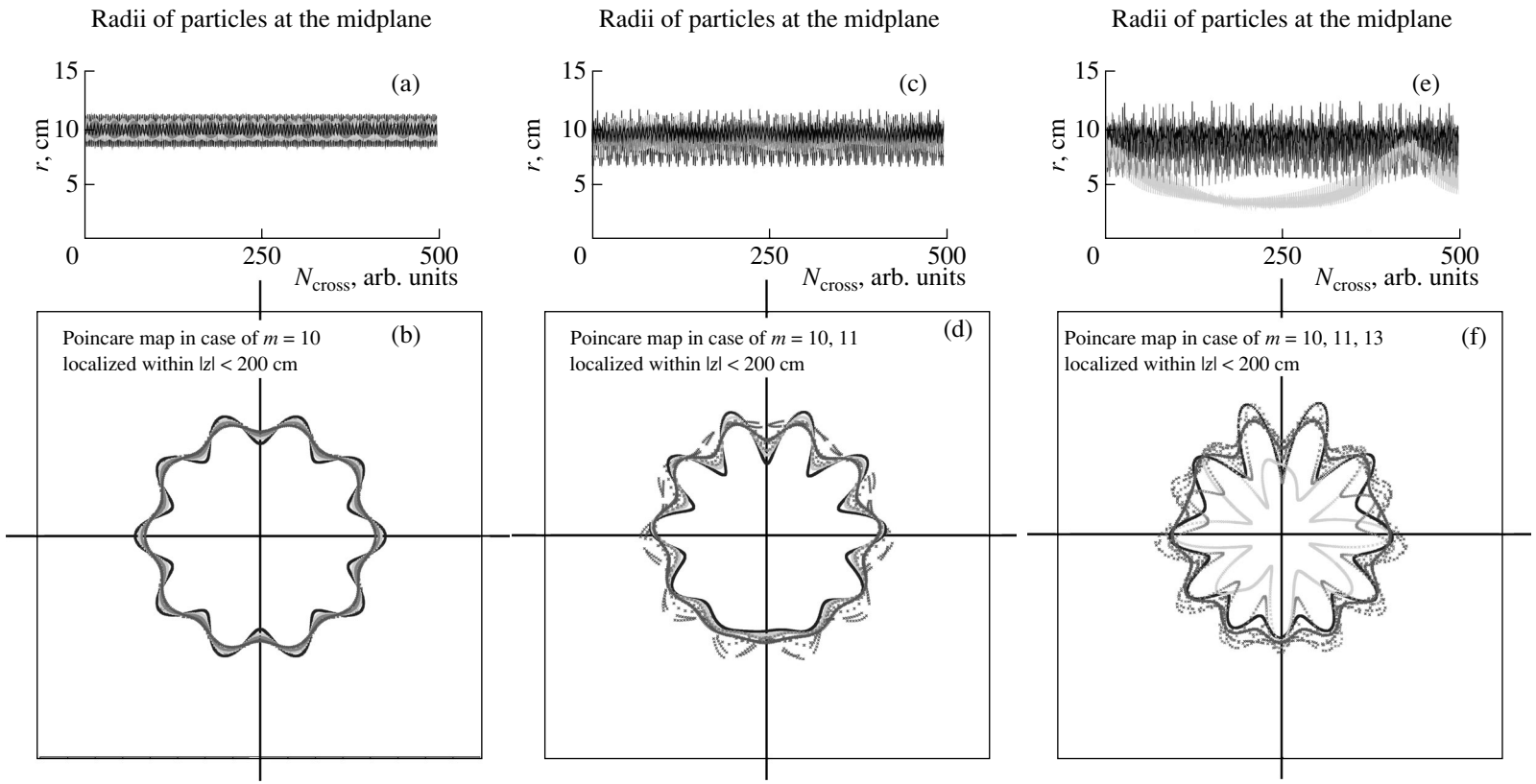

Fig. 18. Ion drift orbits: (a, c, e) the radial position of the test ions at $z = 0$ and (b, d, f) the Poincare maps of the ions at $z = 0$. Here, N_{cross} in (a, c, e) is a count of particle's transits at $z = 0$.

6. SUMMARY

We have proposed a single minimum-*B* ambipolar trap and a linked minimum-*B* ambipolar trap. The design of the transition region between each ambipolar trap is not completed yet on a linked minimum-*B* ambipolar trap. The advantage of this single minimum-*B* trap is as follows. Almost all regions consist of a minimum-*B* mirror so that the system is stable against MHD modes.

The plug and thermal barrier potentials are shown to be created if the electron distribution function is non-Maxwellian in the plug/thermal barrier mirror cells. The electron heating by externally injected microwave can easily make the electron distribution function non-Maxwellian. To maintain the non-Maxwellian electron distribution function, some (radial) loss of electrons is necessary, otherwise Coulomb collisions finally make the electrons Maxwellian.

The possible mechanism for ion (electron) radial loss has been proposed in Section 5. The character of radial loss is that the magnitude of the magnetic field at the particle axial turning point in the axial bounce motion is conserved for a particle with $\varepsilon \gg e\varphi$. Therefore, the particles trapped in the central cell of a single minimum-*B* ambipolar trap are confined within the minimum-*B* magnetic field, while the particles trapped in the end mirror cell are lost radially.

Therefore, a single minimum-*B* ambipolar trap requires only ECRH at both mirror cells for the plug/thermal barrier operation. The required pumping of particles is carried out automatically.

REFERENCES

1. Yu. B. Gott, M. S. Ioffe, and V. G. Telkovsky, in *Proceedings of the Conference on Plasma Physics and Controlled Nuclear Fusion Research, Salzburg, 1961*; Nucl. Fusion **3**, 1045 (1962).
2. V. A. Zhil'tsov, V. Kh. Likhtenshtejn, D. A. Panov, *et al.*, in *Proceedings of the 5th International Conference on Plasma Physics and Controlled Nuclear Fusion Research, Tokyo, 1974* (IAEA, Vienna, 1975), Vol. 1, p. 355.
3. V. A. Zhil'tsov, P. M. Kosarev, V. Kh. Likhtenshtejn, *et al.*, in *Proceedings of the 7th International Conference on Plasma Physics and Controlled Nuclear Fusion Research, Innsbruck, 1978*; Nucl. Fusion Suppl. **2**, 469 (1979).
4. *Proceedings of the Course on Mirror-Based and Field-Reversed Approaches to Magnetic Fusion, Varenna, Italy, 1983*, Vol. II, p. 409.
5. G. I. Dimov, V. V. Zakajdaikov, and M. E. Kishinevskij, in *Proceedings of the 6th International Conference on Plasma Physics and Controlled Nuclear Fusion Research, Berchtesgaden, 1976*; Nucl. Fusion Suppl. **3**, 177 (1977).
6. V. P. Pastukhov, Nucl. Fusion **14**, 3 (1974).
7. D. E. Baldwin and B. G. Logan, Phys. Rev. Lett. **43**, 1318 (1979).
8. D. D. Ryutov and G. V. Stupakov, Fiz. Plazmy **4**, 501 (1978) [Sov. J. Plasma Phys. **4**, 278 (1978)]; D. D. Ryutov and G. V. Stupakov, Dokl. Akad. Nauk SSSR **240**, 1086 (1978) [Sov. Phys. Dokl. **23**, 412 (1978)].
9. I. Katanuma, Y. Kiwamoto, S. Adachi, *et al.*, Nucl. Fusion **27**, 2041 (1987); I. Katanuma, Y. Kiwamoto, K. Ishii, *et al.*, Phys. Fluids B **1**, 1459 (1989).
10. T. C. Simonen, S. L. Allen, T. A. Casper, *et al.*, Phys. Rev. Lett. **50**, 1668 (1983).
11. D. P. Grubb, S. L. Allen, T. A. Casper, *et al.*, Phys. Rev. Lett. **53**, 783 (1984).
12. T. Tamano, Phys. Plasmas **2**, 2321 (1995).
13. R. S. Post, K. Brau, J. Casey, *et al.*, in *Proceedings of the 11th International Conference on Plasma Physics and Controlled Nuclear Fusion Research, Kyoto, 1986*; Nucl. Fusion Suppl. **2**, 251 (1987).
14. I. Katanuma, Y. Tatematsu, K. Ishii, *et al.*, J. Plasma Fusion Res. **77**, 1085 (2001).
15. K. Yatsu, L. G. Bruskin, T. Cho, *et al.*, Nucl. Fusion **39**, 1707 (1999).
16. K. Yatsu, T. Cho, M. Hirata, *et al.*, Nucl. Fusion **41**, 613 (2001).
17. I. Katanuma, Y. Tatematsu, K. Ishii, *et al.*, submitted to Phys. Plasmas (2001).
18. I. Katanuma, Y. Kiwamoto, M. Ichimura, *et al.*, Phys. Fluids B **2**, 994 (1990).
19. R. Minai, I. Katanuma, and T. Tamano, J. Phys. Soc. Jpn. **66**, 2051 (1997).
20. R. Minai, I. Katanuma, T. Tamano, and K. Yatsu, J. Phys. Soc. Jpn. **67**, 876 (1998).
21. T. Cho, M. Hirata, H. Hojo, *et al.*, Nucl. Fusion **41**, 1161 (2001).

Plasma Physics Reports, Vol. 28, No. 9, 2002, pp. 750–755. Translated from Fizika Plazmy, Vol. 28, No. 9, 2002, pp. 816–821.
Original Russian Text Copyright © 2002 by Akhmetov, Belkin, Bespamyatnov, Davydenko, Dimov, Kovalenko, Krivenko, Razorenov, Reva, Savkin, Shul'zhenko.

MAGNETIC CONFINEMENT SYSTEMS

Production and Study of a High-Temperature Plasma in the Central Solenoid of the AMBAL-M Device

T. D. Akhmetov, V. S. Belkin, I. O. Bespamyatnov, V. I. Davydenko, G. I. Dimov, Yu. V. Kovalenko, A. S. Krivenko, V. V. Razorenov, V. B. Reva, V. Ya. Savkin, and G. I. Shul'zhenko

Budker Institute of Nuclear Physics, Russian Academy of Sciences, Siberian Division, pr. Akademika Lavrent'eva 11, Novosibirsk, 630090 Russia

Received February 14, 2002

Abstract—Results are presented from experiments on the production and study of a hot dense plasma in the central solenoid of the AMBAL-M fully axisymmetric ambipolar magnetic confinement system. The hot plasma in the solenoid and end cell is produced by filling the system with a thermally insulated current-carrying plasma stream with developed low-frequency turbulence. The plasma stream is generated by a gas-discharge plasma source placed upstream from the magnetic mirror of the solenoid. As a result, an MHD-stabilized plasma with a length of 6 m, a diameter of 40 cm, a density of 2×10^{13} cm^{-3}, an ion energy of 250 eV, and an electron temperature of 60 eV is produced in the central solenoid. It is found that, in the quiescent decay phase, transverse plasma losses from the solenoid due to low-frequency oscillations and nonambipolar transport are rather small and comparable with the classical diffusion losses. © *2002 MAIK "Nauka/Interperiodica".*

1. INTRODUCTION

Experiments carried out in the AMBAL-M fully axisymmetric ambipolar confinement system [1] are of fundamental importance for the future fusion reactor. The key research problems here are MHD stabilization of the collisionless axisymmetric plasma and the study of longitudinal and transverse losses. Experiments in the AMBAL-M device were divided into two stages. From 1993 to 2000, experiments were conducted in the end cell, consisting of a mirror cell and semicusp. The system was filled with a turbulent plasma generated by a plasma source placed upstream from the magnetic mirror. As a result, an initial MHD-stabilized hot plasma with a density of ~2×10^{13} cm^{-3}, an electron temperature of ~60 eV, and an ion energy of ~250 eV was produced. The thermal insulation of the plasma in the entrance magnetic mirror and ohmic plasma heating in the mirror cell by the longitudinal electron current were investigated [2].

In 2000, experiments on the production and study of a hot dense plasma in a long solenoid connected to the end cell of the AMBAL-M device began. A hot plasma in the solenoid and the end cell is produced by filling the system with a thermally insulated current-carrying plasma stream with developed low-frequency turbulence. The plasma stream is generated by a gas-discharge plasma source placed upstream from the magnetic mirror of the solenoid. This source is the same as in the end cell experiments. In this paper, which is dedicated to the memory of D.A. Panov, we present the results of the first experiments on filling the solenoid with a hot dense plasma.

2. EXPERIMENTAL SETUP

Figure 1 shows a schematic of the experimental setup. The distance between the magnetic mirrors of the solenoid connected to the end cell is 7 m, and the length of the region with a uniform magnetic field of 1.95 kG is 6 m. To achieve the optimum filling of the solenoid, the distance between the solenoid entrance mirror and the plasma source can be varied from 70 to 155 cm.

The plasma parameters in the solenoid were measured with a set of diagnostics used previously in the end cell experiments [2] and consisting of movable Langmuir and magnetic probes, diamagnetic loops, end-loss energy analyzers, and a system of multichord plasma probing by the attenuation of a fast neutral beam in the solenoid.

3. EXPERIMENTAL RESULTS

The experiments showed that the filling of the solenoid with a turbulent plasma stream allowed the production of a thermally insulated plasma with a length of 6 m, a diameter of up to 40 cm, a density of up to 2×10^{13} cm^{-3}, an average ion energy of 250 eV, and an electron temperature of 60 eV. By varying the distance between the plasma source and the entrance magnetic mirror of the solenoid, it was established that both the plasma density and energy increased as the plasma source approached the solenoid. Figure 2 shows the plasma diamagnetic signals for the three positions of the plasma source: 155, 110, and 70 cm from the entrance magnetic mirror.

1063-780X/02/2809-0750$22.00 © 2002 MAIK "Nauka/Interperiodica"

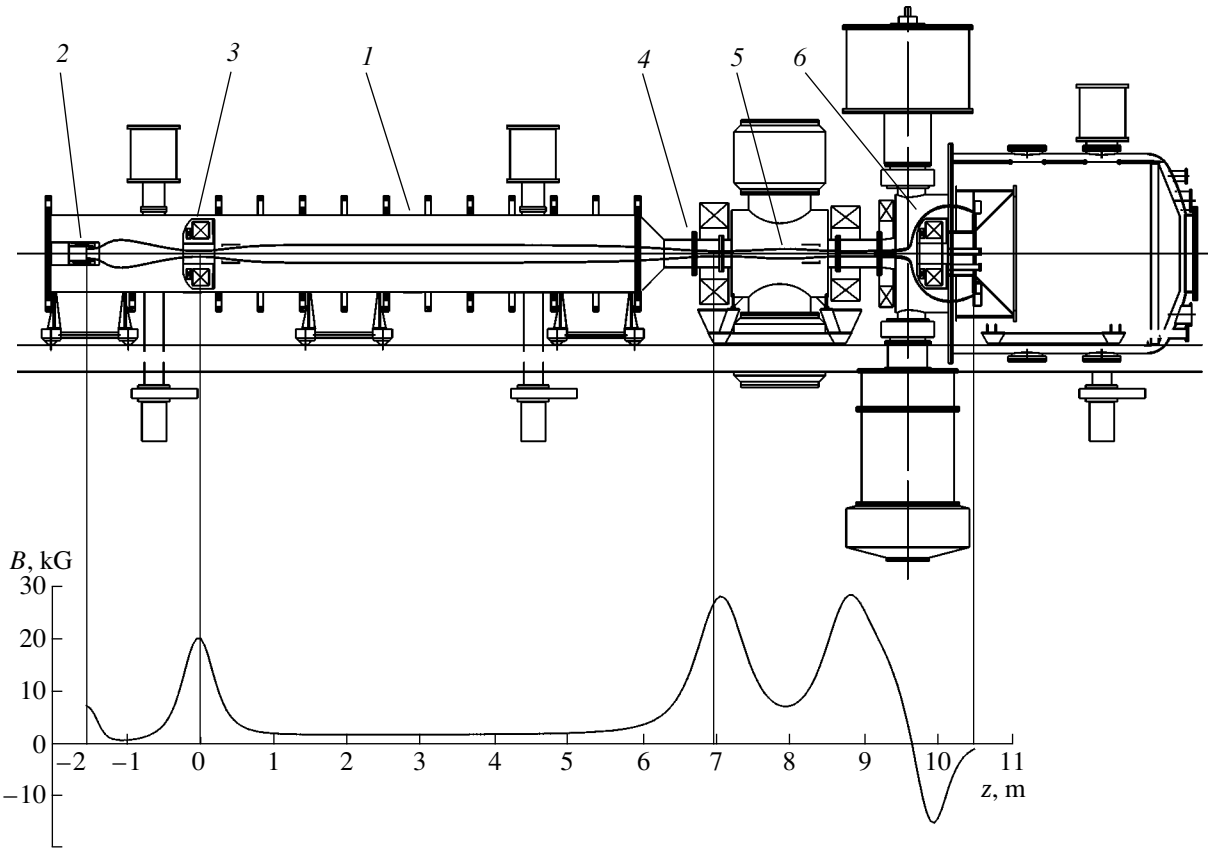

Fig. 1. Schematic layout of experiments with a central solenoid (side view): (*1*) solenoid, (*2*) gas-discharge plasma source (*3*) entrance magnetic mirror of the solenoid, (*4*) exit magnetic mirror, (*5*) mirror sell, and (*6*) semicusp. Shown are the magnetic field lines emerging from the plasma source ($z_0 = -155$ cm, $r_0 = 6$ cm). At the bottom, the axial profile of the magnetic field is shown.

Measurements with Langmuir probes showed that the internal plasma was at a fairly high negative potential. The floating potential of an isolated Langmuir probe was about –150 V for a maximum distance of 155 cm between the solenoid and the plasma source, and it was about –350 V for a minimum distance of 70 cm (Fig. 3). The rapid differential rotation of the plasma due to the substantial potential gradient leads to the onset of the Kelvin–Helmholtz instability. The spectra of the density and potential fluctuations exhibit

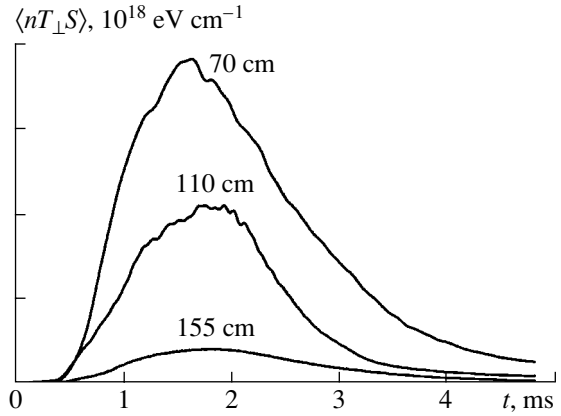

Fig. 2. Diamagnetic signals from the solenoid plasma for three distances between the plasma source and the solenoid.

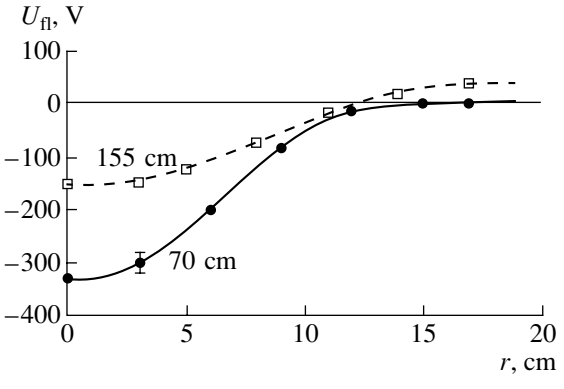

Fig. 3. Radial profiles of the probe floating potential for the maximum and minimum distances between the plasma source and the solenoid.

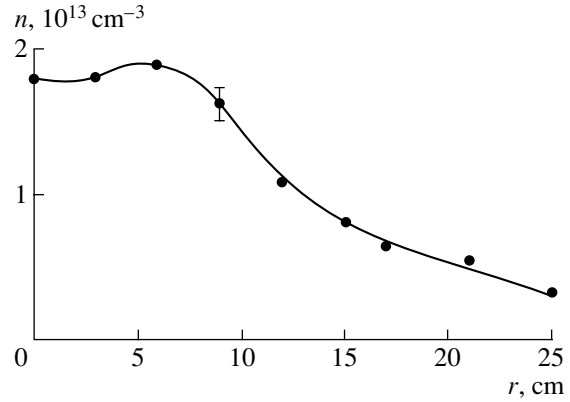

Fig. 4. Radial profile of the plasma density in the solenoid for the minimum distance between the plasma source and the solenoid.

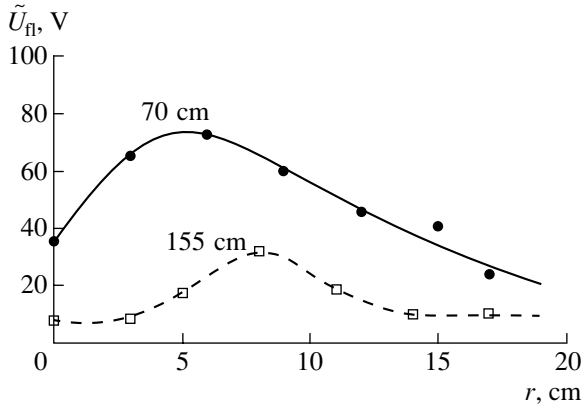

Fig. 5. Radial profiles of the rms amplitude of plasma potential fluctuations for the maximum and minimum distances between the plasma source and the solenoid.

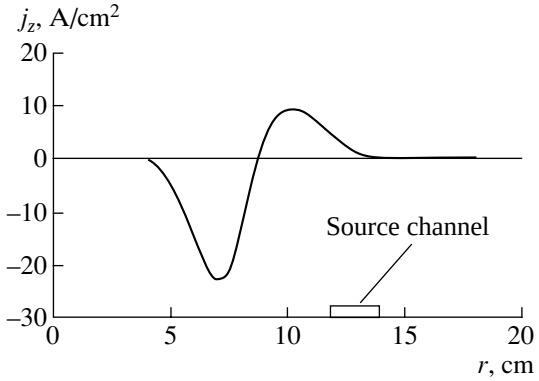

Fig. 6. Radial profile of the longitudinal current density in the solenoid.

maxima at frequencies that are multiples of the fundamental frequency $f_E = cE_r/2\pi rB \sim 15$ kHz and that are associated with the drift of the corresponding azimuthal harmonics.

The onset of electrostatic plasma oscillations leads to the intense radial diffusion of the plasma. As a result, the inner region becomes filled with a plasma that is hollow at the source outlet because of the annular geometry of the discharge channel of the source; simultaneously, a plasma appears in the peripheral region. The radial plasma density profiles obtained from probe measurements and multichord diagnostics by the attenuation of a probing fast hydrogen neutral beam (Fig. 4) have a characteristic radius of 12–18 cm at a level of $1/e$, depending on the distance between the plasma source and the solenoid. As the distance from the plasma source to the entrance mirror decreases, the transverse plasma losses increase because the amplitude of plasma potential fluctuations increases from 30 to 80 V (Fig. 5) and the outer radius of the projection of the gas-discharge channel of the source onto the solenoid increases from 12.9 to 14.2 cm. As a result, the plasma radius increases to 18 cm at a distance of 70 cm between the source and the entrance mirror.

The radial profile of the longitudinal electron current flowing through the solenoid plasma was measured with the help of a movable magnetic probe. Figure 6 shows the radial profile of the longitudinal current density in the initial segment of the solenoid (at $z = 55$ cm). It is seen in the figure that there is an inner annular region where the negative electron current with a density of ~20 A/cm^2 and total value of ~2.3 kA is directed from the plasma source to the solenoid, whereas in the outer annular region, a current of ~1.8 kA flows in the opposite direction.

We also measured the local transverse plasma transport in the central solenoid. The local transverse plasma flux caused by electrostatic oscillations is of drift nature, and its density is $\Gamma_r \approx -c\langle \tilde{E}_\varphi \tilde{n} \rangle/B$, where $\tilde{E}_\varphi$ and $\tilde{n}$ are the fluctuations of the azimuthal electric field and plasma density, respectively, and the angular brackets denote the averaging over the time interval longer than the characteristic oscillation period. This flux was measured by a combined four-electrode Langmuir probe, which could be displaced in the radial direction. The azimuthal electric field was determined from the difference between the floating potentials of one pair of probes, and the plasma density was determined from the ion saturation current. Similar probes were previously used to study fluctuations and plasma transport in the edge plasma of tokamaks (see, e.g., [3, 4]) and reversed-field pinches [5]. To eliminate the influence of the plasma source on the measurements of the radial plasma transport in the solenoid in the quiescent decay phase, the source discharge current was rapidly switched off in a time of ~0.1 ms.

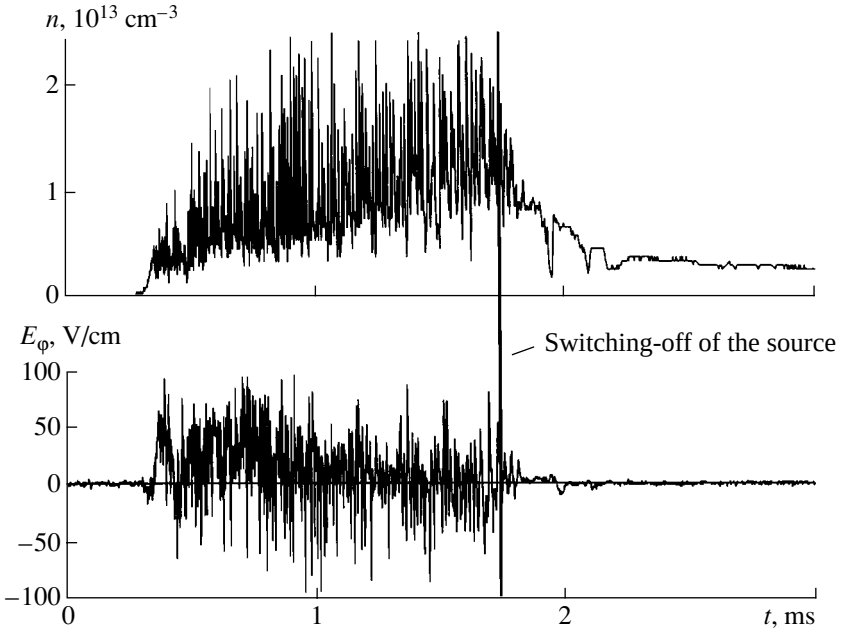

Fig. 7. Signals of the plasma density and the azimuthal electric field at a radius of 6 cm.

Figure 7 shows the signals of the ion saturation current and the azimuthal electric field. It is seen that, after the source discharge current is switched off, the amplitude of electric field oscillations sharply decreases and low-frequency fluctuations in the saturation ion current are observed over ~0.5 ms. In our opinion, these fluctuations indicate the onset of MHD plasma oscillations because of the disruption of the stabilizing effect of plasma line-tying in the conducting end after the source is switched off. Processing of the n and E_φ signals with account of the phase shift and correlation between them shows that the coefficient of turbulent diffusion in the solenoid due to low-frequency plasma fluctuations amounts to $\sim 2 \times 10^6$ cm^2/s during plasma filling. The radial plasma flux decreases by a factor of about 30 over 0.2 ms after the source current is switched off, and, over 0.7 ms, it decreases by a factor of 10^3 in comparison with the turbulent flux measured during the source operation.

Nonambipolar plasma transport in the solenoid was deduced from the measurements of the current to a plasma receiver positioned in the semicusp. When the plasma source was switched off, the current to the plasma receiver was $I_n \sim 2$ A.

An additional increase in the plasma density in the solenoid was achieved by puffing hydrogen into the axial plasma region through a ceramic tube positioned near the entrance magnetic mirror of the solenoid. At an optimum rate of hydrogen puffing into the axial region of the solenoid (~10 l torr/s), the plasma density and the amplitude of the diamagnetic signal increased by a factor of about 1.7. Consequently, the maximum plasma density in the solenoid attained a value of $\sim 4 \times 10^{13}$ cm^{-3}.

The basic parameters of the solenoid of the AMBAL-M device and the parameters of the plasma produced are listed in the table.

4. DISCUSSION

The experiments carried out in the AMBAL-M device showed that the use of a thermally insulated plasma stream is an efficient method for creating a hot plasma in the solenoid. When passing through the solenoid, the stream ions acquire the transverse energy due

Table

Parameter	Value
Distance between magnetic mirrors	7 m
Magnetic field in the uniform part	1.95 kG
Mirror ratio in the entrance and exit magnetic mirrors	10.7 and 14.7
Initial vacuum	3×10^{-6} torr
Pulse duration of the plasma source	~2 ms
Plasma diameter	~40 cm
Plasma density	$(0.3–4) \times 10^{13}$ cm^{-3}
Electron temperature	60 eV
Ion energy	250 eV
Longitudinal electron current in the plasma	~2 kA

to stochastic heating by broadband electrostatic oscillations. A fraction of ions becomes trapped in the confinement region [2]. Note that the ion cyclotron frequency in the solenoid is ~3 MHz and the ions are stochastically heated at the subharmonics of the ion gyrofrequency (in contrast to the experiments [6], in which the ion were stochastically heated at the frequencies close to the ion gyrofrequency). The plasma electrons are heated due to collisions with the trapped hot ions and due to the relaxation of the plasma electron flow with longitudinal electron energies of ~200 eV and current of ~2 kA. Transverse electrostatic plasma oscillations also enhance plasma diffusion, which leads to the broadening of the plasma density profile and an increase in transverse losses. As was mentioned above, the production of a hot initial plasma by filling the system with a turbulent plasma stream was successfully used in the previous end cell experiments in the AMBAL-M device. However, the plasma volume in the solenoid is much greater than that in the end cell; therefore, to fill the solenoid, it was necessary to increase the intensity of the plasma stream by placing the source nearer to the entrance magnetic mirror of the solenoid.

The diamagnetic and plasma density signals in the solenoid in the decay phase after the ordinary (slow) switching-off of the plasma source are quiescent, and a typical plasma decay time of ~1 ms agrees with the classical plasma confinement time, determined by the ion scattering into the loss cone. Such plasma behavior in the solenoid points to its MHD stability. Estimates of the plasma MHD stability against flute perturbations in the given magnetic field geometry show that the plasma inside the semicusp is stable if its pressure is higher than the plasma pressure in the solenoid. Experiments demonstrated that the plasma density in the semicusp was several times lower than that in the solenoid. Consequently, MHD stability of the plasma in the solenoid is provided by a different mechanism. The existence of such a stabilizing mechanism is confirmed by the fact that the behavior of the solenoid plasma remains the same after the switching-off of the semicusp coils producing the favorable curvature of the magnetic field lines. The reasonable explanation of the plasma stability observed in the experiment is that the plasma is frozen in a high-conductivity thermal plasma near the source. The density of this plasma does not change when the discharge current in the source decays slowly over a characteristic time of ~0.5 ms after the source is switched off. When the discharge current in the source is switched off abruptly over a time of ~0.1 ms, the plasma density in the solenoid decreases more rapidly than it does when the source is switched off slowly; in this case, intense density fluctuations at frequencies of 5–10 kHz are observed. These observations most likely indicate the loss of MHD stability because of the deterioration of the stabilizing effect of plasma line-tying in the source when it is switched off abruptly. To clarify this point, it is necessary to investigate plasma oscillations and transverse plasma losses in the decay phase under different source operating conditions.

The results obtained allow us to estimate the plasma lifetime in the axisymmetric solenoid. The plasma lifetime determined by transverse losses due to electrostatic oscillations in the decay phase, $\tau_\perp \sim nr/2\Gamma_r$, amounts to tens of milliseconds. The plasma lifetime determined by nonambipolar losses, $\tau_n \approx \langle nV\rangle/2I_n$, where V is the plasma volume, amounts to ~100 ms. These lifetimes are rather long (one to two orders of magnitude longer than the classical longitudinal confinement time), which indicates that the plasma can be confined in the solenoid of the ambipolar confinement system provided that the longitudinal losses are suppressed.

Controllable gas puffing for maintaining or increasing the plasma density is used in many magnetic confinement systems, in particular, open systems (e.g., the GAMMA-10 device [7]). Hydrogen puffing in the AMBAL-M device was previously used in the mirror cell of the end system and showed its high efficiency [8]. It was demonstrated that the gas puffing increases both the density and energy of the plasma. This is explained by the fact that the gas-discharge plasma source, which continues operating in the course of gas puffing, introduces a considerable power into the solenoid plasma; then, this power is transferred to the particles of the created plasma and heats them. Therefore, the ions produced by gas ionization rapidly gain energy from electrostatic oscillations via stochastic heating, whereas the electrons gain energy due to the enhanced relaxation of the longitudinal electron current in the higher density plasma.

5. CONCLUSION

A plasma with a length of 6 m, a diameter of ~40 cm, a density of 2×10^{13} cm^{-3}, an electron temperature of 60 eV, and an ion energy of ~250 eV was produced in the central solenoid of the AMBAL-M device by filling the system with a turbulent plasma stream. With an additional gas puffing, the plasma density was increased to $4 \times 10^{13-3}$, whereas the electron temperature did not decrease substantially. To further increase the plasma density in the solenoid, it is planned to use the second plasma stream, which will fill the solenoid from the opposite end. Recently, the second source has been mounted in the plasma receiver tank and the vacuum coil impeding the free propagation of the plasma stream has been removed. As a result, a transition region between the second source and the mirror cell has been formed, which is similar to the transition region between the first source and the solenoid. In this case, MHD plasma stability, as previously, is provided by the plasma line-tying in the sources at the ends of the device.

REFERENCES

1. G. I. Dimov, in *Proceedings of the International Conference on Open Plasma Confinement Systems for Fusion, Novosibirsk, Russia, 1993* (World Scientific, Singapore, 1994), p. 23.
2. T. D. Akhmetov, V. S. Belkin, E. D. Bender, *et al.*, Fiz. Plazmy **23**, 988 (1997) [Plasma Phys. Rep. **23**, 911 (1997)].
3. J. A. Boedo, D. Rudakov, R. Moyer, *et al.*, Phys. Plasmas **8**, 4826 (2001).
4. E. O. Vekshina, P. R. Goncharov, S. V. Shatalin, *et al.*, Pis'ma Zh. Tekh. Fiz. **26** (19), 52 (2000) [Tech. Phys. Lett. **26**, 873 (2000)].
5. T. D. Rempel, A. F. Almagri, S. Assadi, *et al.*, Phys. Fluids B **4**, 2136 (1992).
6. M. S. Ioffe, B. I. Kanaev, V. P. Pastukhov, and E. E. Yushmanov, Zh. Éksp. Teor. Fiz. **67**, 2145 (1974) [Sov. Phys. JETP **40**, 1064 (1975)].
7. T. Tamano, Phys. Plasmas **2**, 2321 (1995).
8. T. D. Akhmetov, S. A. Bekher, V. I. Davydenko, *et al.*, in *Proceedings of the 11th International Toki Conference on Potential and Structure in Plasmas, Toki, Japan, 2000*; J. Plasma Fusion Res. **4**, 199 (2001).

Translated by N. F. Larionova

Plasma Physics Reports, Vol. 28, No. 9, 2002, pp. 756–764. Translated from Fizika Plazmy, Vol. 28, No. 9, 2002, pp. 822–830.
Original Russian Text Copyright © 2002 by Zvonkov, Kuyanov, Nuehrenberg, Skovoroda, Zille.

MAGNETIC CONFINEMENT SYSTEMS

Toroidal Mirror System

A. V. Zvonkov*, A. Yu. Kuyanov*, J. Nuehrenberg, A. A. Skovoroda*, and R. Zille****

**Institute of Nuclear Fusion, Russian Research Centre Kurchatov Institute, pl. Kurchatova 1, Moscow, Russia*

***Max-Planck-Institut für Plasmaphysik, Greifswald, Germany*

Received December 20, 2001

This paper is dedicated to the memory of Dmitriĭ Aleksandrovich Panov

Abstract—A study is made of a toroidally linked mirror system with a zero rotational transform and a three-dimensional magnetic field that ensures good confinement of charged particles. A toroidally linked magnetic mirror configuration at low plasma pressures is calculated by numerically solving the isometry equation for the magnetic field to second order in the small parameter of the paraxial approximation. The calculations carried out with the VMEC code for a particular linked magnetic mirror configuration demonstrate the possibility of achieving good confinement of drifting particles. The calculated results show that it is, in principle, possible to link mirror cells into a toroidal configuration capable of providing plasma confinement at a tokamak level.
© 2002 MAIK "Nauka/Interperiodica".

1. INTRODUCTION

The problem of eliminating longitudinal plasma losses by linking mirror cells into a toroidal configuration has a long history, dating back to 1958, when the paper by Kadomtsev [1] was published. Various experimental and theoretical attempts have been made to devise a magnetic configuration with good confinement properties [2–4]. Unfortunately, all known proposals failed to avoid superbanana drift orbits, which are known to lead to enormously high transverse particle losses in devices with fusion plasma parameters. This is presumably one of the reasons why no experiments with such confinement systems are now carried out.

Recent advances in the study of confinement properties of magnetic configurations by analyzing the topography of the magnetic field strength on equilibrium magnetic surfaces [5–9] have made it possible to suggest a new approach to implementing the idea of toroidal mirror devices: in order to achieve good plasma confinement in a toroidal mirror system, Arsenin *et al.* [10] proposed to use the isometry condition [7].

Here, we present the results of numerical calculations of a toroidally linked vacuum magnetic mirror configuration satisfying the isometry condition [7] and analyze the confinement properties of the configuration at low plasma pressures by using the VMEC code [11]. Since this code is widely used to estimate plasma confinement in stellarators, we could follow the same computation procedure in order to carry out a comparative analysis of the confinement properties of a toroidally linked mirror system (TLMS) and an optimized stellarator. In our simulations, we did not address MHD stability issues because it is supposed that related problems will be overcome by divertor stabilization [10].

The paper is organized as follows. In Section 2, we derive equations describing a toroidally linked, vacuum paraxial isometric configuration and give an example of how they can be solved. The boundary magnetic surface obtained by solving these equations and approximated by spatial Fourier harmonics is used as input to the VMEC code for equilibrium calculations. The results of relevant simulations are described in Section 3. In Section 4, we discuss and summarize the main results of our study.

2. SECTIONALLY ISOMETRIC, TOROIDALLY LINKED MIRROR SYSTEM IN THE PARAXIAL APPROXIMATION

A TLMS with a zero rotational transform is constructed in several steps. In the first step, we apply the paraxial approximation to calculate a boundary magnetic surface whose shape satisfies the isometry condition in vacuum [7].

2.1. Paraxial Magnetic Surfaces

We consider vacuum magnetic surfaces near the magnetic axis of the system, which is a closed plane curve with variable curvature. We assume that the magnetic surfaces are symmetric with respect to the plane

1063-780X/02/2809-0756$22.00 © 2002 MAIK "Nauka/Interperiodica"

of the magnetic axis. The coordinates of the magnetic surface can be represented as

$$\begin{aligned} x &= x_{\text{axis}} - x_l \sin\alpha, \\ y &= y_{\text{axis}} + x_l \cos\alpha, \\ z &= z_l, \end{aligned} \tag{1}$$

where x_{axis} and y_{axis} are the coordinates of a current point on the magnetic axis and the coordinates x_l and z_l characterize deviation from the magnetic axis in the plane perpendicular to it. The coordinates on the magnetic axis satisfy the trigonometric equations

$$x'_{\text{axis}} = \cos\alpha, \quad y'_{\text{axis}} = \sin\alpha, \quad \alpha' = k(s), \tag{2}$$

where α is the angle between the tangent to the magnetic axis and the x-axis, k is the magnetic axis curvature, and the prime denotes the derivative with respect to the arc length s of the magnetic axis.

It is convenient to formulate the isometry condition in Boozer coordinates [12], which will be used in further analysis. We choose the radial Boozer coordinate to be the toroidal magnetic field flux Φ through the cross section of the magnetic surface and denote the poloidal and toroidal angular coordinates by θ and ζ, respectively (in a confinement system with closed magnetic field lines, the poloidal coordinate labels the field lines on the magnetic surface and the toroidal coordinate coincides with the scalar magnetic potential).

In the paraxial approximation, the deviation from the magnetic axis can be described through the expansion in the powers of $\rho = \sqrt{\Phi}$:

$$\begin{aligned} x_l &= a\rho(\cos\theta + \rho\Delta), \\ z_l &= b\rho(\sin\theta + \rho\Gamma), \end{aligned}$$

where the quantities $a(s)$ and $b(s)$ define the ellipticity of the cross section of the magnetic surface and the functions $\Delta(\theta, s)$ and $\Gamma(\theta, s)$ account for the displacement and triangularity of the magnetic surface. The longitudinal coordinate ζ is introduced through the expression

$$s = s_0(\zeta) + \rho^2\Sigma(\theta, s_0), \tag{3}$$

where the first term $s_0(\zeta)$ describes the relationship between s and ζ at the magnetic axis and the corrective second term accounts for the deviation of the surface ζ = const from the surface perpendicular to the magnetic axis. Note that it is sufficient to incorporate this correction only into the coordinates on the magnetic axis because the paraxial approximation is constructed to second order in ρ. Expanding the coordinates on the axis in powers of ρ, we obtain from representations (1) and Eq. (2) the following expressions:

$$\begin{aligned} x &= x_{\text{axis}} - x_l \sin\alpha + \rho^2\Sigma\cos\alpha, \\ y &= y_{\text{axis}} + x_l \cos\alpha + \rho^2\Sigma\sin\alpha, \\ z &= z_l. \end{aligned} \tag{4}$$

Here, there is no need to distinguish between s and s_0, so that all of the parameters of the magnetic surface in these expressions can be treated as functions either of s or ζ, through the dependence $s = s_0(\zeta)$.

The metric tensor elements in the coordinates (Φ, θ, ζ) should satisfy the conditions [10]

$$g_{13} = g_{23} = 0, \quad g_{11}g_{22} - g_{12}^2 = g_{33}/F^2,$$

where F = const is the external poloidal current (the total current in the coils). Using expressions (4), we can determine the metric tensor elements and derive the relationships for the geometric parameters of the magnetic surface. To first order, the former conditions $g_{13} = g_{23} = 0$ determine the function Σ:

$$\Sigma = -(aa'\cos^2\theta + bb'\sin^2\theta)/2.$$

The latter condition yields the relationship between s and ζ at the magnetic axis,

$$\frac{ds_0}{d\zeta} = \frac{F}{2}ab,$$

and the angular dependence of the functions Δ and Γ (with allowance for their symmetry with respect to the $z = 0$ plane),

$$\begin{aligned} \Delta &= \Delta_0 + \Delta_1\cos 2\theta, \\ \Gamma &= \Gamma_2 \sin 2\theta, \\ \Delta_0 + \Delta_1 + \Gamma_2 &= -\frac{ka}{2}. \end{aligned} \tag{5}$$

It is important to note that another restriction on the parameters Δ and Γ can be obtained from the condition $g_{13} = g_{23} = 0$ in the next-order (second-order) approximation. To do this, we must retain the higher order (third-order) terms $\rho^3\delta x$ and $\rho^3\delta y$ in expressions (4). The consistency condition for the equations for δx and δy, which follow from the conditions $g_{13} = g_{23} = 0$, gives the relationship

$$a^2(\Delta'_0 - \Delta'_1) - b^2\Gamma'_2 = kabb'. \tag{6}$$

In what follows, we will use the metric tensor element g_{33}. Taking into account the above relationships, we can

express g_{33} as

$$g_{33} = \frac{a^2b^2F^2}{4}\Big(1 - 2\rho ka\cos\theta + \frac{\rho^2}{2}[-4ka\Delta_0 + k^2a^2 - aa'' - bb'' + (-4ka\Delta_1 + k^2a^2 - aa'' + bb'')\cos 2\theta]\Big). \quad (7)$$

Let us compare the expressions derived here with the expressions obtained by Shafranov [13], who determined the shape of the magnetic surface in a mirror confinement system with closed magnetic field lines from the scalar potential of the magnetic field near the magnetic axis. The comparison yields

$$a = e^{-\eta/2}/(\pi B_0)^{1/2},$$
$$b = e^{\eta/2}/(\pi B_0)^{1/2},$$
$$\Delta_0 = A_1 + A_2 - ka/4,$$
$$\Delta_1 = A_1 - A_2 - ka/4,$$
$$\Gamma_2 = -2A_1.$$

Here, η is the ellipticity, B_0 is the magnetic field at the magnetic axis, and

$$A_1 = \int \frac{e^{-\eta/2}}{2(\pi B_0)^{1/2}}\left(\frac{k'}{8} + \frac{9}{16}k\eta' - \frac{3}{16}k\frac{B_0'}{B_0} + \frac{3B_3}{B_0}\right)ds,$$

$$A_2 = \int \frac{e^{3\eta/2}}{2(\pi B_0)^{1/2}}\left(-\frac{k'}{8} - \frac{1}{16}k\eta' - \frac{5}{16}k\frac{B_0'}{B_0} + \frac{3B_3}{B_0}\right)ds,$$

where B_3 is the amplitude of the third poloidal harmonic in the expansion of the scalar potential. One can readily verify that these expressions satisfy both conditions (5) and (6). Additionally, the terms in the expression for $\zeta(s)$, which can be obtained by inverting formula (3), are the same as the first terms in the expansion of the scalar potential of the magnetic field near the magnetic axis [13].

2.2. Isometry Condition

The isometry condition, which indicates that the B = const contours on a magnetic surface have constant separation along a field line, ensures omnigeneity, a property whereby the superbanana drift vanishes [7]. In Boozer coordinates, the isometry condition has the form

$$\frac{\partial g_{33}}{\partial\theta} = f(\rho, \theta)\frac{\partial g_{33}}{\partial\zeta},$$

where $f(\rho, \theta)$ is a bounded function periodic in θ. In this condition, we use expression (7) for g_{33} and the expansion of the function f in powers of ρ: $f(\rho, \theta) = \rho f_1(\theta) + \rho^2 f_2(\theta)$.

To first order in ρ, the choice $ka\sin\theta = \frac{F}{2}(ab)'f_1$ (where C_1 is an arbitrary constant) and the relationship $f_1 = \frac{2}{F}C_1\sin\theta$ yield the first-order isometry condition:

$$k = C_1\frac{(ab)'}{a} = -C_1\frac{B_0'}{\pi^{1/2}B_0^{3/2}}e^{\eta/2}. \quad (8)$$

Note that condition (8) coincides with the condition derived in [7].

To second order in ρ, the choice $f_2 = \frac{2}{F}C_2\sin\theta\cos\theta$ (where C_2 is an arbitrary constant) and the relationship

$$ab(4ka\Delta_1 - k^2a^2 + aa'' - bb'')\sin 2\theta = f_2Fab(ab)' - f_1F(ka^3b^2)'\cos\theta$$

yield the second-order isometry condition:

$$aa'' - bb'' = -C_1^2(a^2b^2)''/2 + (C_2 - 4C_1\Delta_1)(ab)' \quad (9)$$

Substituting isometry conditions (8) and (9) into expression (7), we can show that the following relationship is satisfied to within second-order terms:

$$g_{33}(\rho, \theta, \zeta) = g_{33}\Big(0, 0, \zeta - \rho\frac{2C_1}{F}\cos\theta - \rho^2\frac{C_2}{F}\cos^2\theta\Big) - \rho^2a^2b^2(2C_1(ab)'(\Delta_0 - \Delta_1) + bb'').$$

The metric tensor element g_{33} is uniquely related to the magnetic field strength B: $B = F/2\pi\sqrt{g_{33}}$. Consequently, the isomagnetic contours B = const on the magnetic surface ρ = const are the lines ζ = const + $\rho\frac{2C_1}{F}\cos\theta + \rho^2\frac{C_2}{F}\cos^2\theta$. In the (θ, ζ) plane, all of the isomagnetic contours can be obtained by translating a fixed contour along the ζ-axis.

In a mirror confinement system with closed magnetic field lines, equilibrium magnetic surfaces are determined by the condition $\oint dl/B = U(\rho)$ (see, e.g., [14]). The magnetic surfaces on which the isometry condition is satisfied are equilibrium surfaces [7]. This is also readily seen from the familiar equilibrium conditions in the paraxial approximation [13]; in our notation, they can be written as

$$\oint ka^2b\,ds = 0,$$
$$\oint(bb'' - aa'' + k^2a^2 - 4ka\Delta_1)ab\,ds = 0.$$

Taking into account isometry conditions (8) and (9), we see that these equilibrium conditions are satisfied, because the integrands are the total derivatives of periodic functions.

2.3. Sectionally Isometric Mirror System

In order to construct a TLMS, it is necessary to ensure that the magnetic field lines are closed. A possible way to do this is to require that the condition for closed field line geometry be satisfied only in the paraxial approximation. In other words, to second order in ρ, it is sufficient to require that the magnetic axis be closed and the differential equation (6) for the *periodic* functions $a, b, k, \Delta_0, \Delta_1$, and Γ_2 be satisfied. However, we will take a different approach.

The mirror-image symmetry of a magnetic configuration, i.e., the symmetry of a magnetic surface with respect to a certain plane perpendicular to the magnetic axis (e.g., the $y = 0$ plane), guarantees that the magnetic field lines are closed [15] and requires that the functions B_0, η, and k be even functions of s (provided that the arc length of the magnetic axis is measured from the mirror-image symmetry plane).

Unfortunately, this requirement contradicts the first-order isometry condition (8). Let us try to make them as consistent as possible. This can be done in the following way. We consider a TLMS that has several periods, i.e., is composed of several identical curvilinear subsystems. We assume that each subsystem consists of two symmetric parts such that the constant C_1 is positive in the first half and is negative ($-C_1$) in the second half. We also assume that the constant changes sign at the magnetic field maxima $B_{0\max}$, at which $B_0' = 0$. Under these assumptions, from Eq. (8), we see that the curvature is a continuous function and, in Eq. (9), we can set $\Delta_1 = 0$ for simplicity, in which case Eq. (9) becomes independent of the sign of C_1.

Of course, a TLMS constructed in this way is not exactly isometric. This can be seen, e.g., from the expression for the contours of constant magnetic field strength B on an equilibrium magnetic surface (see the end of Section 2.2). It can nevertheless be hoped that the deviation from isometry will be small. At least, the most dangerous particles (those that are most deeply trapped in local magnetic wells) will move in an essentially isometric field and thus will not lead to superbanana losses. In addition, a break in the curvature indicates that the solution obtained is actually nonanalytic in the third and higher orders in the paraxial approximation. However, in our simulations, this circumstance did not cause any confusion, because the paraxial approximation is used merely to determine the magnetic surface, the coordinates on which are expanded in a series in poloidal and toroidal harmonics. However, since these expansions are analytic functions, we could naturally use them as the boundary conditions in the VMEC code.

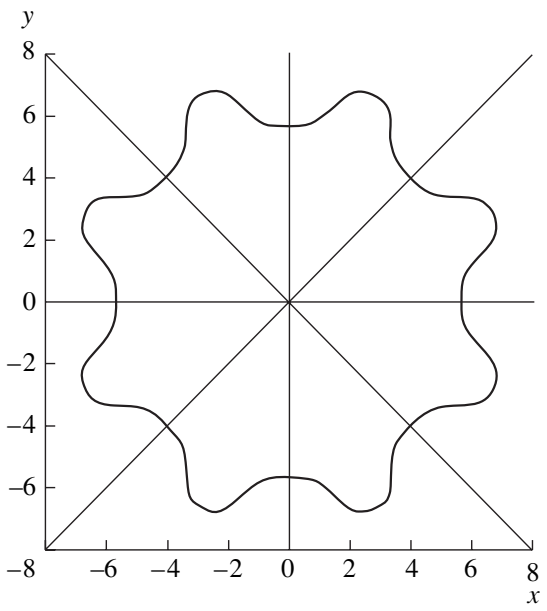

Fig. 1. Magnetic axis of an 8-period toroidally linked mirror system.

Hence, in order to construct a sectionally isometric TLMS, we solved Eqs. (2) and (8) (in which we took into account the above change of the sign of C_1) and Eq. (9) (in which we set $\Delta_1 = C_2 = 0$). The functions Δ_0 and Γ_2 were calculated from the relationships

$$\Delta_0 = -\frac{ka}{2}\frac{b^2}{a^2+b^2} - I,$$

$$\Gamma_2 = -\frac{ka}{2}\frac{a^2}{a^2+b^2} + I,$$

$$I' = ka\left[\frac{ab}{(a^2+b^2)^2}(a'b - ab') - \frac{bb'}{a^2+b^2}\right],$$

which satisfy Eqs. (5) and (6). As may be seen, there remains considerable freedom in searching for the solution, because there is one equation, namely, Eq. (9), for two unknown function, a and b.

For convenience in numerical solution, we represented the functions a and b as $a = \frac{1}{\sqrt{\pi B_{0\max}}}\exp(u+v)$, $b = \frac{1}{\sqrt{\pi B_{0\max}}}\exp(u-v)$. The magnetic field at the axis, $B_0 = B_{0\max}\exp(-2u)$, was determined in terms of a periodic function u, which was specified as the sum of several harmonics, $u = D_2(\cos 2s - 1) + D_4(\cos 4s - 1) + D_3(\cos 3s - \cos s) + D_5(\cos 5s - \cos s)$, over one period of the system. The arc length s of the magnetic axis over one period was nondimensionalized in such a way that

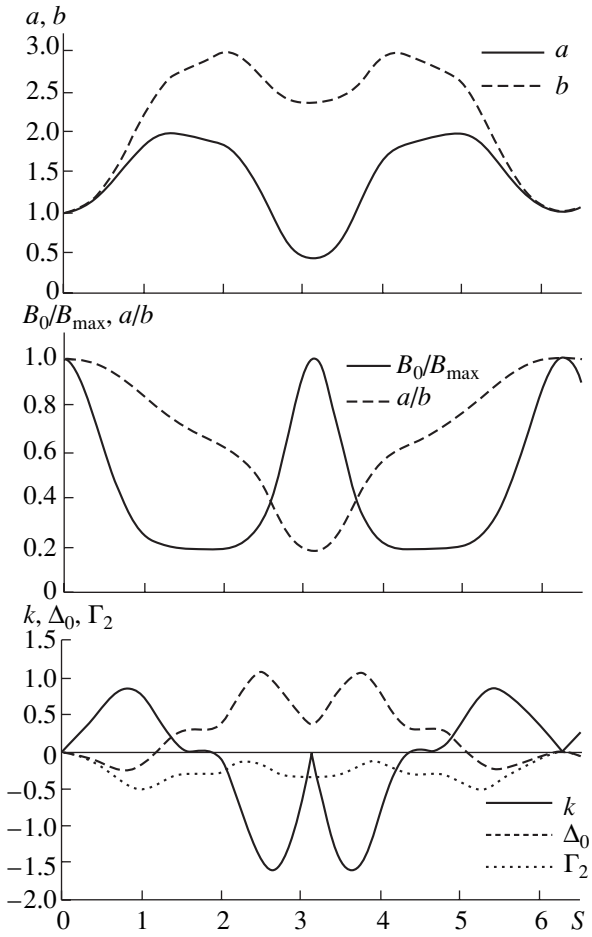

Fig. 2. Calculated dependences of a, b, B_0, a/b, k, Δ_0, and Γ_2 on the coordinate along the magnetic axis.

the function u was 2π-periodic. At the points $s = 0$, π, and 2π, at which $u = u' = 0$, the magnetic field has maxima. Equations (2) and (9) for the unknown function v were solved with the initial conditions $v = v' = 0$ at $s = 0$ (which corresponds to circular magnetic surfaces). By varying the constants D and C_1, we were able to obtain a periodic solution and to close the magnetic axis.

Figure 1 shows the shape of the magnetic axis in an 8-period TLMS with $C_1/\sqrt{\pi B_{0\,\max}} = 0.257592$, $D_2 = -0.420341$, $D_3 = 3.86782 \times 10^{-2}$, $D_4 = -0.949148 \times 10^{-1}$, and $D_5 = 3.46073 \times 10^{-2}$. We can see that the angular separation between the mirror-image symmetry planes is 22.5°. Figure 2 illustrates how functions a and b, the magnetic field strength at the magnetic axis, the ratio of semiaxes a/b, the magnetic axis curvature, and the displacement and triangularity of the magnetic surface (the last three functions being normalized to $\sqrt{\pi B_{0\,\max}}$) depend on the arc length over one period of the system.

3. CALCULATIONS OF THE MAGNETIC CONFIGURATION AND PARTICLE CONFINEMENT WITH THE VMEC CODE

Having calculated functions a, b, k, Δ_0, and Γ_2, we can use expressions (4) as a parametric representation of the boundary magnetic surface of a configuration one of the eight periods of which is shown in Fig. 3. On the boundary magnetic surface, we plot the magnetic field lines and the isomagnetic contours B = const in vacuum. The lines and the contours are all seen to enclose the magnetic axis.

Then, we expand the cylindrical coordinates R and z on the boundary magnetic surface in Fourier series: $R = \sum_{m=0}^{M}\sum_{n=-N}^{N} R_{mn}\cos(m\theta - n\varphi)$, and $z = \sum_{m=0}^{M}\sum_{n=-N}^{N} z_{mn}\sin(m\theta - n\varphi)$, where R is the distance from the z, φ is the toroidal angle, and θ is the Boozer angular coordinate in the paraxial approximation (see Section 2). The resulting sets of coefficients R_{mn} and z_{mn} can be used as input to the VMEC code. In order for the code to calculate a sufficiently smooth boundary magnetic surface over one period of the system, it was necessary to use a large number of Fourier harmonics ($M = 7$, $N = 30$).

Figure 4 shows isomagnetic contours calculated for $\beta = 0.1\%$ in the plane (θ, ζ) of Boozer coordinates on a magnetic surface with a radius equal to 0.9 of the plasma radius. We can see that, in a TLMS, isomagnetic contours are symmetric with respect to the vertical line at which the magnetic field is maximum (in the middle of the period). With sufficient accuracy, isomagnetic contours in each half-period possess the translational symmetry in the toroidal direction.

Figure 5 shows the contours of $\oint dl/B$ = const calculated at $\beta = 0.1\%$ in Boozer polar coordinates (ρ, θ) in an arbitrary cross section of the magnetic surface. In these coordinates, the magnetic surfaces are concentric circles. The contours of $\oint dl/B$ = const are also seen to be nested circles. It may therefore be concluded that we have actually arrived at equilibrium magnetic surfaces in a magnetic mirror configuration with closed magnetic field lines.

Figure 6 shows the contours $J_\parallel = \oint \mathbf{v}\,d\mathbf{l}$ = const of the longitudinal adiabatic invariant calculated at $\beta = 0.1\%$ for different pitch angles of the trapped particles (i.e., for different mirror ratios $B_{\mathrm{ref}}/B_{\min}$, where B_{ref} is the magnetic field strength at the reflection point). We can immediately see the omnigeneity of most of the trapped particles: the contours $J_\parallel$ = const coincide with the equilibrium magnetic surfaces (the concentric circles in Fig. 5). This provides clear evidence for good confinement of the trapped particles, which constitute the majority of the particles in a TLMS.

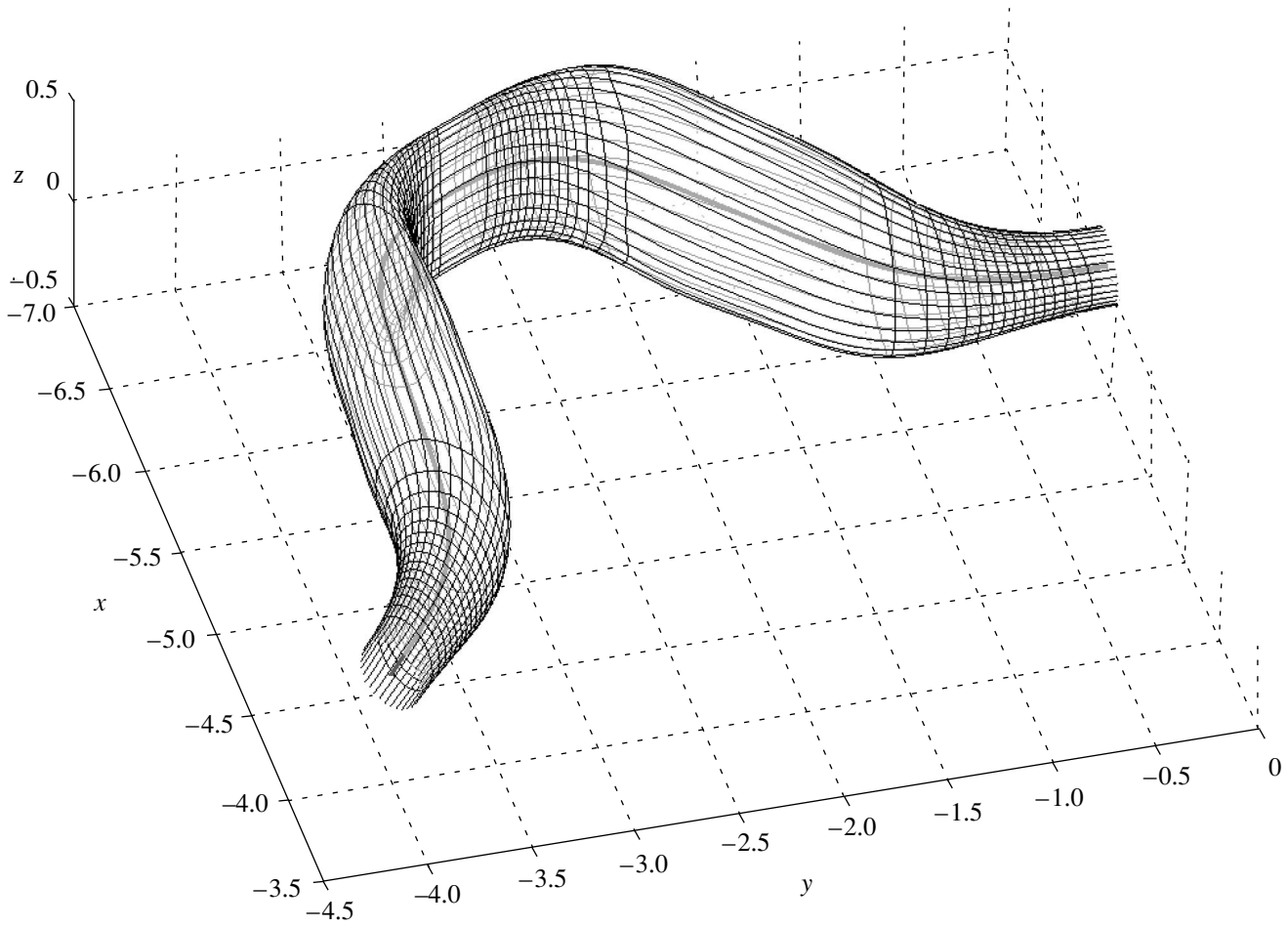

Fig. 3. Boundary magnetic surface over one period of a toroidally linked mirror system.

3.1. Particle Confinement

In the VMEC code, the particle confinement quality is controlled by the following universal procedure. The reactor-scale sizes and relevant magnetic fields are automatically assigned to the mirror system. The drift trajectories of model 3.6-MeV α-particles that start with random velocities from random positions at a given magnetic surface are traced until the particles escape from the interior of the boundary magnetic surface. The times at which the particles escape through the boundary magnetic surface and the total number of such particles are stored in the code. The table presents the parameters of the TLMS that were used in simulations, and Fig. 7 illustrates the dynamics of the losses of particles starting from three magnetic surfaces. Figure 7 shows that there is good particle confinement in a TLMS with a large mirror ratio. Note that fairly rapid losses of a small number of particles starting from magnetic surfaces with large radii is presumably associated with the fact that the isometry condition at these surfaces is satisfied somewhat inexactly, which gives rise to small "isomagnetic islands" near the extremes of the magnetic field (Fig. 4). The calculated results are found to agree fairly well with the results obtained in analogous simulations of optimized stellarators [16].

Parameters of a toroidally linked mirror system

Aspect ratio	20.65
Plasma volume	469.5 m^3
Major radius (min/max)	18.63 m/24.78 m
Volume-averaged minor radius	1.114 m
Average magnetic field	5 T
Mirror ratio at the magnetic axis	5.8
Average β value	0.1%

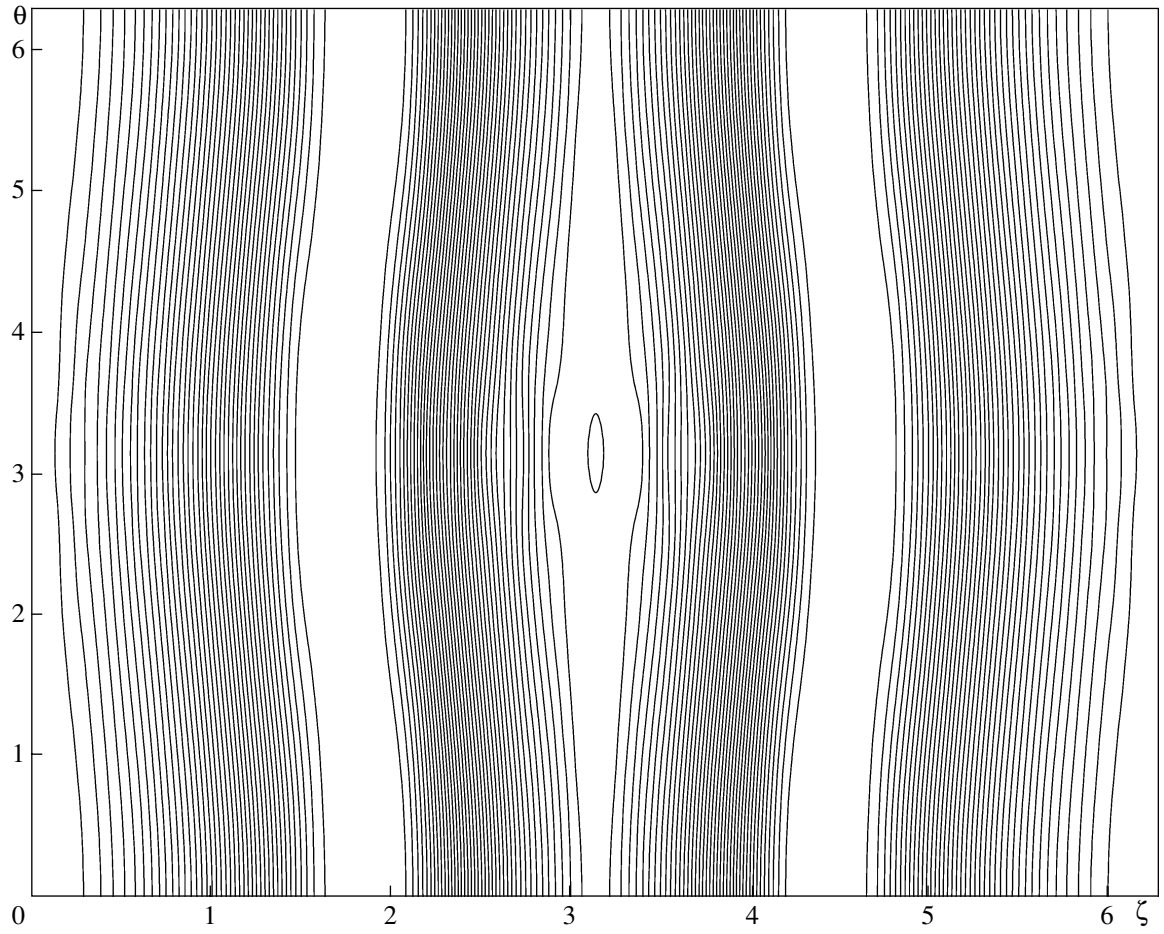

Fig. 4. Isomagnetic contours in the plane of Boozer angular coordinates over one period of a sectionally isometric confinement system.

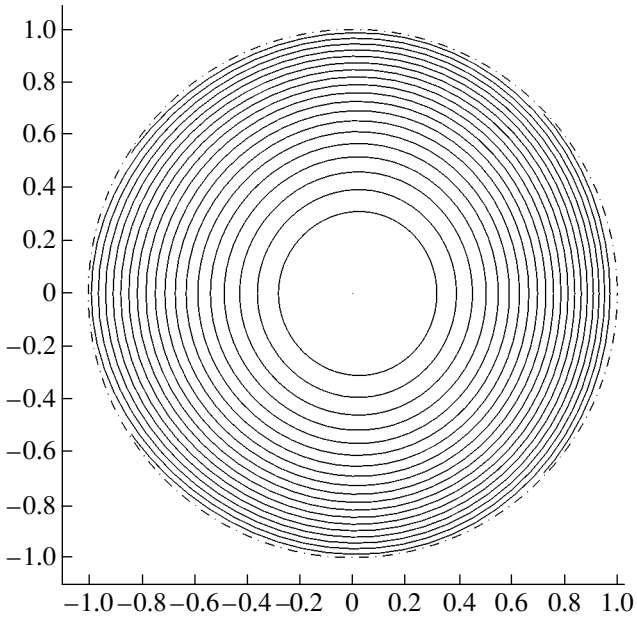

Fig. 5. Contours of the integral $\oint dl/B$ = const at β = 0.1%.

3.2. Equilibrium Calculations

The VMEC code was devised to calculate plasma equilibria in devices with a nonzero rotational transform. Our simulations show that, for "mirror-image" systems with a zero rotational transform, the VMEC code is capable of making more or less accurate predictions of plasma equilibria at low (less than 1%) β values. However, the larger the β value, the more significant the deviation of the surfaces of $\oint dl/B$ = const from the magnetic surfaces calculated by the code (the concentric circles in Fig. 8). Recall that, for the plasma to be in equilibrium in a system with closed magnetic field lines, the integral $\oint dl/B = U(\rho)$ should be constant on the magnetic surfaces.

This deviation from equilibrium conditions is associated with an incorrect formulation of the equilibrium problem for a system with a zero rotational transform and a fixed boundary magnetic surface. At low plasma pressures, the condition $\oint dl/B = U(\rho)$ = const is ensured by

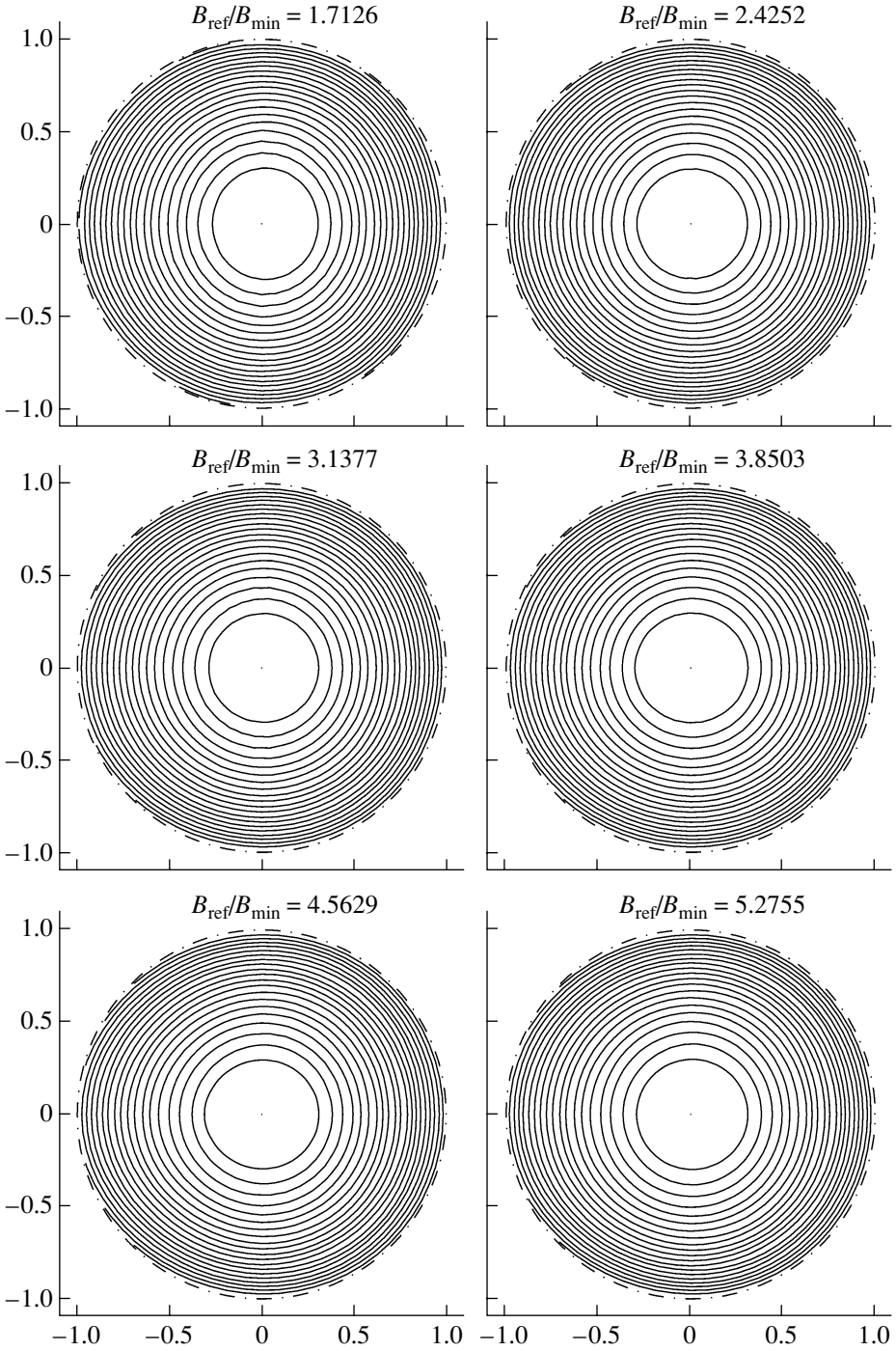

Fig. 6. Contours $J_{\|} = \oint \mathbf{v} d\mathbf{l}$ = const for trapped particles reflected at different mirror ratios B_{ref}/B_{min}.

the procedure proposed here for specifying the boundary magnetic surface from the solution to the vacuum problem. At large β values, the boundary magnetic surface ceases to be equilibrium, so that its shape should be adjusted in a desired fashion. In future numerical investigations, we are going to determine the shape of the boundary magnetic surface satisfying the condition $\oint dl/B = U(\rho)$ = const and the isometry condition for a given β value by selecting the proper set of Fourier harmonics.

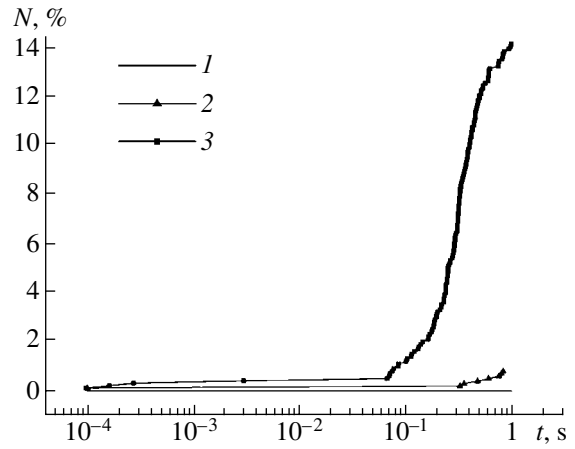

Fig. 7. Time evolution of the number of α-particles, out of 1000, that start from three magnetic surfaces with the radii r = (*1*) 0.25, (*2*) 0.5, and (*3*) 0.75 and are lost from the system.

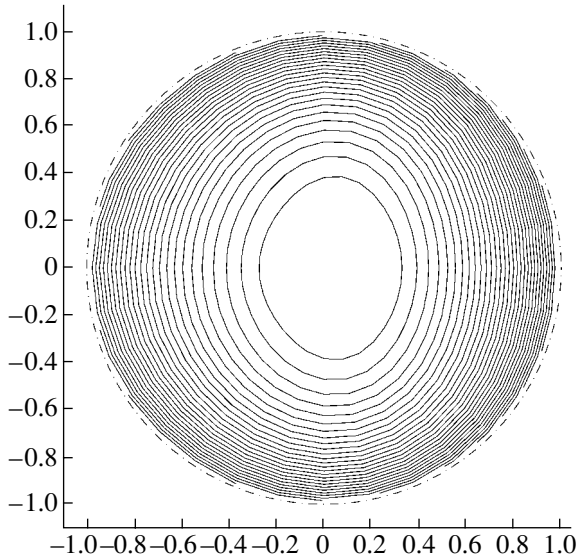

Fig. 8. Contours of the integral $\oint dl/B$ = const at β = 1%.

4. CONCLUSION

The calculations carried out in this paper for a particular toroidally linked, magnetic mirror configuration demonstrate that it is possible to achieve good confinement of drifting particles in a curvilinear mirror system. An effective way of linking mirror cells into a toroidal configuration at low plasma pressures is to satisfy the isometry condition up to second order in the paraxial approximation.

The calculated results show that it is, in principle, possible to link mirror cells into a toroidal configuration capable of providing plasma confinement at a tokamak level.

ACKNOWLEDGMENTS

We are grateful to V.D. Shafranov for supporting this study and to M.I. Mikhaĭlov for useful comments and computational help. We also thank S.P. Hirshman (ORNL) for the opportunity to use the VMEC code in our calculations. This work was supported in part by the Russian Foundation for Basic Research, project nos. 00-15-96526 and 00-02-17105.

REFERENCES

1. B. B. Kadomtsev, *Plasma Physics and the Problem of Controlled Thermonuclear Reactions*, Ed. by M. A. Leontovich (Akad. Nauk SSSR, Moscow, 1958; Pergamon, New York, 1960), Vol. III.
2. R. A. Dory, N. A. Uckan, W. B. Ard, *et al.*, ELMO Bumpy Square Proposal, Report ORNL/TM-9994 (Oak Ridge National Laboratory, 1986).
3. V. P. Pastukhov and H. L. Berk, Nucl. Fusion **33**, 1471 (1993).
4. V. M. Glagolev, B. B. Kadomtsev, V. D. Shafranov, and B. A. Trubnikov, in *Proceedings of the 10th European Conference on Controlled Fusion and Plasma Physics, Moscow, 1981*, Vol. 1, p. E-8.
5. A. Boozer, Phys. Fluids **26**, 496 (1983).
6. J. Nuehrenberg and R. Zille, Phys. Lett. A **129**, 113 (1988).
7. A. A. Skovoroda and V. D. Shafranov, Fiz. Plazmy **21**, 937 (1995) [Plasma Phys. Rep. **21**, 886 (1995)].
8. M. I. Mikhaĭlov, V. D. Shafranov, and D. Sünder, Fiz. Plazmy **24**, 706 (1998) [Plasma Phys. Rep. **24**, 653 (1998)].
9. A. A. Skovoroda, Fiz. Plazmy **26**, 590 (2000) [Plasma Phys. Rep. **26**, 550 (2000)].
10. V. V. Arsenin, E. D. Dlougach, V. M. Kulygin, *et al.*, Nucl. Fusion **41**, 945 (2001).
11. S. P. Hirshman and J. C. Whitson, Phys. Fluids **26**, 3553 (1983).
12. A. Boozer, Phys. Fluids **24**, 1999 (1981).
13. V. D. Shafranov, At. Énerg. **22**, 356 (1967).
14. A. A. Skovoroda and V. D. Shafranov, Fiz. Plazmy **20**, 245 (1994) [Plasma Phys. Rep. **20**, 221 (1994)].
15. J. B. Taylor, Plasma Phys. **9**, 163 (1967).
16. A. A. Subbotin, M. I. Mikhailov, J. Nuehrenberg, *et al.*, in *Proceedings of the 28th EPS Conference on Controlled Fusion and Plasma Physics, Madeira, Portugal, 2001*, p. 5.052.

Translated by I. A. Kalabalyk

Plasma Physics Reports, Vol. 28, No. 9, 2002, pp. 765–772. From Fizika Plazmy, Vol. 28, No. 9, 2002, pp. 831–839.
Original English Text Copyright © 2002 by Hooper, Pearlstein.

MAGNETIC CONFINEMENT SYSTEMS

Hyper-Resistive Modeling in the Spheromak[1]

E. B. Hooper and L. D. Pearlstein

Lawrence Livermore National Laboratory, Livermore, CA 94551, USA

Received February 4, 2002

Abstract—Current drive by coaxial helicity injection in the Sustained Spheromak Physics Experiment (SSPX) is modeled by a hyper-resistive term in Ohm's law for discharges in which magnetic fluctuations are small (1–3%). The current on the open magnetic field lines from the applied vacuum bias flux is assumed completely relaxed; interior to the spheromak, the helicity flux balances the ohmic losses. The poloidal area of the spheromak is found to depend on the strength of the hyper-resistive diffusion coefficient, allowing potentially large amplifications of the vacuum flux and discharge current. One discharge is examined in detail; the best fit to the experimental data finds that a limited fraction of the helicity injected into the flux conserver is effectively applied to current drive interior to the spheromak. © *2002 MAIK "Nauka/Interperiodica".*

We dedicate this paper to our late colleague and warm friend Dmitriĭ A. Panov, in memory of our collaborations in fusion physics and especially in the physics of open (mirror) systems.

1. INTRODUCTION

The current in the spheromak toroidal magnetic configuration can be sustained by injection of helicity from an electrostatic coaxial gun. (References to the extensive spheromak literature can be found in [1, 2].) The mechanism is a magnetic dynamo arising from correlated magnetic and velocity fluctuations. The resulting helicity source in Ohm's law yields a time-averaged steady state configuration. Such sustainment has been studied in several experiments, including CTX [3], FACT [4], SPHEX [5], and SSPX [6].

The current drive source is the injection of magnetic helicity into the flux-conserving wall surrounding the spheromak [7]. The helicity is then coupled into the spheromak from open field lines that intersect the flux conserver. This concept of a primarily axisymmetric spheromak is valid when magnetic fluctuations are not too large, so that a mean-field model is a good representation of the flux surfaces. Consequently, the helicity density inside the spheromak separatrix is a flux function and its transport across flux surfaces is enhanced by the dynamo effect. If the coupling of the fluctuations to the plasma is of sufficiently small scale, it can then be represented as a current diffusion; the resulting dynamo in Ohm's law can be described by a hyper-resistivity [8].

Experimental discharges run in three phases. The first phase, formation of the spheromak, is accompanied with significant MHD activity and, thus, cannot be modeled with the present theory. The second phase, sustainment, generally has moderate levels of MHD activity and can be suitable for modeling with hyper-resistivity. The third phase, decay, generally has increasing MHD activity and terminates with an MHD event; it is thus not suitable for modeling with this theory.

In this paper, we apply the hyper-resistive model to the plasma sustained in the Sustained Spheromak Physics Experiment (SSPX) (Fig. 1), under conditions in which the magnetic fluctuations (at the wall) are ~1–3% [6]. It is with these conditions that the core electron temperatures exceed 100 eV during sustainment. Equally important is that the electron temperature for these conditions is a flux function with a profile peaked on the magnetic axis. The flux dependence of this profile was obtained by comparing Thomson scattering measurements with an equilibrium reconstruction, using the CalTrans/Corsica code and the magnetic probe data [6, 9].

Many discharges in SSPX can be fit with a hyper-resistivity model, although more experimental work will be required to confirm this hypothesis of current diffusion. In the present paper, a simple, *ad hoc* hyper-resistive coefficient is used to fit the limited set of data, yielding an estimate of the magnitude of this coefficient. In future work, this result will be expanded with calculations from a large set of experimental data and compared with nonlinear theories that calculate the hyper-resistivity coefficient explicitly [10–13]. Issues of energy confinement consistent with flux-surface breaking by the current drive are also left to future work.

2. OHM'S LAW WITH HYPER-RESISTIVITY

Ohm's law with hyper-resistivity has the general form [8]

$$\mathbf{E} + \mathbf{v}\times\mathbf{B} = \eta\mathbf{j} - \frac{\hat{\mathbf{b}}}{B}\nabla\cdot(\Lambda\nabla\lambda - \mathbf{u}\times\nabla\lambda) \equiv \mathbf{R}, \quad (1)$$

[1] This article was submitted by the authors in English.

1063-780X/02/2809-0765$22.00 © 2002 MAIK "Nauka/Interperiodica"

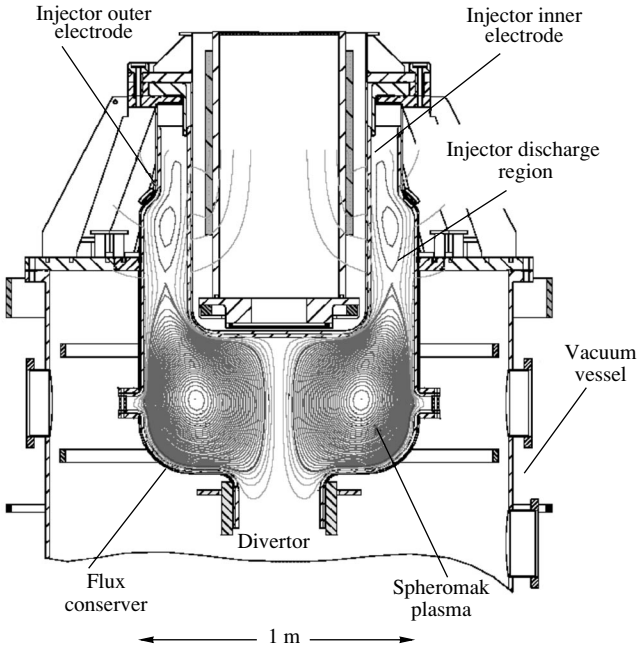

Fig. 1. Cross section of the SSPX spheromak. Bias magnetic coils inside the inner electrode (cathode) provide the flux necessary for electrostatic helicity injection; external coils allow shaping of the vacuum flux surfaces, providing experimental flexibility. A slot on the midplane of the spheromak plasma is used for diagnostic access. Locations of magnetic probes in the flux conserver wall are shown as small circles. Also shown are the poloidal flux surfaces for a "generic" spheromak.

where $\lambda = \mu_0 \mathbf{j}\cdot\mathbf{B}/B^2$, Λ is an arbitrary positive function of position, and $\mathbf{u}$ is an arbitrary vector function of position. In a force-free toroidal plasma that was the basis of the work in [8], λ is a flux function so the term $\mathbf{u}\times\nabla\lambda$ will vanish in the surface-averaged Ohm's law. In this work, we assume that, with a pressure gradient, λ must remain a flux function; consequently, we choose

$$\lambda = \mu_0 \langle \mathbf{j}\cdot\mathbf{B}\rangle / \langle \mathbf{B}\cdot\mathbf{B}\rangle, \tag{2}$$

where the average is defined as

$$\langle \ldots \rangle = \oint (\ldots)\frac{dl}{B}\Big/\oint \frac{dl}{B}. \tag{3}$$

In addition, the velocity $\mathbf{u}$ can now be chosen for convenience; we choose it (in the Appendix) to simplify the classical transport associated with hyper-resistivity. Clearly, this is *ad hoc*; the only justification is that it leads to transport equations without an explicit dependence on the unknown velocity $\mathbf{u}$ [14]. It should be pointed out that this procedure differs from that used by Ward and Jardin [15]; their independent variable remained $j_\parallel/B$ and, then, they used $\mathbf{u}$ to transform Ohm's law into a proper 1D equation. In what follows, we choose Λ to be a flux function as are all other transport coefficients. For this present study, it is further assumed to be a constant.

The poloidal component of Faraday's law together with the surface average of Eq. (1) provides Ohm's law

$$\frac{\partial \Psi}{\partial t} = V_L = 2\pi\left[\eta\frac{\langle \mathbf{J}\cdot\mathbf{B}\rangle}{\langle \mathbf{B}\cdot\nabla\varphi\rangle} - \frac{\partial}{\partial\Phi}\Lambda\langle|\nabla\Phi|^2\rangle\frac{\partial V}{\partial\Phi}\frac{\partial\lambda}{\partial\Phi}\right]. \tag{4}$$

Another important quantity is the gauge invariant helicity,

$$K = \int_0^\Phi (\Psi_{sep} - \Psi)\, d\Phi. \tag{5}$$

Here, V_L is the loop voltage, Ψ is the poloidal flux, and Φ is the toroidal flux. Note that these equations can only be used inside the separatrix; in the cold open field line region, we choose λ to be constant. Of course, other choices could be made, but, for this work, we assume this edge plasma to be completely "relaxed" and can supply helicity at whatever rate required to drive the spheromak plasma current.

Note that the surface averaged currents appearing in Eq. (4) are second order in Φ. Without hyper-resistivity, Eq. (4) is second order in flux and needs only a single boundary condition at the edge since the equation is singular at the axis with natural boundary conditions. With the addition of hyper-resistivity, the equation becomes fourth order and needs an additional boundary condition at the edge. Again, the axis takes care of itself. For this free boundary calculation, we choose one boundary condition to be the value of the loop voltage. In fact, this choice is not arbitrary. It is constrained to synchronize the equilibrium and Ohm's law. Specifically, it is constrained to force the poloidal flux at the separatrix of the plasma as computed in Eq. (4) to be equal to that computed by the free boundary equilibrium solver needed to complete the dynamical calculation. For this work the additional boundary condition is the value of λ at the edge, since that is basically set by the gun current and gun flux. Another choice could be the rate of helicity injection across the separatrix. There is one additional condition, namely the value of the toroidal flux across the spheromak, Φ_m; this is determined by demanding that $F = RB_{tor}$ be continuous across the plasma separatrix.

The formal procedure for obtaining Eq. (4) was to use a coordinate system in which the toroidal flux is the independent coordinate. As such, from the remaining components of Faraday's law [14], we learn that the fluid velocity relative to this moving coordinate system is given by

$$\mathbf{v}\cdot\nabla\Phi = (\langle 2\pi R^2 \mathbf{R}\cdot\nabla\varphi\rangle - V_L). \tag{6}$$

This result will then be used in the Appendix to calculate the hyper-resistive correction to classical transport. Finally, in order to work with a fixed coordinate system,

we use the dimensionless toroidal flux, $\hat{\Phi} = \Phi/\Phi_m$, as the independent coordinate.

Next, we consider the properties of Eq. (4). There are two time scales; in one of them, the first term on the right-hand side balances the left-hand side producing the usual L/R time; in the other, the last term on the right-hand side does the balancing producing a hyper-resistive time scale. Now, to describe the behavior of this equation, it is easiest to consider the limit in which Λ is "large" compared with the resistivity. In this case, Ψ evolves until the two terms on the right-hand side balance; this is accomplished by both flattening the λ profile and increasing the poloidal area of the spheromak. As a consequence, the flux hole along the geometric axis contracts and the difference in poloidal flux across the plasma amplifies. Clearly, in the opposite limit where the resistivity is "large", the hole expands, the λ profile steepens, and the plasma area shrinks. Since we are not interested in the specific dynamics of hyper-resistivity, but rather in its time-averaged behavior only, the time asymptotic results of Eq. (4), where the two terms balance, will be compared with the experiment. Further, since the duration of the sustainment phase of the experiment usually exceeds the L/R time, and since the experimental data indicates that the plasma is in equilibrium or evolving slowly, we can compare with the theory in steady state.

3. APPLICATION TO THE SSPX EXPERIMENT

In SSPX, a spheromak is formed and sustained by coaxial helicity injection from a "gun" operated at a current $I_{\rm gun}$ also known as the discharge current, and magnetic flux $\Phi_{\rm gun}$ generated by external power systems. The rate of helicity injection into the flux conserver is $2\Phi_{\rm gun}V_{\rm gun}$, where $V_{\rm gun}$ is the gun voltage. The helicity is injected onto the open magnetic field lines which pass through the flux conserver wall. Some fraction of the helicity is then transferred to the spheromak, where it maintains the plasma current; the remainder is lost in the sheaths at the walls and to ohmic dissipation on the open lines. In the following, we will not model the mechanisms for the transfer from open lines; instead, we determine the helicity required to sustain spheromaks over a parameter range including those measured in the experiment. Calculation of the rate of helicity crossing the separatrix at the experimental current is then compared with $2\Phi_{\rm gun}V_{\rm gun}$, determining the fraction of $V_{\rm gun}$ consumed by sustaining the spheromak.

The time history of the discharge analyzed here is shown in Fig. 2. SSPX has been designed [9] with a flexible bias magnetic field system, which allows sustained operation with $\lambda_{\rm gun} = \mu_0 I_{\rm gun}/\Phi_{\rm gun}$ comparable to the lowest eigenvalue, λ_{FC}, of the flux conserver, calculated by the solution of $\nabla \times \mathbf{B} = \lambda_{FC}\mathbf{B}$. Further, the value of $\lambda(\Phi)$ in the plasma (including open field lines) must span the lowest eigenvalue [16], 9.8 m^{-1}, in SSPX. To

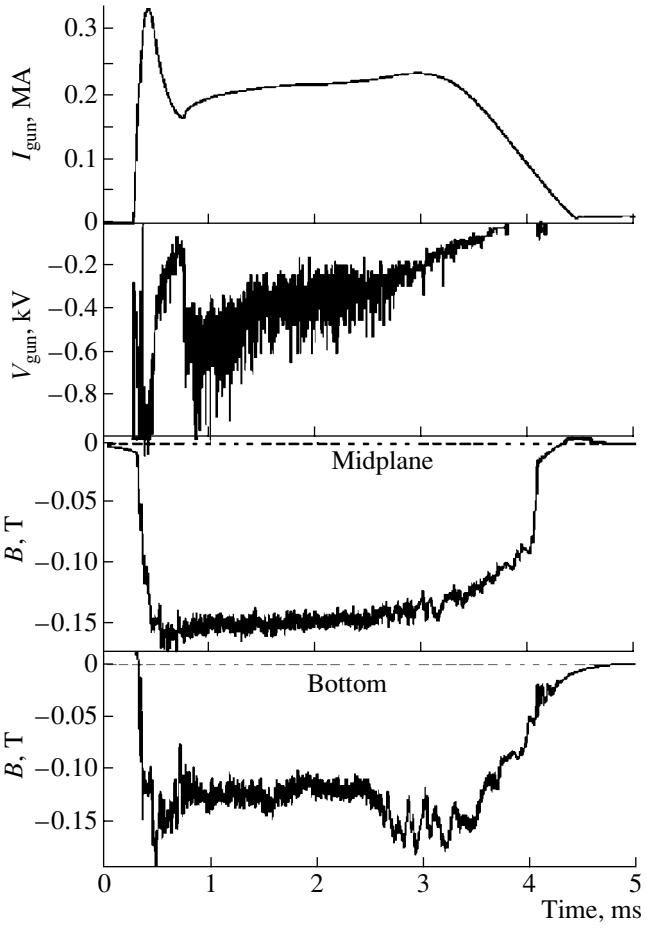

Fig. 2. Time history of shot no. 7052. Shown are the discharge current and voltage, as well as the poloidal magnetic field at the flux conserver wall just above the diagnostic slot and on the bottom of the flux conserver; $\lambda_{\rm gun} = 10.3\ m^{-1}$.

replace helicity losses in the spheromak, λ on the separatrix must be greater than this value. Consequently, operating near the eigenvalue allows sustainment with weak gradients in λ throughout the plasma. As the drive for resistive modes is proportional to this gradient [17], magnetic fluctuations are expected and found to have a low amplitude. These fluctuations (as measured by wall currents flowing in rods bridging the diagnostic slot in the flux conserver wall, Fig. 1) show several low toroidal mode numbers, n = 1, 2, 3, and 4 (Fig. 3). Their interference leads to coherence times comparable to the rotation time of the discharge. This combination of fluctuations with low amplitude and low coherence are generally consistent with a current diffusion model, although further measurements will be needed to justify this assumption. Electron temperature measurements using Thomson scattering show that this discharge has peaked electron temperatures of 50–80 eV, rather less than the maximum observed in the "best" discharges; for modeling purposes, we take 50 eV on the magnetic axis and with $Z_{\rm eff}$ = 2.5 and assume the

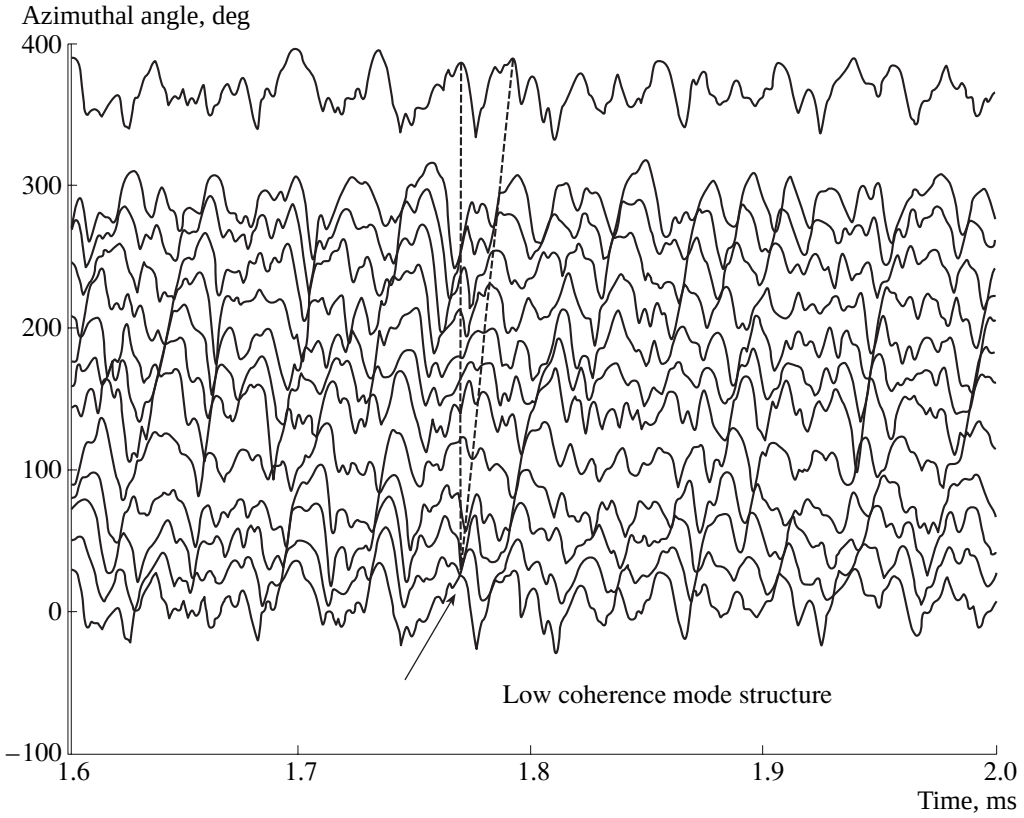

Fig. 3. Fluctuations in the wall current measured at 12 azimuthal locations in the rods bridging the diagnostic slot (Rogowski signals, shot no. 7052). The top and bottom traces are the same signal, connected with lines that indicate relative times at each azimuth.

temperature profile to be linear in $\hat{\Phi}$, dropping to 15 eV on the open field lines.

We apply our analysis to this discharge at 1.8 ms, when the discharge has reached a quasi-steady state, although possibly with a slowly varying current profile. The starting point is the MHD equilibrium found by fitting the plasma current profile and current to the poloidal magnetic field data from the probes identified in Fig. 1. An acceptable reconstruction has λ taking the form $\lambda(\hat{\Psi}) = \lambda_{gun}(1 + a\hat{\Psi}^2)/(1 + a)$, where $\hat{\Psi}$, the poloidal magnetic flux normalized to the flux between the separatrix and magnetic axis, ranges from 0 on the magnetic axis to 1 on the separatrix. The value of λ on the open field lines is then λ_{gun}. (We have found that the current, flux, and average λ are insensitive to the precise form of the fit.) For this particular discharge, we find that the fraction of the gun current passing through the hole is 142 kA, the toroidal plasma current inside the separatrix is 145 kA, and that $\lambda_{gun} = 10.3\ m^{-1}$ with $a = 0.29$.

The solution of Ohm's law with the resistivity profile determined by the electron temperature, together with the free-boundary equilibrium for the SSPX geometry, requires knowing the vacuum magnetic flux distribution frozen into the cathode and flux conserver walls; this is provided by the initial vacuum bias field. Together with the discharge current, the vacuum flux yields λ_{gun}. One further parameter needs to be specified: Λ, or the toroidal plasma current in the spheromak, or the helicity flux at the separatrix. To compare with experiment, we evaluate the discharge properties over a wide range of Λ. The results of the model are then fit to the discharge by determining Λ which matches the plasma current determined from the equilibrium fit to the data. (This effectively fits the experimental magnetic probe data, as shown below.)

The flux configuration is shown in Fig. 4 for two values of Λ (note the change in poloidal area corresponding to large differences in amplification of the gun flux and current). The values of the gun flux and current through the hole along the geometric axis are approximately independent of the spheromak plasma current, changing somewhat with the electrode intersection with the separatrix limiting the open field lines which encircle the spheromak. As the spheromak current increases with the hyper-resistive coefficient, the magnetic field on and near the geometric axis increases. To maintain the open flux, the hole radius shrinks, as is seen in the figure. The radius can be estimated to ~70% by calculating the flux due to the spheromak current, approximating it as a toroidal filament on the magnetic axis.

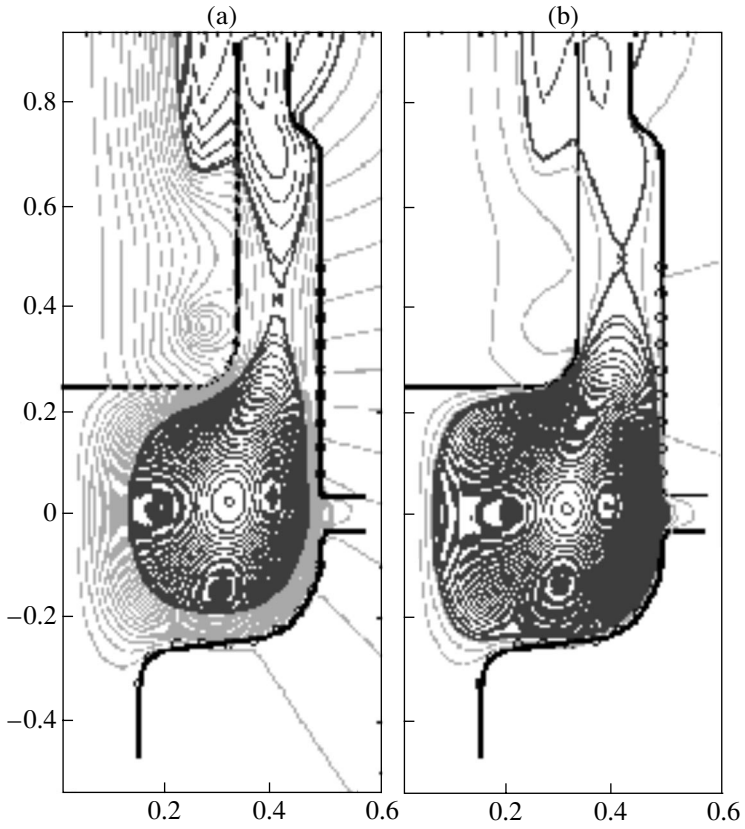

Fig. 4. Spheromak equilibria at (a) $\Lambda = 0.0091$ V Wb, $I_{pl} = 142$ kA and (b) $\Lambda = 1.0$ V Wb, $I_{pl} = 882$ kA.

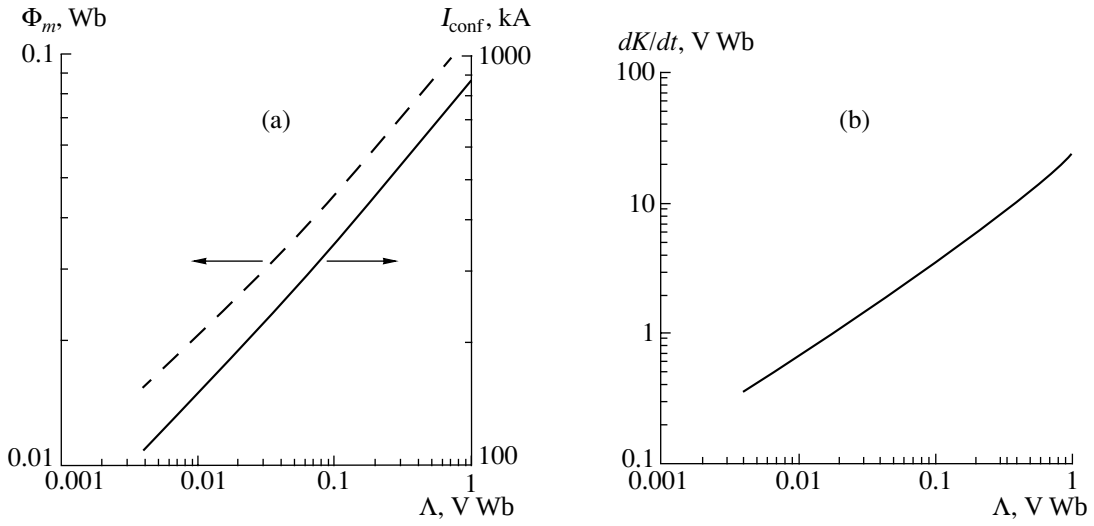

Fig. 5. (a) Toroidal magnetic flux on the separatrix (dashed line) and confined toroidal current (solid line). The applied gun flux which passes through the hole on the geometric axis varies from 0.017 Wb for $\Lambda = 0.004$ to 0.022 Wb for $\Lambda = 1$. (b) Helicity injection rate at the separatrix.

The toroidal flux on the separatrix and the helicity injected across the separatrix are plotted in Fig. 5. As the confined current increases with Λ at fixed gun current and flux, λ on the magnetic axis approaches the flux conserver eigenvalue from below, but the edge value, λ_{gun}, is fixed. Consequently, the helicity is driven by a weaker gradient, so that the flux and current amplifications increase more slowly than linearly with Λ.

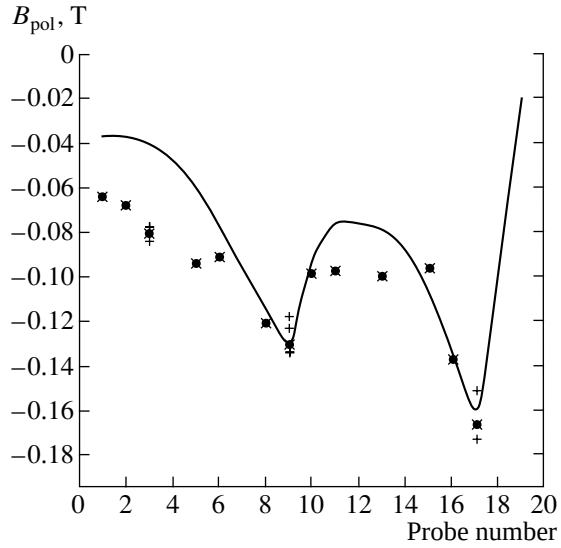

Fig. 6. Calculated poloidal magnetic field at the wall for Λ = 0.0092 (solid line), compared with probe data (crosses) for t = 1.8 ms (shot no. 7052). The probe locations (Fig. 1) are numbered from 1 at the top to 20 at the bottom of the flux conserver. Missing data points correspond to locations which do not presently contain probes.

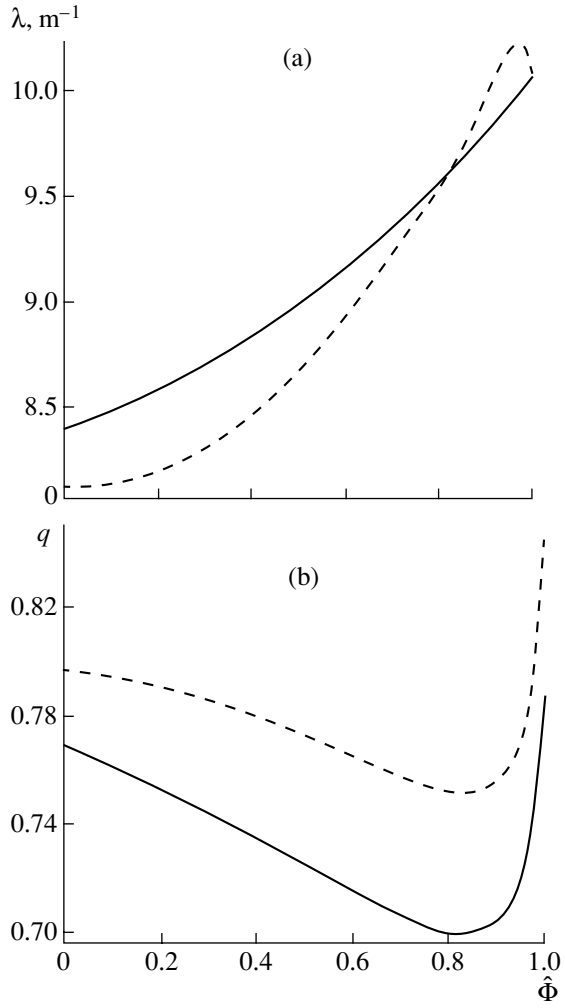

Fig. 7. Profiles resulting from the fits to the magnetic probe data, comparing the results of the initial reconstruction (dashed line) with the results from the hyper-resistivity calculation (solid line) for Λ =0.0092: (a) λ profile and (b) q profile.

The measured confined current corresponds to Λ = 0.0091 V Wb. The magnetic field at the wall is compared with probe data in Fig. 6 and is found to be as good as the fit used to start the calculation. At other values of Λ, the calculated probe fields are significantly different. The calculated profiles of λ and q are shown in Fig. 7 as functions of the normalized poloidal flux. The lack of low order (m, n) rational surfaces found from the q profile is consistent with the low amplitude of magnetic fluctuations.

The calculated rate of helicity transport across the separatrix is 0.62 V Wb. At the calculated value of the gun flux which passes through the poloidal hole, 0.017 Wb, the effective voltage applied to the confined spheromak is 19 V, which is much less than the applied voltage (≈350 V). Also, the helicity injected into the spheromak is small compared to the helicity supplied by the gun. This result follows from the assumed electron temperature and Z_{eff}, although likely variations in these will not increase the effective voltage by a large amount. The fact that the resultant effective voltage applied to the spheromak is small is consistent with experimental measurements which find that the bulk of the voltage drop is across the sheath and along the open field lines [18].

The helicity drive also depends strongly on λ_{gun}, since the helicity transport across the separatrix is proportional to $\partial\lambda/\partial\hat{\Phi}$. As an example, flux surfaces in a discharge operating at λ_{gun} = 14.0 m^{-1} are shown in Fig. 8. The best fit to the hyper-resistivity had Λ = 0.0039 V Wb with a helicity injection into the spheromak of 1.70 V Wb, corresponding to an effective helicity drive voltage of 63 V.

4. DISCUSSION

We have modeled a discharge in SSPX using Ohm's law in which the dynamo is approximated by hyper-resistive diffusion. The approximation is applied within the spheromak separatrix and assumes that the open-field region is completely relaxed (with constant λ). In this limit, helicity transport into the spheromak is determined by the balance between interior ohmic losses and the hyper-resistivity. This in turn determines the amplification of vacuum flux and current by the spheromak. Comparison of the fit to the experimental data analyzed here with the total helicity injected into the flux conserver indicates that only a small fraction is transferred to the spheromak, with most of the helicity lost in

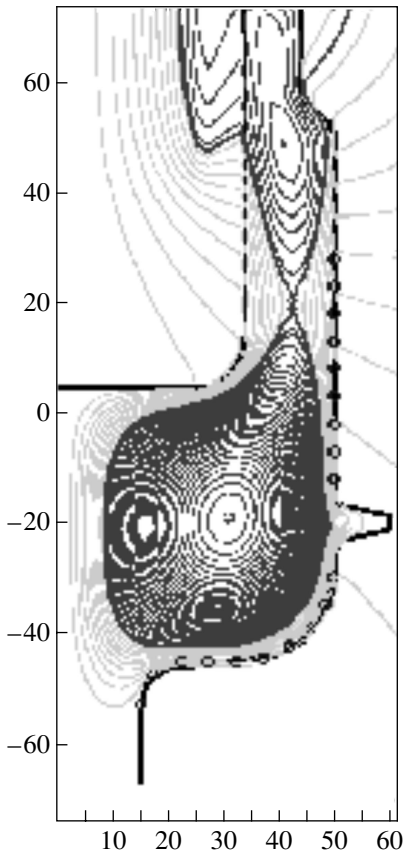

Fig. 8. Poloidal flux surfaces for shot no. 7226 at 1.8 ms. For this discharge, the gun current along the geometric axis was calculated to be 0.155 MA, the confined current was 0.267 MA, and $\lambda_{gun} = 14.0\ m^{-1}$.

sheaths at the walls and in dissipation in the cold plasma on open field lines.

The spheromak magnetic flux and current shown in Fig. 5 scale less than linearly with Λ. Further, the values of Λ needed to fit the few discharges analyzed to date are similar. If this holds in general, the value may provide significant constraints on the dynamo responsible for the sustainment. Comparison of this value with calculations of hyper-resistive coefficients will help address the issue of whether the experimentally observed current is limited by helicity balance in the spheromak, the coupling of helicity from the edge plasma column, or both.

Within the hyper-resistive model, the amplification of applied flux and current are potentially quite large, providing the possibility that losses on the open lines can be reduced significantly relative to those in the spheromak. An important caution is that the limiting factor may be the coupling from the open field lines to the spheromak, an issue not addressed here. There is evidence that a strong $n = 1$ mode can drive this coupling [19, 20], but improved field and flux amplification requires that magnetic fluctuations not badly open the mean-field flux surfaces, which would allow large energy losses and produce low electron temperatures and high resistivity.

ACKNOWLEDGMENTS

We gratefully acknowledge the SSPX Team, D.N. Hill, H.S. McLean, B.W. Stallard, R.D. Wood, and S. Woodruff, both for the experimental results and many enlightening discussions. We also appreciate enlightening discussions with L.L. LoDestro. R.H. Bulmer provided considerable assistance in inverting the experimental measurements to generate the MHD equilibrium used as the starting point in the modeling. This work was performed under the auspices of the U.S. Department of Energy by the University of California Lawrence Livermore National Laboratory under contract no. W-7405-Eng-48.

APPENDIX

CLASSICAL TRANSPORT DUE TO HYPER-RESISTIVITY

Here, we determine the correction to classical transport due to hyper-resistivity. Classical particle transport has the form

$$\frac{\partial N}{\partial t} = \frac{\partial}{\partial \Phi}\Gamma N + \text{Source}, \tag{A.1}$$

where

$$N = n\oint \frac{dl}{qB} \tag{A.2}$$

and

$$\Gamma = \langle \mathbf{v}\cdot\nabla\Phi\rangle. \tag{A.3}$$

Now, with Eq. (6), we see that there are two contributions to Γ from hyper-resistivity; one is already accounted for in V_L and the other comes from the explicit dependence on the first term of Eq. (5). The sum can be written as

$$\Gamma^{HR} = 2\pi q\left[\left\langle -\frac{F}{B^2}\nabla\cdot(\Lambda\nabla\lambda - \mathbf{u}\times\nabla\lambda)\right\rangle - \frac{V_L^{HR}}{2\pi}\right], \tag{A.4}$$

where q is the safety factor and $F = RB_{tor}$. Now, the first term in the square bracket can be rewritten as

$$\frac{\langle B_{tor}^2\rangle}{\langle B^2\rangle}\left[\frac{\partial}{\partial\Phi}A\left\langle\frac{|\nabla\Phi|^2}{B^2}\right\rangle\langle B^2\rangle\frac{\partial\lambda}{\partial\Phi} + \text{terms}\right].$$

Here, B_{tor} is the toroidal magnetic field and *terms* has the unpleasant form depending on u_θ,

$$\langle a(\Phi,\theta) + \beta(\Phi,\theta)u_\theta\rangle\frac{\partial\lambda}{\partial\Phi}.$$

This term can be eliminated by the appropriate choice of u_θ. Finally, the hyper-resistive correction has the form

$$\Gamma^{HR} = 2\pi q\left[\frac{\langle B_{\rm tor}^2\rangle}{\langle B^2\rangle}\frac{\partial}{\partial\Phi}\frac{\Lambda}{2\pi}\left\langle|\nabla\Phi|^2\left(1-\frac{\langle B^2\rangle}{B^2}\right)\right\rangle\frac{\partial\lambda}{\partial\Phi} - \frac{\langle B_{\rm pol}^2\rangle}{\langle B^2\rangle}V_L^{HR}\right], \quad \text{(A.5)}$$

where $B_{\rm pol}$ is the poloidal magnetic field.

Note that this is the way the loop voltage comes in for the usual η driven part, which is what led us to the specific choice of u_θ.

REFERENCES

1. T. R. Jarboe, Plasma Phys. Controlled Fusion **36**, 945 (1994).
2. P. M. Bellan, *Spheromaks* (Imperial College Press, London, 2000).
3. T. R. Jarboe, I. Hennins, A. R. Sherwood, *et al.*, Phys. Rev. Lett. **51**, 39 (1983).
4. N. Nagata, T. Kanki, T. Matsuda, *et al.*, Phys. Rev. Lett. **71**, 4342 (1993).
5. M. G. Rusbridge, S. J. Gee, P. K. Browning, *et al.*, Plasma Phys. Controlled Fusion **39**, 683 (1997).
6. H. S. McLean, S. Woodruff, E. B. Hooper, *et al.*, Phys. Rev. Lett. **88**, 125004 (2002).
7. J. B. Taylor and M. F. Turner, Nucl. Fusion **29**, 219 (1989).
8. A. H. Boozer, J. Plasma Phys. **35**, 133 (1986).
9. E. B. Hooper, L. D. Pearlstein, and R. H. Bulmer, Nucl. Fusion **39**, 863 (1999).
10. A. R. Jacobson and R. W. Moses, Phys. Rev. A **29**, 3335 (1984).
11. H. R. Strauss, Phys. Fluids **29**, 3668 (1986).
12. A. Bhattacharjee and E. Hameiri, Phys. Rev. Lett. **57**, 206 (1986).
13. G. G. Craddock, Phys. Fluids B **3**, 316 (1991).
14. J. Blum and J. LeFoll, Comput. Phys. Rep. **1**, 465 (1984); a set of lecture notes due to S. C. Jardin, private communication.
15. D. J. Ward and S. C. Jardin, Nucl. Fusion **29**, 905 (1989).
16. D. A. Kitson and P. K. Browning, Plasma Phys. Controlled Fusion **32**, 1265 (1990).
17. A. H. Boozer, *Plasma Confinement*, in *Encyclopedia of Physical Science and Technology* (Academic, New York, 1992), Vol. 13, p. 1.
18. B. W. Stallard, private communication (2001).
19. A. al-Karkhy, P. K. Browning, G. Cunningham, *et al.*, Phys. Rev. Lett. **70**, 1814 (1993).
20. R. C. Duck, P. K. Browning, G. Cunningham, *et al.*, Plasma. Phys. Controlled Fusion **39**, 715 (1997).

Plasma Physics Reports, Vol. 28, No. 9, 2002, pp. 773–775. From Fizika Plazmy, Vol. 28, No. 9, 2002, pp. 840–842.
Original English Text Copyright © 2002 by Fowler, Hua.

MAGNETIC CONFINEMENT SYSTEMS

Heat Confinement in Spheromaks[1]

T. K. Fowler and D. D. Hua

Department of Nuclear Engineering, University of California, Berkeley, CA 94720-1730, USA

Received December 14, 2001

In Memory of Dmitriĭ Panov

Abstract—Calculations are presented showing the temperatures expected in a spheromak sustained by continuous injection of helicity, based on a model previously shown to agree with temperatures achieved in spheromak experiments carried out in the 1980's. New experiments with Thomson scattering measurements of electron temperature will provide an experimental test. © *2002 MAIK "Nauka/Interperiodica".*

1. INTRODUCTION

The spheromak is a potentially attractive concept for compact fusion reactors, either in steady state or pulsed operation [1]. The unique feature of the spheromak is the possibility of creating very strong magnetic fields using an electrostatic Marshall gun to inject helicity into a metal flux conserver that, in the case of the pulsed reactor, confines the plasma without the need for externally produced magnetic fields.

The price paid for these simplifications is magnetic turbulence associated with relaxation of the injected currents into a stable Taylor configuration [2]. However, by injecting helicity at a controlled rate, on time average, the turbulence needs to be only strong enough to cause relaxation on the time scale of ohmic decay, which is the competing process by which a stable state is distorted into an unstable state. Models based on this idea appeared to explain temperatures achieved in the CTX spheromak in the 1980s [3]. Here, we apply the model to predict temperatures in the new SSPX spheromak facility [4].

2. TRANSPORT MODEL

Our calculations employ a heat transport code using the model of [3]. We refer to that paper and [5] for a description of the equations. The heat diffusivity χ includes both a term due to magnetic turbulence (electron channel) and an ion classical heat diffusion term, and also a gyrobohm term important at high temperatures but not at temperatures of a few hundred eV anticipated in SSPX.

The term in χ representing magnetic turbulence is that due to Rechester and Rosenbluth, of the form [6]:

$$\chi_{MAG} = v_e L_C \frac{\langle \delta B^2 \rangle}{B^2}, \quad (1)$$

where $\langle\ \rangle$ denotes a space-time average; v_e is the electron thermal speed; and $L_C = 3a$ is a magnetic correlation length with spheromak minor radius a, calibrated to CTX temperature data (a correction to [3], which gave $L_C = 5a$).

The expression for magnetic fluctuations used in our transport code is derived in [3, 5]. It is a version of S-scaling [7], giving

$$\frac{\langle \delta B^2 \rangle}{B^2} \approx \frac{g_P}{S}, \quad (2)$$

where S is the Lundquist number (ratio of the properly averaged ohmic decay time to the Alfvén transit time) and g_P is the enhancement factor. Our formula for g_P, derived from the Poynting flow of magnetic energy needed to restore the magnetic field to Taylor's relaxed state, causes fluctuations to be enhanced in proportion to the power driving build up of the magnetic field in the spheromak [3]. In a steady state, $g_P \approx 1$. We refer the reader to [5] for details.

The physical significance of Eq. (1) lies in a calculation of chaotic wandering of magnetic field lines in space, giving line lengths L of order [6]

$$L = \frac{2\pi a}{\frac{\langle \delta B^2 \rangle}{B^2}} \approx 2\pi a \frac{S}{g_P}. \quad (3)$$

Then, collisional transport across field lines gives a heat transport in the radial direction that usually exceeds parallel transport along field lines: $\chi_{MAG}/a^2 > v_e\lambda/L^2$ if $\langle \delta B^2 \rangle / B^2 < 4\pi^2 (L_C/\lambda)$, where λ is the electron mean free path. This criterion is satisfied over a wide range of parameters, and our transport code using Rechester–Rosenbluth transport seems to explain temperatures obtained in CTX [3].

[1] This article was submitted by the authors in English.

1063-780X/02/2809-0773$22.00 © 2002 MAIK "Nauka/Interperiodica"

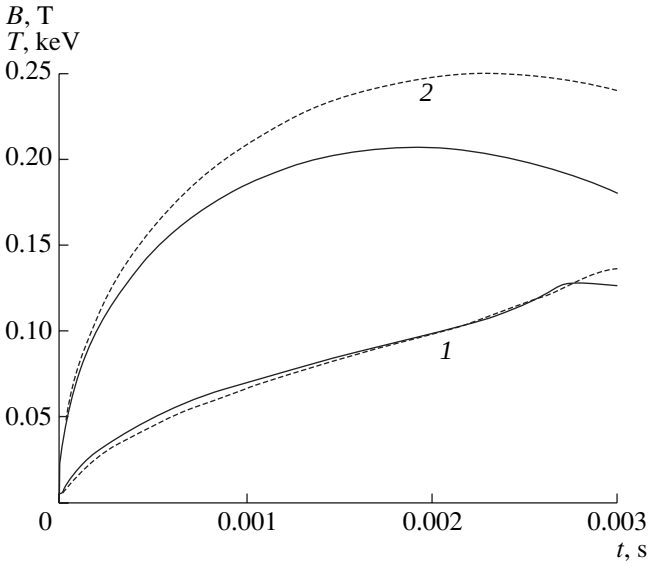

Fig. 1. (*1*) Core temperature and (*2*) magnetic field evolution for $Z_{\text{eff}} = 1$ (dashed lines) and 2 (solid lines).

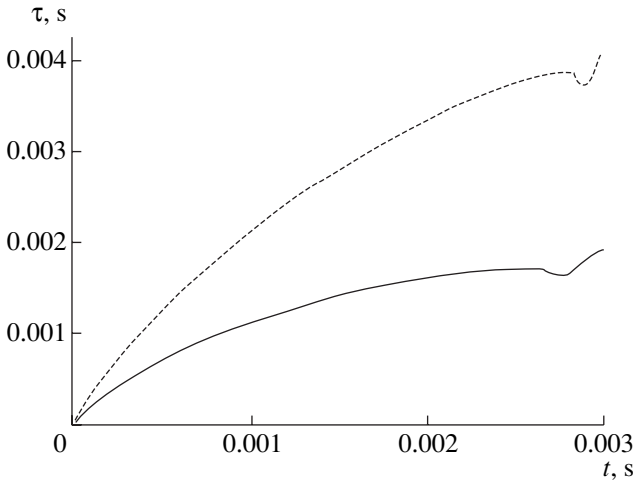

Fig. 2. Ohmic decay time evolution for $Z_{\text{eff}} = 1$ (dashed line) and 2 (solid line).

3. RESULTS

Figures 1 and 2 show results for buildup of a spheromak by gun injection using our heat transport code to calculate temperatures during buildup. Buildup of the field is calculated from

$$\frac{dE_{MAG}}{dt} = P(t) - \int \eta j^2 dV, \tag{4}$$

where E_{MAG} is the magnetic energy in the spheromak assuming approximately a Taylor state and P is the useful fraction of the gun power going toward buildup of the field energy. We are developing models of $P(t)$ to represent the constant current power supply in SSPX and the spheromak impedance R_S giving a voltage $V = IR_S$ in response to a gun current I. Here, we will simply specify $P(t)$ representative of gun powers measured in the experiment.

Figure 1 shows the buildup of the magnetic field and temperature with power input given by

$$P(t) = 20 \text{ MW} \left[1 - \frac{t}{t_0}\right] \tag{5}$$

for a pulse duration $t_0 = 3$ ms. The peak field $B = 0.2$ T corresponds to $E_{MAG} = 10$ kJ in a cylindrical flux conserver of radius $R = 0.5$ m and length R.

The ohmic decay power $\int \eta j^2 dV$ in Eq. (4) appears as ohmic heating in the heat transport equation. We assume constant density $n = 10^{20}$ m^{-3}. We show results for two cases, $Z_{\text{eff}} = 1$ and 2. The temperature is not much affected since Z_{eff} appears in both the ohmic heating term and the Rechester–Rosenbluth loss term, giving a maximum temperature $T = 0.1$ keV near the end of the pulse.

The magnetic field is affected by Z_{eff} because the ohmic decay time is affected. The ohmic decay time is shown in Fig. 2, given by

$$\tau = \frac{E_{MAG}}{\int \eta j^2 dV}. \tag{6}$$

We see that τ rises as the temperature rises, allowing prolonged sustaining of the field even though the power input is falling by Eq. (5).

4. DISCUSSION

We have carried out calculations of temperatures expected to be obtained by ohmic heating during buildup of the magnetic field by gun injection in the SSPX spheromak. The predicted temperatures, in the range of 0.1 keV, have previously been observed in spheromaks during quiet periods or decay but data has not been available during buildup in SSPX.

Maintaining temperatures sufficient to limit ohmic losses well below the input power is essential for buildup to high magnetic fields. Indeed, in our calculations $\int \eta j^2 dV$ is almost constant, so that a power level sufficient to initiate buildup is sufficient to sustain buildup for as long as the power lasts. This result follows from S-scaling, which predicts approximately constant β with ohmic heating and Rechester–Rosenbluth transport [8], giving $\tau \propto B^2$ as shown in Fig. 3.

As we have seen, S-scaling implies magnetic field lines of long length, of order Sa by Eq. (3), where $S \approx 10^5$ in SSPX, or shorter lines that only appear intermittently as flux surfaces open and close, with duty factor S^{-1}. Recent MHD simulations of spheromaks using the NIMROD code find much shorter open field lines that

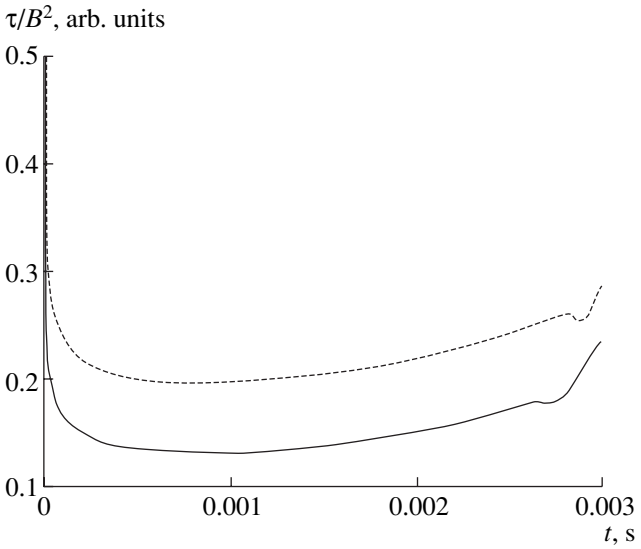

Fig. 3. Ratio of the ohmic decay time to magnetic energy at a constant density for $Z_{\text{eff}} = 1$ (dashed line) and 2 (solid line).

persist during gun injection [9]. It is the use of temperature as a diagnostic to distinguish between persistently short or long field lines that has motivated the calculations presented here.

Agreement between predictions by our heat transport model and temperature measurements in SSPX would be encouraging for future research on spheromaks. Our χ_{MAG}, being collisional in origin, turns out to be similar to classical ion thermal transport (also included in our code), giving

$$\frac{\chi_{MAG}}{\chi_{\text{class}}} \approx \frac{g_P}{2\sqrt{\beta}}, \tag{7}$$

where β is the usual ratio of kinetic to magnetic pressure. Classical losses also give constant β with ohmic heating.

Eventually gyrobohm transport would be expected to dominate in spheromaks at fields above 1 T [8]. Even so, reactor studies with our transport model show that ohmic ignition might be possible at a higher field [1].

REFERENCES

1. T. K. Fowler, D. D. Hua, E. B. Hooper, *et al.*, Comments Plasma Phys. Control. Fusion, Comments Mod. Phys., Part C **13**, 83 (1999).
2. J. B. Taylor, Rev. Mod. Phys. **58**, 741 (1986).
3. T. K. Fowler and D. D. Hua, J. Fusion Energy **14**, 181 (1995).
4. D. N. Hill, R. H. Bulmer, B. I. Cohen, *et al.*, in *Proceedings of the 18th IAEA Fusion Energy Conference, Sorrento, Italy, 2000* (UCRL-JC-13828).
5. T. K. Fowler and D. D. Hua, Fiz. Plazmy **23**, 777 (1997) [Plasma Phys. Rep. **23**, 719 (1997)].
6. A. B. Rechester and M. N. Rosenbluth, Phys. Rev. Lett. **40**, 38 (1978).
7. N. Mattor, Phys. Plasmas **3**, 1578 (1996).
8. T. K. Fowler, Fusion Technol. **29**, 206 (1996).
9. C. R. Sovinec, J. M. Finn, and D. del-Castillo-Negrete, Phys. Plasmas **8**, 475 (2000).

Plasma Physics Reports, Vol. 28, No. 9, 2002, pp. 776–778. Translated from Fizika Plazmy, Vol. 28, No. 9, 2002, pp. 843–845.
Original Russian Text Copyright © 2002 by Arsenin.

MAGNETIC CONFINEMENT SYSTEMS

Stability of Localized MHD Perturbations in Confinement Systems with Closed Magnetic Field Lines

V. V. Arsenin

Institute of Nuclear Fusion, Russian Research Centre Kurchatov Institute, pl. Kurchatova 1, Moscow, 123182 Russia

Received March 17, 2002

Abstract—Conditions are determined for the stability of a finite-pressure plasma against perturbations localized near a magnetic field line in a magnetic confinement system without average minimum-B. The marginal stability ($\omega^2 = 0$) is achieved at the pressure profile $p \propto U^{-5/3}$ (where $U = \oint \frac{dl}{B}$), provided that the pressure is lower than a certain critical value above which an unstable incompressible mode in which the displacement as a function of the coordinate along the field line has zeros appears at some magnetic field line. © *2002 MAIK "Nauka/Interperiodica".*

1. In confinement systems with closed magnetic field lines, the plasma compressibility may play an important role in MHD-stabilizing convective perturbations. For a plasma with an isotropic pressure ($p_\perp = p_\parallel = p$) in a configuration without a magnetic well, the condition for stability against flute modes has the form [1]

$$W = \nabla p \cdot \nabla U + \gamma p \frac{(\nabla U)^2}{U} \geq 0, \quad (1)$$

where $U = \oint \frac{dl}{B}$ and $\gamma = 5/3$. The marginal stability condition is

$$W = 0, \quad (2)$$

the corresponding marginal pressure profile being

$$p \sim U^{-\gamma}. \quad (3)$$

Criterion (1) is valid, in particular, for a finite-pressure plasma, $\beta = 2p/B^2 \neq 0$ (where the quantity U is to be calculated from an actual equilibrium magnetic field). In criterion (1), the second stabilizing term, associated with the plasma compressibility, is important for nonparaxial systems, in which $|\nabla B/B| \gtrsim |\nabla p/p|$. The inequality in criterion (1) imposes a restriction on the radial pressure profile. If, at the plasma periphery, there is a separatrix surface (in the immediate vicinity of which we have $U \longrightarrow \infty$), then there exist convectively stable pressure profiles such that the pressure vanishes at this surface.

As was shown in [2], the plasma equilibrium in an axisymmetric configuration of the poloidal (meridional) magnetic field is stable against arbitrary perturbations if (a) condition (1) is satisfied and if (b) the wave equation describing perturbations with large azimuthal mode numbers ($m \longrightarrow \infty$) at any magnetic field line without allowance for the plasma compressibility has no unstable solutions such that the displacement as a function of the coordinate along the field line has zeros. Note that requirement (b) determines the maximum possible β value consistent with MHD plasma stability. The results obtained in [3] on a dipole magnetic configuration with a levitated current-carrying ring illustrate how requirements (a) and (b) can be used in the calculations of the plasma stability.

The use of the stabilizing effect of nonparaxial elements expands the possibilities of creating MHD stable systems with closed magnetic field lines. Interest in such systems is associated, in particular, with a search for configurations that ensure the lowest possible transport across the magnetic surfaces [4–7]. Thus, in a closed-line configuration, the role of a nonparaxial stabilizer may be played by a divertor [8, 9]. The objective of the present paper, which is dedicated to the memory of D.A. Panov, is to investigate the stability of a finite-pressure plasma in confinement systems with closed magnetic field lines (and with a zero rotational transform) by taking into account the effect of the plasma compressibility and by not restricting the analysis to a class of axisymmetric configurations of the poloidal magnetic field. Conditions for stability against perturbations localized near a magnetic field line (or ballooning modes, according to the terminology of [10]) are derived.[1]

2. We consider a localized perturbation with the displacement

$$\Xi = \xi(\mathbf{r}) \exp(iS - i\omega t), \quad (4)$$

[1] In contrast to axisymmetric configurations [2], the fact that, for general magnetic geometries, stability against such localized modes is a sufficient condition for stability against arbitrary perturbations remains unproved (see also [11]).

1063-780X/02/2809-0776$22.00 © 2002 MAIK "Nauka/Interperiodica"

where

$$\nabla S = \mathbf{k}_\perp, \quad \mathbf{k}_\perp \cdot \mathbf{B} = 0, \quad \mathbf{k}_\perp \cdot \boldsymbol{\xi} = 0,$$
$$\mathbf{B} \cdot \nabla \frac{\mathbf{k}_\perp \cdot \nabla a}{|\nabla a|^2} = 0, \quad \mathbf{B} \cdot \nabla \left(\frac{\mathbf{B} \times \nabla a}{B^2} \cdot \mathbf{k}_\perp \right) = 0, \quad (5)$$
$$k_\perp \gg b^{-1}, \quad \partial/\partial l;$$

b is the characteristic transverse dimension of the plasma, and $\partial/\partial l$ is the derivative along the magnetic field. For simplicity, we restrict ourselves to the case in which the "azimuthal" component $\mathbf{k}_\perp$ of the wave vector is much larger than its "radial" component. In this case, we have $\boldsymbol{\xi} = \sigma \frac{\nabla a}{|\nabla a|^2} + \tau \frac{\mathbf{B}}{B^2}$, and the displacement components σ and τ satisfy the equations [10]

$$-\frac{\rho\omega^2}{|\nabla a|^2}\sigma = \mathbf{B} \cdot \nabla \left(\frac{\mathbf{B}}{|\nabla a|^2} \cdot \nabla \sigma \right) + \frac{2\kappa}{|\nabla a|} \left[p'\sigma + \frac{\gamma p B^2}{\gamma p + B^2} \left(\nabla \cdot \left(\tau \frac{\mathbf{B}}{B^2} \right) - \frac{2\kappa}{|\nabla a|}\sigma \right) \right], \quad (6)$$

$$-\rho\omega^2\tau = \mathbf{B} \cdot \nabla \left[\frac{\gamma p B^2}{\gamma p + B^2} \left(\nabla \cdot \left(\tau \frac{\mathbf{B}}{B^2} \right) - \frac{2\kappa}{|\nabla a|}\sigma \right) \right], \quad (7)$$

where ρ is the density, a labels the magnetic surfaces (the constant pressure surfaces), $\oint \frac{dl}{B} = \text{const}$, $\kappa = \boldsymbol{\kappa} \cdot \nabla a / |\nabla a|$ is the normal component of the curvature vector $\boldsymbol{\kappa} = \nabla_\perp (p + B^2/2)/B^2$ of the magnetic field line, and the prime denotes the derivative with respect to a.

In formulas (6) and (7), the quantity

$$f = \frac{\gamma p B^2}{\gamma p + B^2} \left(\nabla \cdot \left(\tau \frac{\mathbf{B}}{B^2} \right) - \frac{2\kappa}{|\nabla a|}\sigma \right), \quad (8)$$

which is proportional to $\propto \nabla \cdot \boldsymbol{\xi}$, characterizes the displacement (see [10], Section 6). We express the derivative $\frac{\partial}{\partial l}\left(\frac{\tau}{B^2} \right)$ from formula (8) and integrate it along the magnetic field line (of length L). Then, taking into account the relationship

$$\tau(l + L) = \tau(l), \quad (9)$$

which holds for closed-line configurations, we obtain the following relationship for the function f:

$$\oint f \frac{\gamma p + B^2}{\gamma p B^2} \frac{dl}{B} = -\oint \frac{2\kappa\sigma}{|\nabla a|} \frac{dl}{B}. \quad (10)$$

From formula (7), we can see that, at the stability boundary $\omega^2 = 0$, the function f is independent of l and is equal to

$$f_0 = -\left(\oint \frac{\gamma p + B^2}{\gamma p B^2} \frac{dl}{B} \right)^{-1} \oint \frac{2\kappa\sigma}{|\nabla a|} \frac{dl}{B}. \quad (11)$$

In this case, the normal component σ of the displacement satisfies the integrodifferential equation

$$\frac{\partial}{\partial l}\left(\frac{B}{|\nabla a|^2} \frac{\partial}{\partial l}\sigma \right) + \frac{2\kappa p'}{B|\nabla a|}\sigma = -\frac{2\kappa}{B|\nabla a|} f_0. \quad (12)$$

The integral term on the right-hand side of this equation describes the effect of the plasma compressibility. For an axisymmetric configuration of the poloidal magnetic field, Eq. (12) passes over to Eq. (6.28) from [2].

We integrate Eq. (12) along the field line. Taking into account expression (11), we obtain

$$f_0 p' \oint \frac{\gamma p + B^2}{\gamma p B^2} \frac{dl}{B} = f_0 \oint \frac{2\kappa}{|\nabla a|} \frac{dl}{B}. \quad (13)$$

Assuming that $f_0 \neq 0$, we arrive at the equation

$$p' \oint \frac{\gamma p + B^2}{\gamma p B^2} \frac{dl}{B} = f_0 \oint \frac{2\kappa}{|\nabla a|} \frac{dl}{B}. \quad (14)$$

The relationships $\kappa = (p' + BB')\frac{|\nabla a|}{B^2}$ and $U' = -\oint \left(\frac{2B'}{B} + \frac{p'}{B^2} \right) \frac{dl}{B}$ put Eq. (14) in the form

$$\frac{p'}{p} + \gamma \frac{U'}{U} = 0, \quad (15)$$

which coincides with marginal stability condition (2). Hence, marginal stability is achieved at pressure profile (3). Note that Eq. (12) has the solution $\sigma = \text{const}$, which indicates that, at the stability boundary, the perturbation is of a flute nature. Moreover, the constancy of σ is a consequence of the plasma compressibility: for an incompressible perturbation ($f_0 = 0$), there is no such solution for $\beta \neq 0$.

It can be shown that, in accordance with [1], marginal stability condition (15) for a confinement system without a magnetic well is valid for an arbitrary relationship between the components of the wave vector $\mathbf{k}_\perp$ of localized perturbation (4).

3. Equations (6) and (7) may also have solutions with $\omega^2 < 0$ (i.e., solutions with $f = 0$, which are not of a flute nature) when $\frac{p'}{p} + \gamma \frac{U'}{U} > 0$. However, if one and

only one of the eigenvalues $\lambda_1 < \lambda_2 < \ldots$ of the problem

$$\frac{\partial}{\partial l}\left(\frac{B}{|\nabla a|^2}\frac{\partial}{\partial l}\sigma\right) + \left(\lambda r + \frac{2\kappa p'}{B|\nabla a|}\right)\sigma = 0, \quad (16)$$

$$\sigma(l + L) = \sigma(l) \quad (17)$$

(where $r(l)$ is a positive function[2]) is negative,

$$\lambda_1 < 0, \quad (18)$$

$$\lambda_2 > 0, \quad (19)$$

then Eqs. (6) and (7) have no such unstable solutions. The negative eigenvalue λ_1 corresponds to an unstable flute perturbation (the first eigenfunction $\sigma = \sigma_1$ has no zeros) in an incompressible plasma, i.e., to a confinement system without average minimum-B. However, by integrating Eq. (16), we can see that the constant sign of σ_1 yields the inequality $\lambda_1 \neq 0$ for $\oint \frac{\kappa\sigma}{|\nabla a|}\frac{dl}{B} \neq 0$. Consequently, according to relationship (10), the function f cannot be identically zero; i.e., there exists no solution with $f = 0$.[3] However, as was shown above, a compressible flute perturbation is stable. The inequality in condition (19) indicates the absence of unstable incompressible modes such that the displacement as a function of the coordinate along the field line has zeros. Condition (19) is valid for moderate pressures; the critical pressure at the given magnetic field line is $\beta = \beta_*$, at which the eigenvalue λ_2 passes through zero.

4. Hence, it has been shown that, in a confinement system without a magnetic well, the marginal stability against perturbations of class (4) is achieved at pressure profile (3) provided that β is lower than a certain critical value above which an unstable incompressible perturbation with an alternating-sign displacement $\sigma(l)$ appears at some magnetic field line. Since condition (1) refers to any β value, it may be said that the flute mode is the most dangerous.

Note that, under condition (1), the most "dangerous" (from the standpoint of the lowest possible pressure) magnetic field lines are those lying on a magnetic surface at which the pressure gradient is large and the magnetic field in regions of unfavorable field line curvature is weak (in a magnetic confinement system with a divertor, these are magnetic field lines near the separatrix surface).

[2] Since we are interested exclusively in the signs of the eigenvalues, the form of this function is unimportant for further analysis.

[3] For a flute perturbation, the function f equals zero at $\lambda_1 = 0$, in which case Eq. (13) at the stability boundary is automatically valid because both its sides contain $f_0 = 0$. The requirement $\lambda_1 \geq 0$ is reflected in the stability criteria for a closed-line confinement system with a magnetic well (see [11–14]).

ACKNOWLEDGMENTS

I am grateful to V.I. Il'gisonis for useful remarks. This study was supported in part by the Russian Federal Program "Leading Scientific Schools," project no. 00-15-96526.

REFERENCES

1. B. B. Kadomtsev, *Plasma Physics and the Problem of Controlled Thermonuclear Reactions* (Akad. Nauk SSSR, Moscow, 1958; Pergamon, New York, 1960), Vol. IV.
2. A. B. Bernstein, E. A. Frieman, M. D. Kruskal, and R. M. Kulsrud, Proc. R. Soc. London A **244**, 17 (1958).
3. A. N. Simakov, P. J. Catto, S. I. Krasheninnikov, and J. J. Ramos, Phys. Plasmas **7**, 2526 (2000).
4. L. S. Hall and B. McNamara, Phys. Fluids **18**, 552 (1975).
5. D. A. Panov, Pis'ma Zh. Éksp. Teor. Fiz. **35**, 70 (1982) [JETP Lett. **35**, 82 (1982)]; Fiz. Plazmy **9**, 184 (1983) [Sov. J. Plasma Phys. **9**, 112 (1983)].
6. J. Nuehrenberg and R. Zille, Phys. Lett. **129**, 113 (1988).
7. A. A. Skovoroda and V. D. Shafranov, Fiz. Plazmy **21**, 937 (1995) [Plasma Phys. Rep. **21**, 886 (1995)].
8. V. P. Pastukhov and A. Yu. Sokolov, Fiz. Plazmy **17**, 1043 (1991) [Sov. J. Plasma Phys. **17**, 603 (1991)].
9. V. V. Arsenin, E. D. Dlougach, V. M. Kulygin, *et al.*, Nucl. Fusion **41**, 945 (2001).
10. V. D. Pustovitov and V. D. Shafranov, in *Reviews of Plasma Physics*, Ed. by B. B. Kadomtsev (Énergoatomizdat, Moscow, 1987; Consultants Bureau, New York, 1990), Vol. 15.
11. G. O. Spies, Phys. Fluids **17**, 400 (1974).
12. L. S. Solov'ev, Zh. Éksp. Teor. Fiz. **53**, 2063 (1967) [Sov. Phys. JETP **26**, 1167 (1968)].
13. A. B. Mikhailovskiĭ, Zh. Éksp. Teor. Fiz. **64**, 536 (1973) [Sov. Phys. JETP **37**, 274 (1973)].
14. A. V. Frolenkov, Fiz. Plazmy **2**, 679 (1976) [Sov. J. Plasma Phys. **2**, 373 (1976)].

Translated by O. E. Khadin

Plasma Physics Reports, Vol. 28, No. 9, 2002, pp. 779–786. Translated from Fizika Plazmy, Vol. 28, No. 9, 2002, pp. 846–853.
Original Russian Text Copyright © 2002 by Ilgisonis, Khalzov.

TOKAMAKS

On the Boundary of an Equilibrium Plasma near the Magnetic Separatrix in a Tokamak[1]

V. I. Ilgisonis and I. V. Khalzov

Institute of Nuclear Fusion, Russian Research Centre Kurchatov Institute, pl. Kurchatova 1, Moscow, Russia

Received December 27, 2001

Abstract—It is shown that plasma rotation near the tokamak the wall can result in a shift of the isobaric separatrix with respect to the magnetic one. This shift is calculated analytically, and this effect is exemplified by simple plasma equilibrium states. The plasma rotation that causes the shift of the separatrices can be driven either by a nonzero radial electric field at the plasma edge or by the Hall effect, which may take place even in the absence of the electric field. © *2002 MAIK "Nauka/Interperiodica".*

1. INTRODUCTION

In the traditional theory of a high-temperature plasma equilibrium, the separatrix that separates nested toroidal magnetic surfaces from open field lines (which is characteristic of present-day tokamaks with a divertor) is regarded as a boundary of the "hot" plasma. This can be explained by simple kinetic considerations, according to which the plasma particles move roughly along the magnetic surfaces. Under the same considerations, the appearance of the separatrix restricts the maximum possible plasma pressure in a tokamak with a limiter [1]. In fact, it is well known that the drift orbits of charged particles in a tokamak may significantly deviate from the magnetic surfaces. Nevertheless, in static equilibrium, the plasma pressure is a function of the magnetic surface, so that the isobars can deviate from the projections of the magnetic surfaces onto the cross section of the plasma column only when the plasma exhibits a macroscopic motion (rotation).

In a rotating equilibrium plasma, the isobaric surfaces are known to deviate from the magnetic surfaces (see, e.g., [2–4]). On the other hand, it has been established experimentally that, in the immediate vicinity of the magnetic separatrix, the plasma pressure may be finite and the plasma rotation velocity may be nonzero (see, e.g., [5]); as a result, the boundary of the hot plasma and the magnetic separatrix may, in principle, be not coincident. To the best of our knowledge, this circumstance has not yet been extensively discussed in the literature, although it is clearly important to take it into account to correctly calculate equilibrium configurations, to infer true conclusions about the limiting values of the equilibrium plasma parameters, etc.

Rotation of the tokamak edge plasma is, as a rule, driven by a nonzero electric field near the wall. This electric field can be associated with different effects, e.g., dominant loss of suprathermal ions, which have "wider" orbits in the wall region [6], and distinctive features of the boundary conditions in the divertor layer of a tokamak (with allowance for the longitudinal ion fluxes onto the divertor plates) [7, 8]. However, even in the idealized case of a high longitudinal conductivity of the plasma in the divertor layer (i.e., of a constant electric potential outside the separatrix), the plasma ions can undergo rotational motion (this possible rotation is described by multifluid MHD models).

Here, we analyze the possible difference between the magnetic and isobaric separatrices due to plasma edge rotation. Depending on the relationships between the equilibrium plasma parameters, the separatrix that separates nested isobaric surfaces from unclosed isobars and is regarded as a physical boundary of the confined hot plasma can lie either inside (an unfavorable case) or outside (a favorable case) the magnetic separatrix. The analysis is carried out on the basis of the Hall magnetohydrodynamics (HMHD) model, which is one of the simplest two-fluid models [9] suitable for describing the steady states of a moving plasma [9–11]. Simple analytic examples of equilibria are presented that demonstrate the effect of different spatial positions of the magnetic and isobaric separatrices.

2. AXISYMMETRIC PLASMA EQUILIBRIUM

Using the HMHD model, we consider the simplest case of an equilibrium tokamak plasma rotating only in the toroidal direction. We employ a cylindrical coordinate system $\{r, \zeta, z\}$, where the radial coordinate r is measured from the z-axis, which is the symmetry axis of the torus, and ζ is the toroidal angular coordinate (the axial symmetry of the tokamak implies that $\partial_\zeta \longrightarrow 0$).

[1] This paper is devoted to the memory of Dmitriĭ Aleksandrovich Panov, a highly skilled physicist and charming man.

1063-780X/02/2809-0779$22.00 © 2002 MAIK "Nauka/Interperiodica"

For a steady-state plasma ($\partial_t \longrightarrow 0$), the set of HMHD equations has the following form (see, e.g., [11]):

$$\rho\nabla\frac{\mathbf{v}^2}{2} + \rho(\nabla\times\mathbf{v})\times\mathbf{v} + \nabla p + \frac{1}{4\pi}\mathbf{B}\times(\nabla\times\mathbf{B}) = 0, \quad (1)$$

$$\nabla\times(\mathbf{v}_e\times\mathbf{B}) = 0, \quad (2)$$

$$\mathbf{v}_e = \mathbf{v} - \frac{\varepsilon}{4\pi\rho}\nabla\times\mathbf{B}, \quad \varepsilon = \frac{m_i c}{e}, \quad (3)$$

$$\nabla\cdot(\rho\mathbf{v}) = 0. \quad (4)$$

Here, we use the standard notation: $\mathbf{v}$ is the flow velocity of the ions of mass m_i; $\mathbf{v}_e$ is the electron flow velocity; and the quantity ε accounts for the Hall effect, which results from the two-fluid nature of the plasma (in the limit $\varepsilon \longrightarrow 0$, the HMHD equations are reduced to the conventional one-fluid MHD equations). Equation (2) can be integrated by introducing the electric potential ϕ:

$$\mathbf{v}_e\times\mathbf{B} = c\nabla\phi, \quad (5)$$

which yields the relationship $\mathbf{B}\nabla\phi = 0$, indicating that ϕ is a function of the magnetic surface,

$$\phi = \phi(\Psi), \quad (6)$$

where Ψ is the label of the magnetic surface described by the equation $\Psi(r, z) = \text{const}$.

We represent the magnetic field as

$$\mathbf{B} = \nabla\Psi\times\nabla\zeta + I\nabla\zeta, \quad (7)$$

where the magnetic surface label Ψ is chosen to be the normalized poloidal magnetic flux. The toroidal plasma rotation velocity can be written in the form

$$\mathbf{v} = \Omega(r, z)r^2\nabla\zeta, \quad (8)$$

which satisfies Eq. (4) by virtue of the axial symmetry of the problem.

Substituting expressions (7) and (8) into Eq. (1) yields

$$-\rho\Omega^2 r\nabla r + \nabla p + \frac{1}{4\pi}\left(\frac{1}{r^2}\Delta^*\Psi\nabla\Psi + \frac{I}{r^2}\nabla I - (\nabla\zeta\cdot[\nabla I\times\nabla\Psi])\nabla\zeta\right) = 0, \quad (9)$$

where

$$\Delta^* = r\frac{\partial}{\partial r}\left(\frac{1}{r}\frac{\partial}{\partial r}\right) + \frac{\partial^2}{\partial z^2}.$$

The vector equation (9) is equivalent to the three scalar equations

$$\Delta^*\Psi + II' + 4\pi r^2(\partial_\Psi p)_r = 0, \quad (10)$$

$$I = I(\Psi), \quad (11)$$

$$\left(\frac{\partial p}{\partial r}\right)_\Psi = \rho\Omega^2 r. \quad (12)$$

Equation (10) is the Grad–Shafranov equation in which the total derivative of the pressure with respect to Ψ is replaced by the partial derivative with respect to Ψ at constant r. The quantity Ω has the meaning of the angular frequency of the toroidal rotation of the ions. Equation (12) clearly shows that, for a nonzero rotation frequency ($\Omega \neq 0$), the plasma pressure is no longer a function of the magnetic surface; i.e., we have $p = p(\Psi, r)$.

From Eqs. (5) and (3), we obtain the following relationship between Ω and $(\partial_\Psi p)_r$:

$$\Omega = \omega(\Psi) + \frac{\varepsilon}{\rho}(\partial_\Psi p)_r, \quad (13)$$

where, for convenience, we have introduced the function $\omega(\Psi) = c\phi'(\Psi)$, which determines the electric field (here and below, the prime denotes the derivative with respect to Ψ). In the absence of the Hall effect ($\varepsilon \longrightarrow 0$), the quantities Ω and ω coincide. When the Hall effect is taken into account, the actual angular rotation frequency Ω differs from the derivative of the electric potential ($\omega = c\phi'$).

3. PATTERN OF ISOBARS NEAR THE MAGNETIC SEPARATRIX

We consider the condition for the existence of a separatrix in the cross section of the family of magnetic surfaces $\Psi(r, z) = \text{const}$. We do not specify the function Ψ but assume that it is a solution to Grad–Shafranov equation (10). The singular points of the family of magnetic surfaces should satisfy the vector equation $\nabla\Psi = 0$. Taking into account representation (7), we see that this equation is equivalent to the following two scalar equations:

$$\left(\frac{\partial\Psi}{\partial r}\right)_z = rB_z = 0, \quad \left(\frac{\partial\Psi}{\partial z}\right)_r = -rB_r = 0. \quad (14)$$

The nested magnetic surfaces have at least one singular point—the magnetic axis ($r = R$, $z = 0$). For simplicity, we also assume that, in the cross section of the magnetic surfaces, there is a vertical separatrix with the radius $r = r_s$, at which we have $B_r = 0$. Under this assumption, substituting $r = r_s$ into the first of Eqs. (14) allows us to find the z coordinate Z_m of the X-point at the magnetic separatrix.

Analogously, taking into account Eq. (12), we obtain the following equations for the isobaric surfaces $p(r, z) = \text{const}$:

$$\left(\frac{\partial p}{\partial r}\right)_z = \left(\frac{\partial p}{\partial \Psi}\right)_r\left(\frac{\partial \Psi}{\partial r}\right)_z + \left(\frac{\partial p}{\partial r}\right)_\Psi$$

$$= rB_z\left(\frac{\partial p}{\partial \Psi}\right)_r + r\rho\Omega^2 = 0, \quad (15)$$

$$\left(\frac{\partial p}{\partial z}\right)_r = \left(\frac{\partial p}{\partial \Psi}\right)_r\left(\frac{\partial \Psi}{\partial z}\right)_r = -rB_r\left(\frac{\partial p}{\partial \Psi}\right)_r = 0.$$

We can see that the family of isobaric surfaces also possesses a vertical separatrix with $r = r_s$, but the ordinate Z_p of the isobaric X-point for $\Omega \neq 0$ can differ from the ordinate of the magnetic X-point.

Let us determine the relative shift of the isobaric and magnetic X-points. To do this, we can retain only the lowest order term in the expansion of B_z in powers of z at $r = r_s$,

$$B_{zs} \approx B_{z0} + \frac{1}{2}\left(\frac{\partial^2 B_{zs}}{\partial z^2}\right)\bigg|_{z=0} z^2, \quad (16)$$

because, for an up/down symmetric plasma configuration, we have $(\partial_z B_{zs})|_{z=0} = 0$. Here and below, the subscript s refers to the values of the quantities at the vertical separatrix, i.e., at $r = r_s$. Inserting expansion (16) for B_{zs} into the first of Eqs. (14), we obtain

$$\left(\frac{\partial^2 B_{zs}}{\partial z^2}\right)\bigg|_{z=0} \approx -\frac{2B_{z0}}{Z_m^2}. \quad (17)$$

With allowance for relationships (16) and (17), the first of Eqs. (15) gives

$$B_{z0}\left(1 - \frac{Z_p^2}{Z_m^2}\right)\left(\frac{\partial p}{\partial \Psi}\right)_r\bigg|_s + \rho_s\Omega_s^2 \approx 0. \quad (18)$$

We introduce the relative shift of the isobaric and magnetic X-points,

$$\delta = \frac{Z_p - Z_m}{Z_m}, \quad (19)$$

to rewrite Eq. (18) in the form

$$1 - (1+\delta)^2 + \frac{\rho_s\Omega_s^2}{B_{z0}(\partial p/\partial \Psi)_r|_s} \approx 0. \quad (20)$$

Assuming that $|\delta| \lesssim 1$, we obtain from Eq. (20)

$$\delta \approx \frac{\rho_s\Omega_s^2}{2B_{z0}(\partial p/\partial \Psi)_r|_s}. \quad (21)$$

When the electric field vanishes at the magnetic separatrix ($\omega_s = 0$), the plasma rotation in the separatrix region is associated with the two-fluid nature of the plasma [see Eq. (13)]:

$$\Omega_s = \frac{\varepsilon}{\rho_s}\left(\frac{\partial p}{\partial \Psi}\right)_r\bigg|_s. \quad (22)$$

Substituting the quantity $(\partial p/\partial \Psi)_r|_s$ extracted from formula (22) into relationship (21), we obtain the relative shift of the isobaric and magnetic X-points:

$$\delta \approx \frac{\varepsilon\Omega_s}{2B_{z0}} = \frac{\Omega_s}{2\omega_{B_{pi}}}, \quad \omega_{B_{pi}} = \frac{eB_{z0}}{m_i c}; \quad (23)$$

where $\omega_{B_{pi}}$ is the ion cyclotron frequency in the poloidal magnetic field B_{z0}. Expression (23) clearly shows that, even when the electric field at the magnetic separatrix is zero, the plasma rotation ($\Omega_s \neq 0$) leads to the relative shift of the magnetic and isobaric X-points (and, accordingly, of the magnetic and isobaric separatrices in the vicinity of the X-points). The value of the shift is determined by the ratio of the angular frequency of the toroidal plasma rotation to the ion cyclotron frequency in the poloidal magnetic field. The sign of the shift depends on the signs of the quantities Ω_s and B_{z0}, i.e., on the mutual orientation of the toroidal rotation velocity vector $\mathbf{v}$ and the z-component $B_{z0}\nabla z$ of the magnetic field. When $\delta > 0$, the isobaric surface, which coincides with the boundary of the plasma column, is shifted to the region outside the magnetic separatrix; as a result, the plasma pressure at the magnetic separatrix (at least, near the magnetic X-point) is nonzero. When $\delta < 0$, the isobaric surface is shifted to the region inside the magnetic separatrix, in which case the plasma pressure at the magnetic separatrix is, of course, zero.

However, if the plasma conductivity in the separatrix region is low, then the electric field at the separatrix can be nonzero, as is the case, e.g., in a detached plasma. In this situation, the relative shift of the isobaric and magnetic X-points is no longer governed exclusively by the two-fluid effects.

The relative shift can be estimated from the following considerations. The plasma pressure at the magnetic axis $\{r = R, z = 0\}$ can be approximately represented as

$$p_a \approx p_s + \left(\frac{\partial p}{\partial r}\right)_{z=0}\bigg|_s \epsilon R + o(\epsilon), \quad (24)$$

where $\epsilon = (R - r_s)/R$ ($|\epsilon| < 1$) is the inverse aspect ratio. Since the pressure at the vertical separatrix is zero ($p_s = 0$), we have

$$\frac{p_a}{\epsilon R} \approx \left(\frac{\partial p}{\partial r}\right)_{z=0}\bigg|_s = r_s\left(\rho_s\Omega_s^2 + B_{z0}\left(\frac{\partial p}{\partial \Psi}\right)_r\bigg|_s\right). \quad (25)$$

When the kinetic energy $\rho\Omega^2R^2/2$ of the plasma rotation is insignificant in comparison with the pressure p_a, we

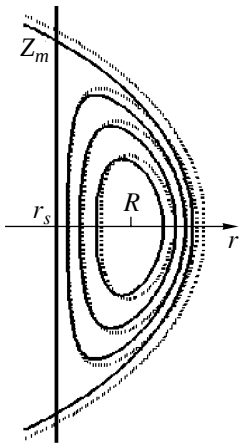

Fig. 1. Magnetic (solid curves) and isobaric (dotted curves) surfaces in an equilibrium configuration described by expressions (34) and (36) with $\epsilon = (R - r_s)/R = 0.2$, $Z_m = 0.5R$, and $M_a^2 = 0.49$.

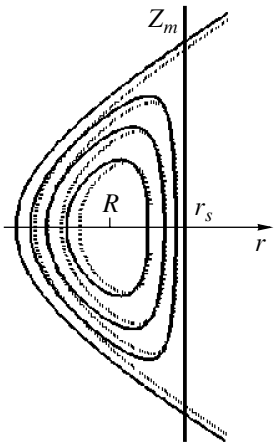

Fig. 2. Magnetic (solid curves) and isobaric (dotted curves) surfaces in an equilibrium configuration described by expressions (34) and (36) with $\epsilon = (R - r_s)/R = -0.2$, $Z_m = 0.5R$, and $M_a^2 = 0.49$.

can extract the quantity $(\partial p/\partial\Psi)_r|_s$ from Eq. (25):

$$\left(\frac{\partial p}{\partial \Psi}\right)_r\Bigg|_s \approx \frac{p_a}{\epsilon R^2 B_{z0}}.$$

We insert this expression into relationship (21) to obtain the relative shift of the isobaric and magnetic X-points:

$$\delta \approx \epsilon \frac{\rho_s \Omega_s^2 R^2}{2 p_a}. \tag{26}$$

Hence, when the electric field in the separatrix region is nonzero, the relative shift of the isobaric and magnetic X-points is determined by the toroidal rotation velocity of the plasma at the separatrix. The sign of this shift depends on the sign of ϵ, i.e., on the relative position of the vertical separatrix to the magnetic axis. For a D-shaped cross section of the plasma column, the inverse aspect ratio is positive, $\epsilon > 0$, and the vertical separatrix occurs at the inner circumference of the torus. The isobaric surface is shifted to the region outside the magnetic separatrix, so that the plasma pressure at the magnetic separatrix (at least, near the magnetic X-point) is nonzero (Fig. 1). When $\epsilon < 0$, the vertical separatrix is at the outer circumference of the torus and the plasma pressure at the magnetic separatrix is zero (Fig. 2).

4. ANALYTIC EXAMPLES OF PLASMA EQUILIBRIA

We illustrate the above analysis by discussing simple analytic examples of equilibrium plasma states. In contrast to the static plasma state, in which the plasma equilibrium is described by the two flux-surface functions $I(\Psi)$ and $p(\Psi)$, a description of the toroidally rotating plasma requires the specification of two additional functions, $\omega(\Psi)$ and $\rho(\Psi, r)$, in which case the plasma pressure $p(\Psi, r)$ should satisfy Eq. (12).

In order to find analytic solutions to Eqs. (10) and (12), we represent the plasma density ρ as $\rho = \rho_0(r) f(\Psi)$, use expression $I^2 = 2C_I\Psi + C_*$, and assume that $(\partial p/\partial\Psi)_r$ is a function of only r. Then, Eq. (12) can be integrated to yield (see Appendix)

$$p(\Psi, r) = \frac{p_a}{1-\kappa}\Bigg[\exp\left(M_a^2(1-\kappa)\frac{r^2 - R^2}{R^2}\right)\frac{\Psi}{\Psi_a} + \kappa\exp\left(M_a^2(1-\kappa)\frac{r^2 - r_s^2}{R^2}\right)\left(1 - \frac{\Psi}{\Psi_a}\right) - \kappa\Bigg], \tag{27}$$

where the label Ψ is measured from the magnetic separatrix (at which $\Psi = 0$), $M_a^2 = \rho_a \Omega_a^2 R^2/(2p_a)$ is the square of the Mach number, p_a is the pressure at the magnetic axis, and $\kappa = \rho_s \Omega_s^2/(\rho_a \Omega_a^2)$.

Using expression (27), we can rewrite Eq. (10) in the form

$$4r^2\frac{\partial^2\Psi}{\partial(r^2)^2} + \frac{\partial^2\Psi}{\partial z^2} + C_I + 4\pi r^2 \frac{p_a}{\Psi_a(1-\kappa)} \times\left[1 - \kappa\exp\left(M_a^2(1-\kappa)\frac{R^2 - r_s^2}{R^2}\right)\right] \times\exp\left(M_a^2(1-\kappa)\frac{r^2 - R^2}{R^2}\right) = 0. \tag{28}$$

The solution to this equation can be constructed by the expansion in polynomials in r and z^2 (see, e.g., [12]).

The simplest way to do this is to retain only the lowest order term in the expansion in powers of z^2 and to use explicitly the coordinates $\{r_s, Z_m\}$ of the magnetic X-point. Introducing the dimensionless variables $x = r/R$ and $y = z/R$, we can express $\Psi(x, y)$ as

$$\Psi(x, y) = \frac{B_{z0}R^2}{2}\left\{(x_s^2 - x^2)\frac{y^2}{y_m^2} + \frac{1}{4y_m^2}[(x^2-1)^2 - (x_s^2-1)^2] + \left(1 - \frac{x_s^2-1}{2y_m^2}\right)[1 - \exp[K(x_s^2-1)]]^{-1} \times \left(x^2 - x_s^2 - \frac{1}{K}[\exp[K(x^2-1)] - \exp[K(x_s^2-1)]]\right)\right\}, \quad (29)$$

where $x_s = r_s/R$, $y_m = Z_m/R$, and $K = M_a^2(1 - \kappa)$. The quantity B_{z0} is the z-component of the magnetic field at the vertical separatrix at $z = 0$. Indeed, we have

$$B_{zs}\big|_{z=0} = 2\left(\frac{\partial\Psi}{\partial(r^2)}\right)_{z=0}\Bigg|_{r=r_s} = \frac{2}{R^2}\left(\frac{\partial\Psi}{\partial(x^2)}\right)_{y=0}\Bigg|_{x=x_s} = B_{z0}. \quad (30)$$

Substituting expression (29) for $\Psi(x, y)$ into Grad–Shafranov equation (28), we obtain the relationship between the geometric parameters (x_s, y_m) of the magnetic configuration and the plasma parameters (M_a, κ, $\beta_0 = 8\pi p_a/B_{z0}^2$),

$$1 - \frac{x_s^2-1}{2y_m^2} = \frac{\beta_0}{4K(1-\kappa)\tilde{\Psi}_a} \times (1 - \kappa\exp[K(1-x_s^2)])(1 - \exp[K(x_s^2-1)]), \quad (31)$$

where

$$\tilde{\Psi}_a = \frac{\Psi(1,0)}{B_{z0}R^2} = \frac{1}{2}\left\{-\frac{(x_s^2-1)^2}{4y_m^2} + \left(1 - \frac{x_s^2-1}{2y_m^2}\right) \times \left((1 - \exp[K(x_s^2-1)])^{-1}(1-x_s^2) - \frac{1}{K}\right)\right\}, \quad (32)$$

and also the relationship between the magnetic-field component B_{z0} and the quantity C_I, characterizing the poloidal current profile,

$$C_I = -\frac{x_s^2}{y_m^2}B_{z0}. \quad (33)$$

In the simplest case $\kappa \longrightarrow 1$ ($\rho_s\Omega_s^2 \longrightarrow \rho_a\Omega_a^2$), expression (29) for $\Psi(x, y)$ reduces to

$$\Psi(x, y) = \frac{B_{z0}R^2}{2}\left((x_s^2 - x^2)\frac{y^2}{y_m^2} + \frac{1}{2(x_s^2-1)}[(x^2-1)^2 - (x_s^2-1)^2]\right), \quad (34)$$

which corresponds to the familiar Solov'ev's solution[1]; moreover, from relationship (31), it follows that

$$y_m^2 = \frac{x_s^2-1}{2(1-\beta_0)}. \quad (35)$$

Note that the surfaces Ψ = const of the function Ψ given by expression (34) are closed near the point $\{x = 1, y = 0\}$ at any $x_s \neq 1$, and the points $\{x = x_s, y = y_m\}$ are X-points. In what follows, we restrict ourselves to considering such values of M_a and κ that do not distort this configuration.

For $\kappa \longrightarrow 1$, expression (27) for the plasma pressure simplifies to

$$p(\Psi, x) = p_a\left[(1 + M_a^2(x_s^2-1))\frac{\Psi}{\Psi_a} + M_a^2(x^2 - x_s^2)\right], \quad (36)$$

where

$$\Psi_a = \frac{B_{z0}R^2}{4}(1 - x_s^2). \quad (37)$$

Knowing the equilibrium configuration of the magnetic field and the plasma parameters, we can determine the relative shift of the isobaric and magnetic X-points. For the solutions obtained above, specifically, the solutions that are linear in z^2, expansion (16) and Eq. (20) are exact. Consequently, in the case in which the electric field vanishes at the separatrix, the relative shift of the X-points is described by the expression [see Eq. (20)]

$$\delta = \sqrt{1 - \frac{\Omega_s}{\omega_{B_{pi}}}} - 1, \quad (38)$$

where $\omega_{B_{pi}} = eB_{z0}/m_i c$ is the ion cyclotron frequency in terms of the field component B_{z0}.

If the electric field at the separatrix is nonzero, then Eq. (20) at $\kappa \neq 1$ yields

$$1 - (1+\delta)^2 + 2\kappa M_a^2\tilde{\Psi}_a(1-\kappa)(\exp[K(x_s^2-1)] - \kappa)^{-1} = 0, \quad (39)$$

where $\tilde{\Psi}_a$ is given by expression (32).

For $\kappa \longrightarrow 1$, Eq. (39) reduces to

$$1 - (1 + \delta)^2 + \frac{(1 - x_s^2)M_a^2}{2(1 - (1 - x_s^2)M_a^2)} = 0. \quad (40)$$

Taking into account the relationship $x_s = 1 - \epsilon$, we obtain

$$\delta = \sqrt{1 + \frac{\epsilon(1 - \epsilon/2)M_a^2}{1 - 2\epsilon(1 - \epsilon/2)M_a^2}} - 1. \quad (41)$$

To within terms of first order in the expansion in powers of ϵ, expression (41) can be written as

$$\delta \approx \frac{\epsilon M_a^2}{2}.$$

For $\kappa = 1$ (i.e., for $\rho_s\Omega_s^2 = \rho_a\Omega_a^2$), this approximate expression coincides with estimate (26).

5. CONCLUSION

Using as an example simple analytic plasma equilibria in a tokamak, we have shown that toroidal rotation of the edge plasma can result in a shift of the plasma boundary with respect to the magnetic separatrix. In different magnetic configurations, the plasma boundary can occur either inside or outside (when the cross section of the plasma column is D-shaped) the magnetic separatrix; in the latter case, the plasma pressure at the magnetic separatrix is nonzero. We have calculated the shift of the isobaric X-point relative to the magnetic X-point as a function of the rotation velocity of the edge plasma. It can be expected that, for a D-shaped tokamak, poloidal plasma rotation will enhance the effect in question. The results obtained show that, in computing particular equilibrium configurations, it is necessary to formulate the boundary conditions more accurately.

ACKNOWLEDGMENTS

This work was supported in part by the Russian Foundation for Basic Research (project no. 02-02-16089) and the Russian Federal Program "Leading Scientific Schools" (project no. 00-15–96526).

APPENDIX

Here, we show that, under the assumptions made in our analysis, expression (27) leads to a general solution to Eq. (12). We rewrite Eq. (12) in the form

$$\left(\frac{\partial p}{\partial r^2}\right)_\Psi = \frac{\rho\Omega^2}{2} = \frac{\rho}{2}\left(\omega(\Psi) + \frac{\varepsilon}{\rho}\left(\frac{\partial p}{\partial \Psi}\right)_r\right)^2. \quad (42)$$

Representing the density as $\rho(\Psi, r) = \rho_0(r^2)f(\Psi)$ (where $\rho_0 \neq 0$) and assuming that the pressure is linear in Ψ, $p(\Psi, r) = C_p(r^2)\Psi + p_0(r^2)$, we obtain

$$\frac{\dot{C}_p}{\rho_0}\Psi + \frac{\dot{p}_0}{\rho_0} = \frac{f\omega^2}{2} + \varepsilon\omega\frac{C_p}{\rho_0} + \frac{\varepsilon^2}{2}f\frac{C_p^2}{\rho_0^2}. \quad (43)$$

Here and below, the superior dot indicates the derivative with respect to r^2, and the prime denote indicates the derivative with respect to Ψ. We differentiate this equation two times with respect to Ψ at constant r to obtain

$$0 = \frac{1}{2}(f\omega^2)'' + \varepsilon\omega''\frac{C_p}{\rho_0} + \frac{\varepsilon^2}{2}\left(\frac{1}{f}\right)''\left(\frac{C_p}{\rho_0}\right)^2. \quad (44)$$

Then, we differentiate Eq. (44) with respect to r^2 at constant Ψ,

$$0 = \varepsilon\omega''\left(\frac{C_p}{\rho_0}\right)^{\cdot} + \varepsilon^2\left(\frac{1}{f}\right)''\left(\frac{C_p}{\rho_0}\right)\left(\frac{C_p}{\rho_0}\right)^{\cdot}. \quad (45)$$

Equation (45) imposes restrictions on the function $\omega(\Psi)$, $f(\Psi)$, $C_p(r^2)$, and $\rho_0(r^2)$. For $\varepsilon \neq 0$, this equation splits into the following two conditions:

$$\omega'' + \varepsilon\left(\frac{1}{f}\right)''\left(\frac{C_p}{\rho_0}\right) = 0 \quad \text{or} \quad \left(\frac{C_p}{\rho_0}\right)^{\cdot} = 0.$$

Let us analyze these conditions separately.

(i) Noting that $C_p/\rho_0 \neq \text{const}$, we obtain from the first equation $\omega'' + \varepsilon(1/f)''(C_p/\rho_0) = 0$ the relationships

$$\omega = C_\omega\Psi + \omega_0, \quad f = \frac{1}{\lambda\Psi + \mu}.$$

Equation (44) yields the following relationships between the constants C_ω, ω_0, λ, and μ: $C_\omega = \chi\lambda$ and $\omega_0 = \chi\mu$ (where χ is an arbitrary constant), in which case we obtain

$$\omega = \chi(\lambda\Psi + \mu), \quad f = \frac{1}{\lambda\Psi + \mu}.$$

However, this solution is not satisfactory for the following reason. If the electric field vanishes at the separatrix, then we have $\omega_s = 0$, which holds either when $\chi = 0$ or when $\lambda\Psi_s + \mu = 0$. In the first case, the electric field is identically zero everywhere ($\omega \equiv 0$). In the second case, the plasma density at the separatrix is singular.

(ii) For $C_p/\rho_0 = C = \text{const} \neq 0$, Eq. (43) implies that $\dot{C}_p/\rho_0 = C_1 = \text{const}$, $\dot{p}_0/\rho_0 = C_2 = \text{const}$, and

$$C_1\Psi + C_2 = \frac{f}{2}\left(\omega + \frac{\varepsilon C}{f}\right)^2.$$

If the dependence $f(\Psi)$ is known, then, from these three relationships, we can find the functions $\rho_0(r)$, $C_p(r)$, $p_0(r)$, and $\omega(\Psi)$:

$$\rho_0(r) = \rho_{00}\exp(kr^2), \quad C_p(r) = C\rho_{00}\exp(kr^2),$$

$$p_0 = \frac{C_2\rho_{00}}{k}\exp(kr^2) + p_{00},$$

$$\omega(\Psi) = \pm\sqrt{\frac{2(kC\Psi + C_2)}{f(\Psi)}} - \frac{\varepsilon C}{f(\Psi)},$$

$$\Omega(\Psi) = \pm\sqrt{\frac{2(kC\Psi + C_2)}{f(\Psi)}}.$$

We thus see that the angular rotation frequency is a function of the magnetic surface: $k = C_1/C$.

Now, we clarify the physical meaning of the constants introduced above. We assume that $\Psi = 0$ and $f(0) = f_s$ at the magnetic separatrix and that $\Psi = \Psi_a$ and $f(\Psi_a) = 1$ at the magnetic axis. Since, at the vertical isobaric separatrix (which coincides with the magnetic separatrix), the plasma pressure should vanish, we have $p_0|_{r = r_s} = 0$ at $r = r_s$, so that the function $p_0(r)$ has the form

$$p_0 = \frac{C_2\rho_{00}}{k}[\exp(kr^2) - \exp(kr_s^2)]. \quad (46)$$

At the magnetic axis, the plasma density is $\rho_a = \rho_{00}\exp(kR^2)$, which gives

$$\rho_{00} = \rho_a\exp(-kR^2). \quad (47)$$

At the vertical separatrix, we have $\rho_s = \rho_a\exp(k(r_s^2 - R^2))f_s$, or, equivalently,

$$f_s = \frac{\rho_s}{\rho_a}\exp(k(R^2 - r_s^2)). \quad (48)$$

The angular rotation frequency at the magnetic separatrix is equal to $\Omega_s = \pm(2C_2/f_s)^{1/2}$, which allows us to find C_2:

$$C_2 = \frac{f_s\Omega_s^2}{2} = \frac{\rho_s\Omega_s^2}{2\rho_a}\exp(k(R^2 - r_s^2)). \quad (49)$$

From expressions (46), (47), and (49), we obtain the following expressions for the pressure and angular rotation frequency at the magnetic axis:

$$p_a = C\rho_a\Psi_a + \frac{\rho_s\Omega_s^2}{2k}(\exp(k(R^2 - r_s^2)) - 1),$$
$$\Omega_a^2 = 2\left(kC\Psi_a + \frac{\rho_s\Omega_s^2}{2\rho_a}\exp(k(R^2 - r_s^2))\right). \quad (50)$$

Resolving these expressions in the unknowns k and C, we find

$$k = \frac{\rho_a\Omega_a^2 - \rho_s\Omega_s^2}{2p_a} = \frac{M_a^2}{R^2}(1 - \kappa), \quad (51)$$

$$C = \frac{p_a}{\rho_a\Psi_a(1 - \kappa)}\left(1 - \kappa\exp\left(M_a^2(1 - \kappa)\frac{R^2 - r_s^2}{R^2}\right)\right), \quad (52)$$

where $M_a^2 = \rho_a\Omega_a^2R^2/(2p_a)$ is the square of the Mach number at the magnetic axis and $\kappa = \rho_s\Omega_s^2/(\rho_a\Omega_a^2)$.

Hence, taking into account expressions (46)–(52), we can represent the solution to Eq. (43) in the form

$$\rho(\Psi, r) = \rho_a\exp\left(M_a^2(1 - \kappa)\frac{r^2 - R^2}{R^2}\right)f(\Psi),$$

$$p(\Psi, r) = \frac{p_a}{1 - \kappa}\left[\exp\left(M_a^2(1 - \kappa)\frac{r^2 - R^2}{R^2}\right)\frac{\Psi}{\Psi_a}\right.$$
$$\left. + \kappa\exp\left(M_a^2(1 - \kappa)\frac{r^2 - r_s^2}{R^2}\right)\left(1 - \frac{\Psi}{\Psi_a}\right) - \kappa\right],$$

$$\Omega(\Psi) = \Omega_a\sqrt{\frac{1}{f(\Psi)}\left[\frac{\Psi}{\Psi_a} + \kappa\exp\left(M_a^2(1 - \kappa)\frac{R^2 - r_s^2}{R^2}\right)\left(1 - \frac{\Psi}{\Psi_a}\right)\right]},$$

$$\omega(\Psi) = \Omega(\Psi) - \frac{\varepsilon p_a}{\rho_a\Psi_a f(\Psi)(1 - \kappa)}$$
$$\times\left(1 - \kappa\exp\left(M_a^2(1 - \kappa)\frac{R^2 - r_s^2}{R^2}\right)\right).$$

In deriving this solution, we used the following free parameters: the density ρ_a; the pressure p_a; the Mach number M_a at the magnetic axis; and the dimensionless quantity κ, which characterizes the separatrix region and the relative position r_s/R of the vertical separatrix. The function $\Psi(r, z)$ was assumed to be known. The function $f(\Psi)$ was an arbitrary nonnegative function that determines the plasma density profile and satisfies the boundary conditions $f(\Psi_a) = 1$ and $f(0) = f_s$, where the function f_s is given by expression (48).

REFERENCES

1. L. S. Solov'ev, in *Reviews of Plasma Physics*, Ed. by M. A. Leontovich (Atomizdat, Moscow, 1972; Consultants Bureau, New York, 1975), Vol. 6.
2. E. K. Maschke and H. Perrin, Plasma Phys. **22**, 579 (1980).

3. E. Hameiri, Phys. Fluids **26**, 230 (1983).
4. H. Tasso and G. N. Throumoulopous, Phys. Plasmas **5**, 2378 (1998).
5. M. J. Schaffer, B. D. Bray, J. A. Boedo, *et al.*, Phys. Plasmas **8**, 2118 (2001).
6. P. N. Yushmanov, J. Q. Dong, W. Horton, and X. N. Su, Phys. Plasmas **1**, 1583 (1994).
7. R. H. Cohen and D. D. Ryutov, Comments Plasma Phys. Control. Fusion **16**, 255 (1995).
8. T. D. Rognlien, D. D. Ryutov, N. Matter, and G. D. Porter, Phys. Plasmas **6**, 1851 (1999).
9. A. I. Morozov and L. S. Solov'ev, in *Reviews of Plasma Physics*, Ed. by M. A. Leontovich (Atomizdat, Moscow, 1974; Consultants Bureau, New York, 1980), Vol. 8.
10. L. C. Steinhauer, Phys. Plasmas **6**, 2734 (1999).
11. V. I. Ilgisonis, Plasma Phys. Controlled Fusion **43**, 1255 (2001).
12. L. S. Solov'ev and V. D. Shafranov, in *Reviews of Plasma Physics*, Ed. by M. A. Leontovich (Atomizdat, Moscow, 1967; Consultants Bureau, New York, 1970), Vol. 5.

Translated by O. E. Khadin

Plasma Physics Reports, Vol. 28, No. 9, 2002, pp. 787–789. Translated from Fizika Plazmy, Vol. 28, No. 9, 2002, pp. 854–857.
Original Russian Text Copyright © 2002 by Khvesyuk, Chirkov, Kovalev.

TURBULENCE AND CHAOS

Some Features of the Stochastic Particle Dynamics in a Magnetized Plasma

V. I. Khvesyuk, A. Yu. Chirkov, and A. V. Kovalev

Bauman State Technical University, Vtoraya Baumanskaya ul. 5, Moscow, 107005 Russia

Received March 21, 2002

Abstract—A study is made of the dynamics of particles interacting with electromagnetic field fluctuations in a plasma in the presence of a magnetic field. Possible mechanisms for the onset of anomalous transport and its suppression by applying a radial electrostatic field are analyzed. Estimates of the diffusion coefficient are proposed based on the calculations of particle trajectories. © *2002 MAIK "Nauka/Interperiodica".*

The paper is devoted to analyzing the dynamics of charged particles in an inhomogeneous magnetized plasma in their interactions with wave packets propagating transverse to the magnetic field and to the plasma density gradient. This approach makes it possible to consider the processes of particle scattering by electromagnetic field fluctuations. Similar problems arise in the study of anomalous transport in plasmas (see, e.g., [1–6] and other related papers).

Here, a possible mechanism for the onset of anomalous transport under the action of drift instabilities in a plasma is discussed in terms of the motion of individual particles [7, 8]. In the presence of multimode perturbations, the motion of particles can become stochastic due to their interactions with fluctuations, in which case the particle confinement in a magnetic field is governed by collisionless diffusion [9–11]. We are interested in the particle interaction with moving, spatially localized, soliton-like fluctuations [12]. We also investigate the effect of the radial electrostatic field on the dynamics of particles and on their transport. This effect is of particular interest in studying improved confinement regimes achieved by applying a radial electrostatic field in different magnetic confinement systems (such as tokamaks, open devices, stellarators, and reversed-field pinches) [13–16].

We consider a two-dimensional (r, θ) configuration that is uniform along the z-axis and in which the magnetic field B depends only on the radius r and is directed along the z-coordinate. We take into account the radial electrostatic field $E_r(r)$ and assume that the waves are electrostatic and propagate along the azimuthal angle θ. The components of the electric field of each wave packet have the form

$$E_\theta^{\sim} = -\frac{1}{r}\frac{\partial \varphi^{\sim}}{\partial \theta}, \quad (1)$$

$$E_r^{\sim} = -\frac{\partial \varphi^{\sim}}{\partial r}. \quad (2)$$

Here, the electric potential $\varphi^{\sim}$ is represented as a sum of many harmonics:

$$\varphi^{\sim} = \sum_n \varphi_{0s,n} g_s(r) \cos[n(\omega_s t - \theta) + \psi_{s,n}], \quad (3)$$

where s is the number of the wave packet, n is the azimuthal wavenumber, ω_s is the angular phase velocity of the packet, $g_s(r)$ is its radial profile, and $\varphi_{0s,n}$ and $\psi_{s,n}$ are the amplitudes and initial phases of the electric-potential harmonics of the packet.

The particle trajectories are determined by numerically solving the following equations of particle motion:

$$m\frac{dv_r}{dt} = q[E_r^{\sim} + E_r(r) + v_\theta B], \quad (4)$$

$$m\frac{dv_\theta}{dt} = q(E_\theta^{\sim} - v_r B), \quad (5)$$

where m and q are the mass and charge of a particle and v_r and v_θ are the radial and azimuthal components of its velocity. The computations were carried out for the following linear radial profile of the electrostatic field:

$$E_r(r) = E_{0r}\frac{r}{a}, \quad (6)$$

where a is the radius of the plasma cylinder.

An important characteristic of anomalous transport is the radial displacement of a particle in its interaction with localized fluctuations. The figure illustrates the time dependence of the radial coordinate of a proton with an initial energy of 100 eV in a plasma column with radius $a = 0.2$ m in a uniform magnetic field $B = 0.5$ T for different values of E_{0r}. We can see that, as the radial electric field (of any polarity) increases, the radial displacement of the particle decreases substantially and, accordingly, the radial scale of the diffusion becomes shorter. In computations, it was assumed that

1063-780X/02/2809-0787$22.00 © 2002 MAIK "Nauka/Interperiodica"

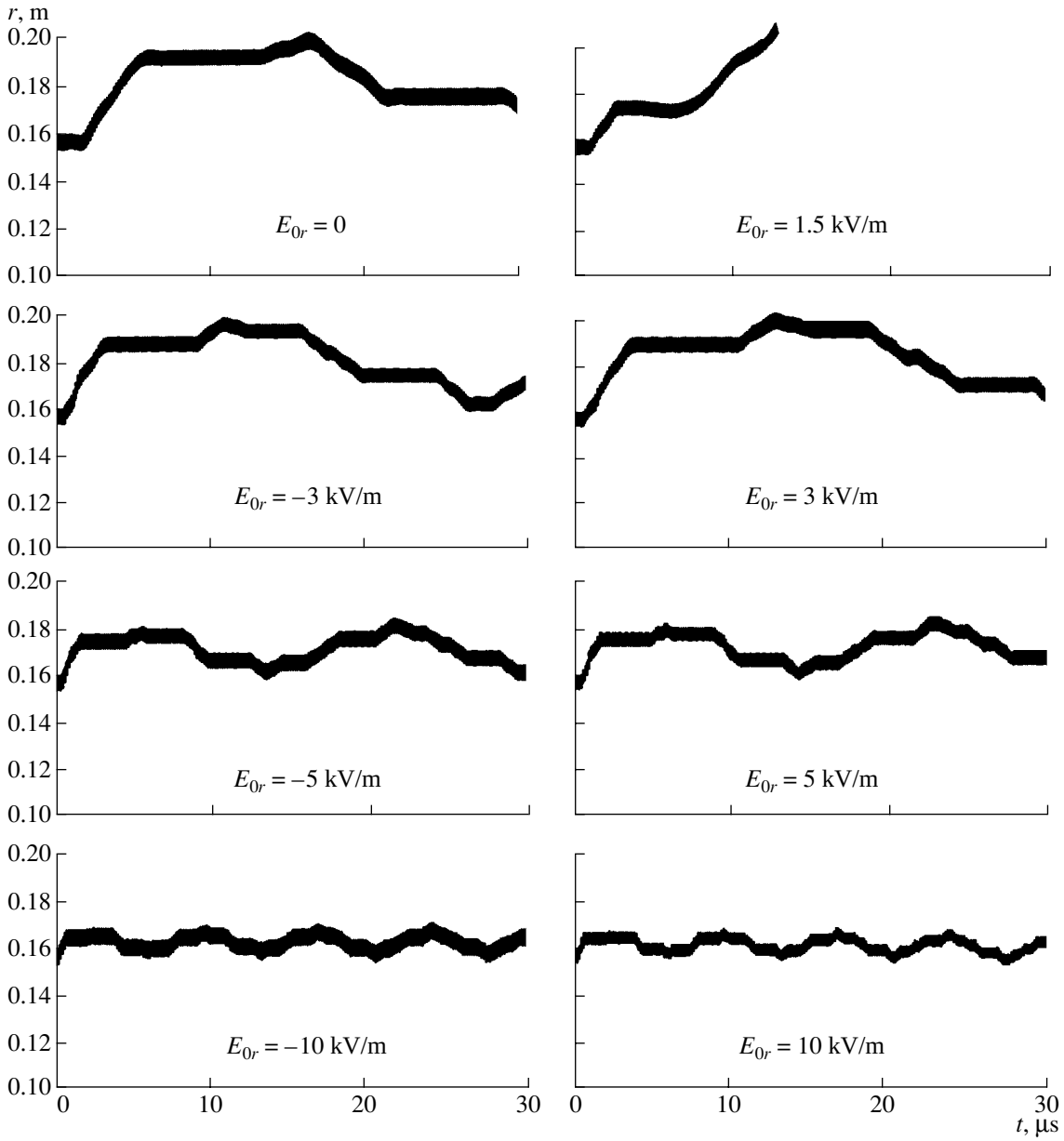

Time dependence of the radial coordinate of a proton with an initial energy of 100 eV for $B = 0.5$ T, $a = 0.2$ m, $\varepsilon = 0.1$, and $T_e = 100$ eV.

the electric field of the wave is localized along the azimuthal angle θ in a sufficiently narrow region of width δ_θ. The maximum potential difference $\Delta\varphi$ across this region (or the maximum potential amplitude) satisfies the condition

$$\varepsilon = \frac{|e\Delta\varphi|}{kT_e} \ll 1, \quad (7)$$

where ε is the relative amplitude of the wave potential, e is the charge of an electron, k is Boltzmann's constant, and T_e is the electron temperature. The results shown in the figure were obtained for $\varepsilon = 0.1$. Under the conditions chosen for the figure, the phase velocity is equal to the diamagnetic drift velocity; this corresponds to low-frequency drift waves [7, 8].

The time during which a particle interacts with the electric field of a single wave packet is equal to

$$\Delta t = \frac{\delta_\theta}{u}, \quad (8)$$

where u is the particle velocity with respect to the wave. For magnetized particles, we have $u = |v_{ph} - V_{dr}|$, where v_{ph} is the wave phase velocity and V_{dr} is the drift velocity of the particle guiding center. For unmagnetized par-

ticles, we have $u = |v_{ph} - v_\theta|$. In the geometry adopted here, the drift velocity V_{dr} may be caused by both the electric field and the magnetic field gradient:

$$V_{dr} = \frac{E_r(r)}{B} - \frac{mv^2}{2qB^2}\frac{dB}{dr}. \quad (9)$$

During the interaction time Δt, a magnetized particle is displaced in the radial direction by a distance of about

$$\Delta r \approx \frac{\tilde{E_\theta}}{B}\Delta t \approx \frac{\Delta\varphi}{Bu}. \quad (10)$$

Our numerical calculations show that estimate (10) is valid for both $u \ll v_\theta$ and $u \simeq v_\theta$. The time between the interactions of a particle with two successive wave packets is equal to

$$\tau_0 = \frac{\lambda}{u}, \quad (11)$$

where λ is the maximum (under the conditions adopted here) wavelength in the electric-potential spectrum (3). Using relationships (10) and (11), we can estimate the maximum anomalous diffusion coefficient in the case of stochastic particle motion:

$$D(r) \approx \frac{(\Delta r)^2}{\tau_0} \approx \frac{\varepsilon^2}{\lambda u}\left(\frac{kT_e}{eB}\right)^2 = \frac{\varepsilon^2}{\lambda|v_{ph} - V_{dr}|}\left(\frac{kT_e}{eB}\right)^2. \quad (12)$$

Estimate (12) shows, in particular, that the diffusion coefficient can be lowered (and, accordingly, the anomalous transport can be suppressed) when $|V_{dr}| \gg v_{ph}$. The drift velocity V_{dr} can be increased by applying a strong radial electric field, which gives rise to the $E \times B$ drift.

The phase velocity of the low-frequency waves, as well as of the lower hybrid drift waves [8], is equal to

$$v_{ph} \approx \frac{kT_e}{eB\delta_n}, \quad (13)$$

where δ_n is the radial scale of the plasma density gradient. For such waves, we have $\lambda \sim \delta_n$. Using these relationships, we obtain the diffusion coefficient for the above two limiting cases:

$$D(r) \approx \varepsilon^2\frac{kT_e}{eB}, \quad |V_{dr}| \ll v_{ph}, \quad (14)$$

$$D(r) \approx \frac{\varepsilon^2}{\lambda|E_rB|}\left(\frac{kT_e}{e}\right)^2, \quad |V_{dr}| \gg v_{ph}. \quad (15)$$

Note that the confinement time estimated from diffusion coefficient (14) coincides with that obtained in [10, 11] in analyzing the quasi-Hamiltonian dynamics of the guiding centers of the ions during their stochastic motion under the action of low-frequency drift waves.

In conclusion, we have analyzed the ion dynamics under the conditions of a stochastic regime of anomalous diffusion. Both qualitative estimates and computational results demonstrate that anomalous diffusion can be suppressed by applying a strong radial electric field. We emphasize that we have neglected a possible decrease in the oscillation amplitude ε after applying the radial electric field and assumed that ε lies in the range $\varepsilon = 0.01$–0.1, corresponding to the experiments of [14]. Presumably, the value of ε should be determined from the self-consistent solution to the corresponding nonlinear problem.

ACKNOWLEDGMENTS

This work was supported by the International Science and Technology Center, project no. 1260.

REFERENCES

1. A. A. Vedenov, E. P. Velikhov, and R. Z. Sagdeev, Nucl. Fusion **1**, 82 (1961).
2. W. E. Drummond and D. Pines, Nucl. Fusion, Suppl. **3**, 1049 (1962).
3. B. B. Kadomtsev, in *Reviews of Plasma Physics*, Ed. by M. A. Leontovich (Gosatomizdat, Moscow, 1964; Consultants Bureau, New York, 1968), Vol. 4.
4. R. C. Davidson and N. T. Gladd, Phys. Fluids **18**, 1327 (1975).
5. N. A. Krall, Phys. Fluids B **1**, 1811 (1989).
6. W. Horton, Rev. Mod. Phys. **71**, 735 (1999).
7. B. B. Kadomtsev and A. V. Timofeev, Dokl. Akad. Nauk SSSR **146**, 581 (1962) [Sov. Phys. Dokl. **7**, 826 (1963)].
8. R. C. Davidson and N. A. Krall, Nucl. Fusion **17**, 1313 (1977).
9. V. I. Khvesyuk, A. Yu. Chirkov, and A. A. Pshenichnikov, J. Plasma Fusion Res. **3**, 150 (2000).
10. V. I. Khvesyuk and A. Yu. Chirkov, Vopr. At. Nauki Tekh., Ser. Termoyad. Sint., No. 3, 17 (2000).
11. V. I. Khvesyuk and A. Yu. Chirkov, Fusion Technol. **39** (1T), 398 (2001).
12. A. S. Kingsep, L. I. Rudakov, and R. N. Sudan, Phys. Rev. Lett. **31**, 1482 (1973).
13. F. Wagner, G. Gosa Becker, K. Behringer, *et al.*, Phys. Rev. Lett. **49**, 1408 (1982).
14. A. Mase, A. Itakura, M. Inutake, *et al.*, Nucl. Fusion **31**, 1725 (1991).
15. A. Fujisawa, H. Iguchi, T. Minami, *et al.*, Phys. Rev. Lett. **82**, 2669 (1999).
16. V. Antoni, E. Martines, D. Desideri, *et al.*, Plasma Phys. Controlled Fusion **42**, 83 (2000).

Translated by I. A. Kalabalyk

Plasma Physics Reports, Vol. 28, No. 9, 2002, pp. 790–795. Translated from Fizika Plazmy, Vol. 28, No. 9, 2002, pp. 858–864.
Original Russian Text Copyright © 2002 by Kalinin, Korel'skiĭ, Kravchenko, Shashkov.

PLASMA DIAGNOSTICS

Laser Probing of the Plasma in the S-300 Facility

Yu. G. Kalinin, V. A. Korel'skiĭ, E. V. Kravchenko, and A. Yu. Shashkov

Russian Research Centre Kurchatov Institute, pl. Kurchatova 1, Moscow, 123182 Russia

Received February 21, 2002

Abstract—A method for the laser probing of an imploding plasma in the S-300 high-current generator (I = 4 MA, Z = 0.15 Ω, and τ = 100 ns) with the use of a YAG : Nd laser is described. The first version of the method enables obtaining three-frame shadow and schlieren photographs of the plasma of the accelerator load with an exposure of 10 ns and an interval between frames of 25 ns. The second version enables the five-frame probing of the plasma with an exposure of 1 ns and an interval between frames of 10 ns. Stimulated Brillouin scattering in carbon tetrachloride is used to compress the probing laser pulse. A series of shadow and schlieren photographs of the plasma of different liners and Z-pinches are obtained. Mechanisms for the image formation are discussed. The magnitude and gradients of the plasma density are estimated. © *2002 MAIK "Nauka/Interperiodica".*

1. INTRODUCTION

Laser probing (interferometry, shadow and the schlieren photography, etc.) has long been a classic method for diagnosing imploding plasmas. This method allows one to study a plasma with a definite density magnitude and gradients. However, to implement this diagnostics in pulsed high-current generators, it is necessary to solve a number of problems related to both the design of the generators and the specific conditions under which experiments are carried out: large distances between the probing radiation source, the object under study, and the image plane; the relatively small dimensions of the object; and, finally, rigid requirements to the synchronization between the probing laser pulse and the current pulse through the load. In this paper, we describe a system for the laser probing of the plasma in the S-300 high-current generator [1]. In our opinion, the system is fairly well suited for these conditions.

The S-300 eight-module generator, operating at a current of up to 4 MA with a current rise time of 100 ns (Fig. 1), is destined for experiments with high-temperature pulsed plasmas of light liners and Z-pinches. The accelerator loads were positioned at the center of the vacuum chamber. The input and output diagnostic windows 100 mm in diameter were placed at a distance of 2.4 m from the load. Accordingly, the angular aperture of the probing beams was no larger than 2.5°.

2. DIAGNOSTIC COMPLEX

The diagnostic complex included the transmitting and receiving laser components.

The receiving component, which was used to record the shadow images of the plasma, consisted of a lens (f = 1600 mm) imaging the plasma with a magnification factor of 2 and a camera equipped with a set of filters and a photographic cassette. Optical wedges with

Fig. 1. General view of the S-300 facility. Arrow 1 indicates the photographic camera, and arrow 2 indicates the holder with mirrors directing the probing laser beams to the plasma object.

1063-780X/02/2809-0790$22.00 © 2002 MAIK "Nauka/Interperiodica"

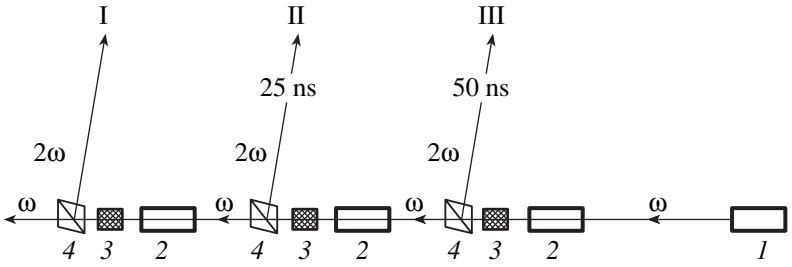

Fig. 2. Optical scheme for generating three probing beams (I, II, and III) with 25 ns delays between the pulses: (*1*) DO, (*2*) amplifier, (*3*) nonlinear crystal for the frequency doubling, and (*4*) Glan prism for separating the beams at the fundamental and second harmonics. The latter pass through the optical delay lines and are directed into the S-300 generator.

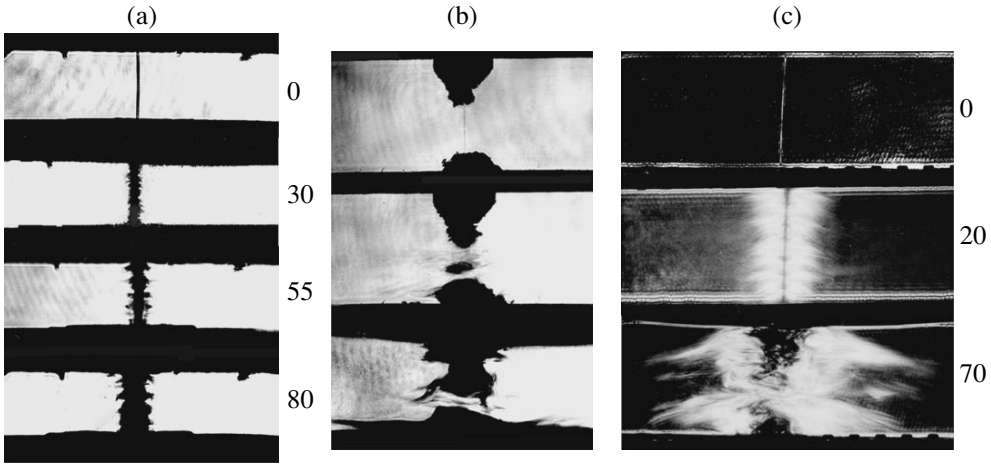

Fig. 3. (a) Shadow photograph of the implosion of an aluminum wire 110 μm in diameter and 1 cm in length at a current through the load of 2 MA. (b) Shadow photograph of the implosion of a C_2D_4 fiber 30 μm in diameter and 0.6 cm in length; the upper frame is made before the current is switched on (the wire clamps are seen at the top and bottom); the delay between the middle and lower frames is 50 ns. (c) Schlieren photographs of the implosion of a C_2D_4 fiber 30 μm in diameter and 1.5 cm in length an a current of 1.7 MA. Schlieren masks allow the detection of the deflection angles of the probing beams in the range from 1 to 6 mrad in all directions. Here and in subsequent figures, numerals on the right from photographs show the delay time (in ns) between the exposure and the current start (at a level of no less than 5%).

an angle of 1° or 2° were positioned near the focal plane of the lens in order to separate the beams in the image plane by a required distance. If needed, different schlieren masks could be positioned in the focal plane of the lens. For immobile objects, the resolution of the system in the object plane was no worse than 35 line/mm.

The transmitting component was located in a separate room; the distance between the laser system and the target unit exceeded 18 m. The first version of the transmitting component (Fig. 2) consisted of a YAG : Nd driving oscillator (DO), a three-stage second-harmonic generator (SHO), and optical delay lines. An electrooptical shutter was synchronized with the current pulse of the S-300 generator. Each SHO stage consisted of a single-pass amplifier, a $LiNbO_3$ nonlinear crystal with the temperature-sensitive tuning to the phase matching, and a Glan prism. After passing through the prism, second-harmonic radiation arrived at the optical delay line and, then, at a set of mirrors directing this radiation onto the plasma object. Radiation at the fundamental frequency, which was polarized orthogonally to the second-harmonic radiation, passed through the Glan prism without deflection. Then, it was amplified and used to generate the second harmonic in the next stage. The energy in each probing beam was 20–25 mJ, the wavelength was 532 nm, the divergence was ~1 mrad, the pulse duration was 10 ns, and the interval between pulses was 25 ns. The beams were directed to the center of the vacuum chamber, where the target unit was installed.

The technique described, which allowed the successive separation of second-harmonic beams, substantially reduced the radiation load on crystals as com-

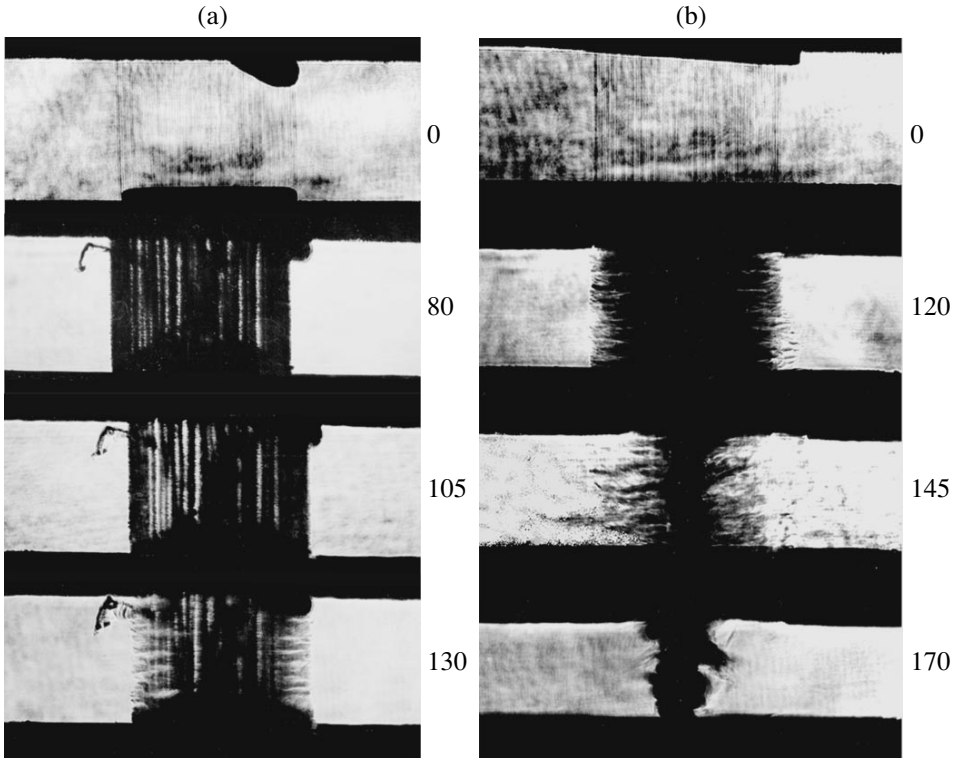

Fig. 4. Shadow photographs of two imploding wire arrays composed of eighty tungsten wires 6 μm in diameter. The array diameter is 1 cm, its length is 1 cm, the current through the load is 2.6 MA, and the current rise time is ~110 ns.

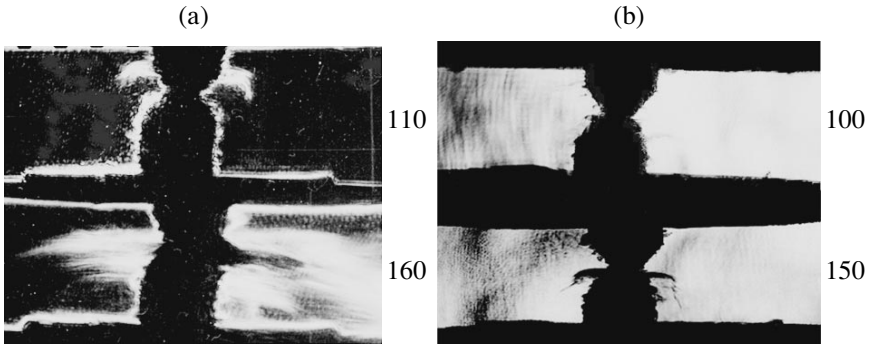

Fig. 5. (a) Schlieren photographs of a Z-pinch with an 8-mm-long and 5-mm-diameter load made of agar-agar and C_2D_4 and having a preformed neck; schlieren masks are similar to those in Fig. 3c. (b) Shadow photographs of the same load with an addition of LiD. The current is 2.2 MA.

pared to the conventional scheme of dividing the output beam. As a result, the number of probing beams can be increased with a minimal expenditure. With this scheme for the probing-beam generation, all laser and nonlinear optical components operated under radiation loads that were far below the limiting ones. This substantially improved the reliability of the complex operation, so that we could adjust the entire diagnostic system in the pulsed mode with a repetition rate of 1 Hz. This is particularly important for experiments with large accelerators having small input apertures for the probing beams.

Figures 3, 4, and 5 show plasma photographs of different S-300 loads. It is seen in the photographs that the plasma of these loads moves at velocities of $\sim 5 \times 10^7$ cm/s. In this case, the spatial resolution in the direction of plasma motion, $\delta = v\tau$, is determined by the duration of the probing pulse ($\tau = 10$ ns) and amounts to several millimeters. Hence, in order to improve the

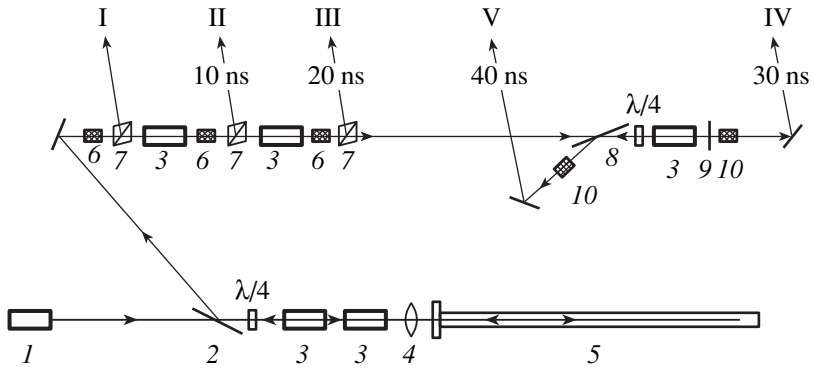

Fig. 6. Optical scheme of the transmitting component of the laser diagnostic complex for five-frame plasma probing: (*1*) YAG : Nd DO, (*2*, *8*) isolators, (*3*) YAG : Nd amplifiers, (*4*) lens (f = 0.9 m), (*5*) scattering CCl_4 cell (l = 1.5 m), (*6*) SHOs ($LiNbO_3$), (*7*) Glan prisms, (*9*) mirror with a reflection coefficient of 30%, and (*10*) SHOs (KTP). Five beams pass through the optical delay lines and are directed into the S-300 generator.

temporal and spatial resolution of the diagnostic technique, the laser pulse should be shortened. For this purpose, the laser system was modified; in addition, the number of the probing beams was increased to 5.

To shorten the laser pulse, we used the compression of the DO pulse due to stimulated Brillouin scattering (SBS) in a nonlinear optical medium. This shortening technique has a number of advantages over the conventional electrooptical method of "cutting" a short pulse from an ordinary giant pulse. This is, first of all, an increase in the power due to the high efficiency of energy transfer from the original (pumping) pulse to the scattered (Stokes) pulse. In addition, there is the possibility of amplifying the Stokes radiation by the pumping-radiation amplifiers because the frequency shift between the pumping and scattered radiation is negligibly small. In addition, there is no delay between these pulses. Finally, we note that this method is very convenient because the process is passive in character and the synchronization of the laser complex with the experimental device is the same as in the first version of the transmitting component.

Phase conjugation and pulse compression in various nonlinear media in the course of SBS were studied in detail by many authors (see, e.g., [2–7]) and have already been used in plasma diagnostics [8].

Figure 6 shows the optical scheme of the transmitting component of the diagnostic complex. The driving oscillator (*1*) with an electrooptical shutter operates at a pumping power slightly exceeding the threshold level for generating the fundamental transverse mode TEM_{00}. The pulse duration is 7 ns, and the pulse energy is 0.3–0.5 mJ. The cavity length is 20 cm, and the diameter of the aperture separating out the fundamental mode is 1 mm. The studies of the longitudinal mode structure with the help of a Fabry–Perot interferometer showed that the DO mode composition varied from pulse to pulse and consisted of one to six modes. Although single-frequency laser pulses are compressed most efficiently (in this case, cavities with passive Q-switching are usually used), we have managed to achieve the reproducible compression of the pumping pulse to 1.2 ns. This result is far from the maximum possible compression, probably, because of the presence of several longitudinal modes in the pumping radiation.

Then, the DO pulse passes through an isolator (*2*) consisting of an interference polarizer and a quarter-wave plate and enters two single-pass amplifiers (*3*). The amplified signal is focused by a lens (*4*) with a 900-mm focal length into a 1.5-m-long cell filled with carbon tetrachloride. The backscattered Stokes pulse with a lower frequency is amplified and directed by the spatial isolator (*2*) into the SHO stages. The first three of them are similar to the stages of the above version of the transmitting component. After these stages, the radiation at the fundamental frequency falls into an isolator (*8*) and is amplified. A fraction of the signal is reflected backward by a mirror (*9*) with a reflection coefficient of 30%. The frequency of radiation passed through the mirror doubles in a KTP crystal (*10*); this second-harmonic beam is the fourth probing beam. The radiation reflected from the mirror (*9*) is amplified during its backward pass and is deflected by the isolator (*8*). This beam, whose radiation frequency doubles in the second KTP crystal, serves as the fifth probing beam. A set of mirrors (which is not depicted in Fig. 6) delays the probing laser beams by 10 ns and directs them to the load of the experimental device and, further, to the receiving component of the diagnostic complex.

The duration of the second-harmonic pulses did not exceed 1 ns because of the square dependence of their intensity on the intensity of the pumping radiation. Their energy was 3–5 mJ, which was quite sufficient to ignore emission from the plasma. The diagnostic complex was adjusted in the pulse-periodic mode at a repetition rate of 0.25–0.5 Hz. The maximum repetition rate was determined by the resources of the pumping-lamp power supply, rather than the processes in the SBS cell

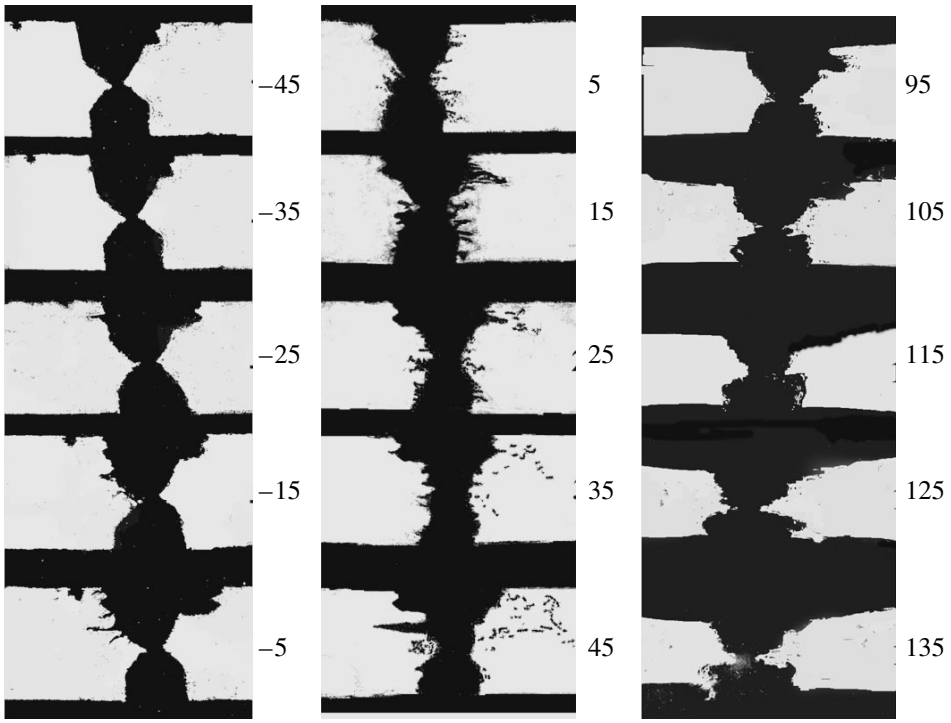

Fig. 7. Five-frame shadow photographs of three agar-agar Z-pinches. Numerals on the right from photographs show the delay time (in ns) between the exposure and the current start. The minus sign means that the frames are made before the beginning of the load current signal detected by the oscillograph; in this case, the current at the beginning of the oscillograph signal can attain 100 kA.

(the latter allowed us to obtain a well reproducible compression of laser pulses at repetition rates up to 10 Hz [6]).

Figure 7 shows shadow photographs of the Z-pinch. In the middle column, one can see the expansion of small plasma drops, which are invisible on photos obtained with an exposure of 10 ns.

3. ESTIMATES OF THE MAGNITUDE AND GRADIENTS OF THE PLASMA DENSITY

There are several mechanisms that may be responsible for the formation of a shadow in photographs.

The first mechanism is the cutoff of the probe radiation in plasma when the radiation frequency approaches the plasma frequency ω_0:

$$\omega \approx \omega_0 = \sqrt{\frac{4\pi N_e e^2}{m}}.$$

For a beam with a wavelength of 532 nm, this occurs at densities of $N_e \geq 4 \times 10^{21}$ cm^{-3}.

Second, the probe radiation can be absorbed via inverse bremsstrahlung (i.e., due to free–free transitions). In this case, the attenuation of laser radiation is described by Bouguer's law,

$$I_\nu = I_{\nu 0}\exp(-\vartheta l),$$

where l is the distance passed by the probing beam and the absorption coefficient ϑ is determined by the expression [9]

$$\vartheta = C_1 \frac{Z^2 g N_e N_i}{T_e^{1/2}\nu^3}\left[1 - \exp\left(-\frac{h\nu}{kT_e}\right)\right].$$

For $kT_e \gg h\nu$, which is always satisfied in our experiments, the absorption coefficient is described by the formula

$$\vartheta \approx C_1 \frac{h}{k}\frac{Z g N_i^2}{T_e^{3/2}\nu^2}.$$

Here, $C_1 = 3.69 \times 10^8$ cm^5 degree$^{1/2}$ s^{-3}; Z is the ion charge; g is the Gaunt factor; N_e and N_i are the electron and ion densities, respectively; and ν is the probe-radiation frequency. From this formula, we obtain the following expression for N_i:

$$N_i = \sqrt{\frac{k}{C_1 h}\frac{\vartheta T_e^{3/2}\nu^3}{Z^3 g}} \approx 7.5\nu\sqrt{\frac{\vartheta T_e^{3/2}}{Z^3 g}}.$$

For a tungsten plasma under our experimental conditions, we have $N_i > 5 \times 10^{18}$ cm^{-3}.

It should be noted that, for a plasma of high-Z materials, the ion density estimated by this formula depends weakly on the electron temperature. Indeed, we have

$N_i \sim T_e^{3/4}/Z^{3/2}(T)$, and the average ion charge number Z is well approximated by the dependence $Z \sim T^{1/2}$. Calculations (see, e.g., [10]) show that, as T_e increases from 10 to 100 eV, Z increases from 6 to 20; in this case, N_i at fixed ϑ changes by no more than 10%.

The third mechanism for the formation of a shadow in photographs is the refraction of the probing beam in plasma regions where the electron density gradient is so large that the refracted rays fall outside the aperture angle of the lens $\alpha = d/a$, where d is the lens diameter and a is the distance from the lens to the object. The deflection angle and the electron-density gradient are related by the formula [11]

$$|\nabla N_e| = -\frac{\varepsilon}{4.46 \times 10^{-14} \lambda^2 l},$$

where ε is the refraction angle, λ is the probing-radiation wavelength, and l is the plasma length along the probing beam. This formula is valid if the probing-wave frequency is much higher than the frequency of electron–ion (or electron–neutral) collisions ($\omega \gg \omega_{ei}$) and much higher than the electron cyclotron frequency, $\omega \gg \omega_e = eB/(mc)$ (here, B is the magnetic field, and m is the electron mass), which is always satisfied under experimental conditions.

For the given geometry of the diagnostic windows, the refraction angle is ~20 mrad, which corresponds to the plasma density gradient $|\nabla N_e|$ no larger than 3×10^{20} cm^{-4}. From the characteristic plasma size observed, we can estimate the electron density as $N_e = 10^{20}$ cm^{-3}. Consequently, for the tungsten plasma, the ion density (Fig. 4) can be estimated as 2×10^{19} cm^{-3} and, for other loads, as 5×10^{19} cm^{-3}.

Hence, the formation of a shadow in photographs via inverse bremsstrahlung absorption seems to be most probable, at least, for a metal plasma. The appearance of a shadow due to absorption was previously observed in experiments on the heating of foils by focused electron beams [12], as well as in experiments on the implosion of highly emitting gas puffs [13]. This mechanism is dominant under many experimental conditions.

The refraction angles detected by the schlieren method lie in the range from 1 to 6 mrad, which determines the range of detectable density gradients: $10^{19} < |\nabla N_e| < 5 \times 10^{19}$ cm^{-4}. Taking into account the characteristic plasma size, the electron density is estimated at 10^{19} cm^{-3}.

4. CONCLUSION

The five-frame laser probing system with an exposure of 1 ns and an interval between frames of 10 ns has been created. The system uses the second harmonic of a YAG : Nd laser and the compression of the DO pulse due to BS in a nonlinear optical medium. It is capable of operating in the repetitive mode under unfavorable conditions of the S-300 generator (the distance from the object is 18 m, and the angular aperture is 2.5°). This made it possible to reliably record five shadow images of the plasma produced by the magnetic implosion of light liners and Z-pinches.

Small-scale plasma formations expanding at velocities of $(2–5) \times 10^8$ cm/s have been detected.

Mechanisms responsible for the formation of a shadow in the photographs have been discussed, and the plasma density has been estimated.

ACKNOWLEDGMENTS

We thank P.I. Blinov for his help in adjustment of the components of the diagnostic complex. This study was supported by the Russian Foundation for Basic Research (project no. 01-02-17359).

REFERENCES

1. A. S. Chernenko, Yu. M. Gorbulin, Yu. G. Kalinin, *et al.*, in *Proceedings of the 11th International Conference on High-Power Particle Beams, Prague, 1996*, p. 154.
2. D. V. Vlasov, Zh. Éksp. Teor. Fiz. **64**, 1986 (1973) [Sov. Phys. JETP **37**, 1001 (1973)].
3. V. A. Gorbunov, V. B. Ivanov, S. B. Papernyĭ, and V. R. Startsev, Izv. Akad. Nauk SSSR, Ser. Fiz. **48**, 1580 (1984).
4. R. R. Buzyalis, A. S. Dement'ev, and E. K. Kosenko, Kvantovaya Élektron. (Moscow) **12**, 2024 (1985).
5. I. M. Bel'dyugin, B. Ya. Zel'dovich, M. V. Zolotarev, and V. V. Shkunov, Kvantovaya Élektron. (Moscow) **12**, 2394 (1985).
6. V. Kh. Bagdasarov, N. N. Denisov, P. P. Pashinin, and E. I. Shklovskiĭ, Kvantovaya Élektron. (Moscow) **14**, 1364 (1987).
7. V. N. Belousov and Yu. K. Nizienko, Preprint No. 4707/7 (Institute of Atomic Energy, Moscow, 1988).
8. R. Alliaga-Rossel, J. Bayley, A. Mamin, and Yu. Nizienko, in *Proceedings of the 4th International Conference on Dense Z-pinches, Vancouver, 1997.*
9. A. N. Zaĭdel' and G. V. Ostrovskaya, *Laser Methods for Plasma Research* (Nauka, Leningrad, 1977).
10. D. Mosher, Phys. Rev. **10**, 2330 (1974).
11. É. P. Kruglyakov, *Plasma Diagnostics* (Atomizdat, Moscow, 1973), Vol. 3, p. 97.
12. Yu. M. Gorbulin, I. A. Znamenskaya, D. M. Zlotnikov, *et al.*, Preprint No. 4042/7 (Institute of Atomic Energy, Moscow, 1984).
13. S. L. Bogolyubsky, E. M. Gordeev, Yu. G. Kalinin, *et al.*, in *Proceedings of the 7th International Conference on High-Power Beams, Karlsruhe, 1988*, p. 1255.

Translated by N. F. Larionova